Systematic study of the role of the indirect RKKY exchange interaction in ultrafast spin dynamics of 4*f* antiferromagnets

Dissertation

zur Erlangung des Grades eines
Doktors der Naturwissenschaften

am Fachbereich Physik
der Freien Universität Berlin

vorgelegt von
Sang-Eun Lee

Berlin 2022

This work was done between December 2017 and August 2022 in the research group "Dynamics of Correlated Materials", headed by Dr. Laurenz Rettig, at the Department of Physical Chemistry (Director: Prof. Dr. Martin Wolf) of the Fritz Haber Institute of the Max Planck Society.

Erstgutachter: Dr. Laurenz Rettig
Zweitgutachter: Prof. Dr. Martin Weinelt

Tag der Disputation: 14. Dez. 2022

Contents

Abstract

Dissipation-free manipulation of magnetic order remains a long-standing goal for future spintronic devices, and is of particular focus in the field of ultrafast magnetism. Ferromagnets, which have long been the primary focus of this field, suffer from inherent angular momentum dissipation, which sets fundamental limits on achievable time scales and energy efficiency. In contrast, antiferromagnets can overcome these limits, and achieve dissipation-free spin dynamics by direct angular momentum transfer between opposing magnetic sublattices. While presenting appealing prospects for devices, a fundamental understanding of how such transfer is mediated remains largely unexplored, in particular when indirect magnetic couplings are at play. A prime example is the indirect Ruderman-Kittel-Kasuya-Yosida (RKKY) exchange coupling, in which conduction electrons mediate between localized moments. There are two important aspects of RKKY coupling: (i) the inter-atomic coupling between localized moments and (ii) the intra-atomic coupling between localized moments and itinerant conduction electrons. This thesis explores these two different aspects of the RKKY coupling by studying ultrafast spin dynamics of $4f$ antiferromagnets experimentally.

First, we demonstrate that the rate of such direct angular momentum transfer between antiparallel localized $4f$ moments scales with the strength of the RKKY interaction by singling out the role of the localized 4f moments, the source, and of the conduction electrons, the mediator of the RKKY interaction. Our study focuses on ultrafast magnetic order dynamics in a series of lanthanide-based antiferromagnets $Ln\,T_2\mathrm{Si}_2$. Our key observation is that the $4f$ angular momentum transfer rate scales with the *de Gennes factor*, a fundamental quantity derived from the L and S atomic numbers of localized $4f$ electrons (Chapter 4) and with the spin polarization of $5d$ conduction electrons around the Fermi level (Chapter 5). Supported by ab-initio calculations, we reveal a direct correspondence between angular momentum transfer rates to the strength of antiferromagnetic RKKY coupling.

Next, we study the on-site RKKY coupling between the localized $4f$ moments and itinerant conduction electrons by measuring ultrafast transient temperature dynamics along with surface and bulk magnetic order dynamics. Our key observations are that (i) the conduction electrons and localized moments exhibit very similar demagnetization timescale, which suggests a strong on-site RKKY coupling and (ii) there are robust magnetic orderings of both conduction electrons and localized moments even when the transient temperature is well above the phase transition temperature for hundreds of picoseconds. A microscopic three temperature model based on the Landau-Lifshitz-Bloch equation phenomenologically explain this with effective increase of phase transition temperature during ultrafast spin dynamics (Chapter 6). We also demonstrate that, in extreme case, the localized $4f$ moments can stay non-thermalized upon optical excitation for hundreds of picoseconds exhibiting 200-ps-long disparate dynamics of exchange couplings between $4f$ moments and long-range antiferromagnetic $4f$ ordering (Chapter 7).

Our results are of fundamental importance for ultrafast magnetic order dynamics in that they demonstrate a systematic relation between microscopic magnetic coupling and inter- and intra-atomic flow of angular momentum and energy. From a practical perspective, they also present new opportunities for controlling or even engineering magnetic order dynamics, because the RKKY magnitude can be sensitively tuned, such as by modifying either the $4f$ moments or the conduction electrons. This is particularly relevant due to the recent rise in prominence of *antiferromagnetic spintronics*. With these considerations, we systematically explored the role of the RKKY interaction in ultrafast spin dynamics of $4f$ antiferromagnets in this thesis.

Deutsche Kurzfassung

Die disspationsfreie Manipulation der magnetischen Ordnung bleibt ein langjähriges Ziel für zukünftige Spintronik-Geräte und steht besonders im Fokus auf dem Gebiet des ultraschnellen Magnetismus. Ferromagnete, die seit langem im Mittelpunkt dieses Gebiets stehen, leiden unter einer inhärenten Drehimpulsdissipation, die den erreichbaren Zeitskalen und der Energieeffizienz grundlegende Grenzen setzt. Im Gegensatz dazu können Antiferromagnete diese Grenzen überwinden und eine dissipationsfreie Spindynamik durch direkte Drehimpulsübertragung zwischen antiparallelen magnetischen Untergittern erreichen. Während sie attraktive Aussichten für Geräte bieten, bleibt ein grundlegendes Verständnis darüber, wie eine solche Übertragung vermittelt wird, weitgehend unerforscht, insbesondere wenn es um indirekte magnetische Kopplungen geht. Ein Paradebeispiel ist die indirekte Austauschkopplung Ruderman-Kittel-Kasuya-Yosida (RKKY), bei der Leitungselektronen zwischen lokalisierten Momenten vermitteln. Es gibt zwei wichtige Aspekte der RKKY-Kopplung: (i) die interatomare Kopplung zwischen lokalisierten Momenten und (ii) die intraatomare Kopplung zwischen lokalisierten Momenten und wandernden Leitungselektronen. Diese Dissertation untersucht diese beiden unterschiedlichen Aspekte der RKKY-Kopplung, indem sie die ultraschnelle Spindynamik von $4f$-Antiferromagneten experimentell untersucht.

Zunächst zeigen wir, dass die Geschwindigkeit eines solchen direkten Drehimpulsübertragung zwischen antiparallelen lokalisierten $4f$-Momenten mit der Stärke der RKKY Wechselwirkung skaliert, indem wir die Rolle der lokalisierten $4f$-Momente, der Quelle, und der Leitungselektronen, des Vermittlers, herausgreifen der RKKY-Interaktion. Unsere Studie konzentriert sich auf die ultraschnelle magnetische Ordnungsdynamik in einer Reihe von Lanthanoid-basierten Antiferromagneten $Ln\,T_2\mathrm{Si}_2$. Unsere wichtigste Beobachtung ist, dass die Schnelligkeit von der $4f$ Drehimpulsübertragung mit dem *de Gennes factor* skaliert, einer fundamentalen Größe, die von den L- und S-Ordnungszahlen lokalisierter $4f$-Elektronen abgeleitet wird (Kapitel 4) und mit der Spinpolarisation von $5d$ Leitungselektronen um das Fermi-Energy herum (Kapitel 5). Unterstützt durch Ab-initio-Rechnungen zeigen wir eine direkte Korrelation zwischen Schnelligkeit von der Drehimpulsübertragung und der Stärke der antiferromagnetischen RKKY-Kopplung.

Als nächstes untersuchen wir die RKKY-Kopplung vor Ort zwischen den lokalisierten $4f$-Momenten und wandernden Leitungselektronen, indem wir die ultraschnelle transiente Temperaturdynamik zusammen mit der Dynamik der magnetischen Ordnung auf der Oberfläche und im Volumen messen. Unsere wichtigsten Beobachtungen sind, dass (i) die Leitungselektronen und lokalisierten Momente eine sehr ähnliche Entmagnetisierungszeitskala aufweisen, was auf eine starke RKKY-Kopplung vor Ort hindeutet, und (ii) es selbst bei transienter Temperatur robuste magnetische Ordnungen sowohl von Leitungselektronen als auch von lokalisierten Momenten gibt für Hunderte von Pikosekunden deutlich über der Phasenübergangstemperatur liegt. Ein microscopic three temperature model basierend auf der Landau-Lifshitz-Bloch-Gleichung erklärt dies phänomenologisch mit einer effektiven Erhöhung der Phasenübergangstemperatur während ultraschneller Spindynamik (Kapitel 6). Wir zeigen auch, dass die lokalisierten $4f$-Momente im Extremfall bei optischer Anregung für Hunderte von Pikosekunden nicht-thermalisiert bleiben können, was eine 200 ps lange unterschiedliche Dynamik von Exchange-kopplungen zwischen $4f$-Momenten und langreichweitigen antiferromagnetischen $4f$ Ordnungen aufweist (Kapitel 7).

Unsere Ergebnisse sind von grundlegender Bedeutung für die ultraschnellen Spindynamik, da sie eine systematische Beziehung zwischen mikroskopischer magnetischer Kopplung und dem inter- und intraatomaren Fluss von Drehimpuls und Energie aufzeigen. Aus praktischer Sicht bieten sie auch neue Möglichkeiten zur Steuerung oder sogar zur Konstruktion der Spindynamik, da die RKKY-Größe fein abgestimmt werden kann, z. B. durch Modifizieren entweder der $4f$-Momente oder der Leitungselektronen. Dies ist besonders relevant aufgrund der jüngsten Zunahme der Bedeutung der *antiferromagnetischen Spintronik*. Mit diesen Überlegungen haben wir in dieser Dissertation systematisch die Rolle der RKKY-Kopplung in der ultraschnellen Spindynamik von $4f$-Antiferromagneten untersucht.

This page is intentionally left blank.

Chapter 1

Introduction

4*f* Antiferromagnets

> *"It's a magnet. But you cannot stick it on your refrigerator."*
> *"Then why are you studying about it?"*

That's how I introduce what an antiferromagnet is to the people who have not studied physics seriously. Indeed, antiferromagnets are magnetic materials. However, unlike ferromagnets where magnetic moments are ordered in a uniform direction (Figure 1.1-a), in antiferromagnets, magnetic moments are ordered in a way that the moments are cancelling each other, resulting zero net magnetization (Figure 1.1-b). This self-cancelling arrangement makes antiferromagnetism externally invisible. However, though invisible, antiferromagnets as well have ordered spin structure, and this ordered spin structure is well maintained unless thermal excitation or external field application overcomes the maintaining force. Then how do antiferromagnets maintain such self-cancelling spin arrangement, which is more complex spin structure than uniformly aligned ferromagnetic arrangement? What physical interaction governs such an complexly ordered spin structure? This externally invisible nature of antiferromagnetism might be the reason why Louis Eugène Félix Néel, a Nobel Laureate in Physics in 1970 for his fundamental work and discoveries concerning antiferromagnetism, expressed that antiferromagnets *are extremely interesting from the theoretical viewpoint, but do not seem to have any applications* [Née70].

Over 90 years have passed since Néel embarked this field of antiferromagnetism in 1928 [Née70]. There have been numerous progresses to make antiferromagnets interesting not only from the theoretical perspective, but also from the practical perspective. Applications for magnetic memories such as magnetoresistive random access memory (MRAM) have been actively studied for the last two decades utilizing the self-cancelling spin arrangement of antiferromagnets. MRAMs read and write 0 and 1 (i.e. information) with magnetic recording. In magnetic recording, information can be written by changing local magnetic orientation with external magnetic field application, and can be read by measuring the local orientation [CFV07]. Since the information is written and stored with spin orientations, not charges, MRAMs are robust against charge fluctuations promising better stability compared to current charge flash memory [CFV07; Wad+16]. So far, mostly ferromagnets have been employed for implementation of MRAMs, but due to intrinsic nature of ferromagnets that spins tend to align into a uniform direction, any disturbing magnetic fields can cause local reorientation, which results information loss. In this regard, self-cancelling spin arrangement in antiferromagnets can solve this limitation since this antiferromagnetic (AF) spin arrangement cancels out the disturbing magnetic fields [Wad+16; Jun+16]. Furthermore, proximity of different magnetic sublattices in antiferromagnetic spin arrangement opens a direct spin transfer channel enhancing the angular momentum transfer, the bottleneck process of ultrafast demagnetization [Thi+17; Win+22]. It is expected that antiferromagnet-based memories can have writing speed of well above gigahertz (10^9 s^{-1}) range where ferromagnet-based memories become extremely energy-inefficient [Ole+18]. Therefore, antiferromagnets are good candidate materials

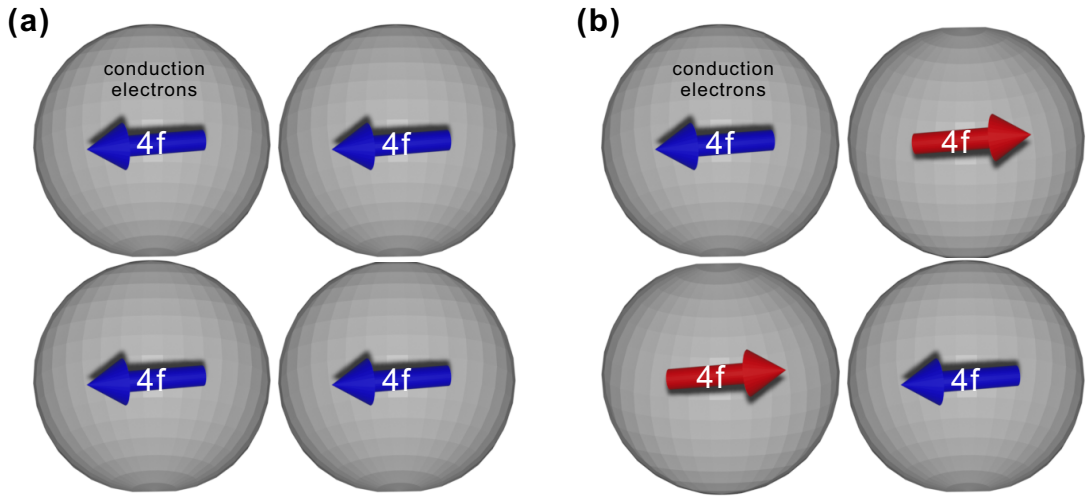

Figure 1.1: Schematics of (a) a $4f$ ferromagnetic spin structure and (b) a $4f$ antiferromagnetic (AF) spin structure. Localized $4f$ spins indirectly interact via surrounding conduction electrons.

for future memory devices, which can improve stability, process rate, and energy efficiency. These expected benefits surely make antiferromagnets interesting in the application point of view as well.

Among various antiferromagnets, in this thesis, I study specifically $4f$ antiferromagnets (Figure 1.1-b). $4f$ antiferromagnets are lanthanides-based antiferromagnets. Lanthanides (also known as rare-earths) are a group of 15 different elements in the periodic table, from element number 57 (La) to 71 (Lu). They share almost identical surrounding itinerant conduction electrons, and the only difference among them is the number of $4f$ electrons in the core part of an atom. Lanthanides, especially heavy lanthanides e.g. Gd, Tb, Dy and Ho, have exceptionally large magnetic moments, which makes them increasingly important in technologies. However, this large magnetic moment is derived from spatially localized $4f$ electrons. Due to this spatially localized nature of $4f$ electrons, $4f$ moments from different lanthanide atoms can interact only indirectly taking surrounding itinerant conduction electrons as a mediator. Since magnetism is derived from ordered structure of a group of magnetic moments from huge number of atoms, to understand lanthanides magnetism, it is essential to understand the nature of this indirect coupling, which is also known as the indirect exchange coupling.

In $4f$ antiferromagnets, the indirect exchange coupling is intricately woven (i) within a lanthanide atom, between localized $4f$ and itinerant electrons, and (ii) between $4f$ electrons from different lanthanide atoms to maintain the complex self-cancelling antiferromagnetic $4f$ spin ordering. In this thesis, we are going to study the nature of these intra- and inter-atomic indirect couplings in $4f$ antiferromagnets. We will introduce how the indirect RKKY coupling forms and determines the magnetic structure in lanthanides in Chapter 2 in detail.

Time-resolved experimental studies

Any perturbation to a system at equilibrium (or in physicists' language, a ground state) causes dynamics; the system departs from the ground state and subsequently returns to it assuming the perturbation is not strong enough to bring the system to entirely new ground state. For example, two masses coupled with a spring oscillates if we apply a force on the system. From the response of the system, we can understand the system in depth; the force responsible for maintaining equilibrium state (spring force), the strength of the coupling (spring constant) etc. Same logic applied to magnetic materials. By measuring the timescale of amplitude of the interactions contributing to

magnetization dynamics, we can deduce the physical interactions relevant for the magnetism of a given magnet, and quantitatively analyze the mechanism of the corresponding physical interactions.

For a microscopic understanding of lanthanide magnetism, it is essential to understand the nature and role of the indirect exchange coupling. Various experimental approaches have been employed to determine such couplings in lanthanides; scanning tunneling spectroscopy, spin-resolved photoemission spectroscopy, angle-resolved photoemission spectroscopy, and resonant elastic x-ray scattering [Bod+99; Kim+92; Mai+02; Döb+07; Ott+06]. However, these time-integrating static techniques average out any relevant microscopic interactions upon perturbation (e.g. heating, external field application). Therefore, it is challenging to disentangle the contributions from various degrees of freedom within a magnetic material, which hinders us to systematically study the role of intra- and inter-atomic couplings of the indirect exchange coupling in lanthanide magnetism.

According to the uncertainty principle imposed on the relation between the energy and time ($\Delta E \Delta t \geq \hbar$, where $\hbar \sim 10^{-34}$ $J \cdot s$ is the Planck constant), for studying the indirect exchange interaction, which is at electronvolt range ($\lesssim 10^{-19}$ J), we have to employ time-resolved experimental techniques on femtosecond timescales ($\gtrsim 10^{-15}$ s). Therefore, in this thesis, by employing state-of-the-art laser setup and synchrotron facilities, we are going apply an ultrashort external stimulus to $4f$ antiferromagnets and measure their responses on femtosecond timescale in order to study the role of the indirect exchange coupling in $4f$ antiferromagnetism, more specifically, in ultrafast spin dynamics of 4 antiferromagnets. It is possible that more than one interactions are associated with the characteristic timescales, which limits the outcome of the time-resolved studies. We will overcome this difficulty by (i) doing comparative analyses of a family of nine different $4f$ antiferromagnets $Ln\,T_2Si_2$, (ii) combining two complementary time-domain techniques, surface-sensitive time- and angle-resolved photoemission spectroscopy (trARPES) and bulk-sensitive time-resolved resonant elastic magnetic x-ray diffraction (trRXD), and (iii) applying theoretical calculations either within a microscopic three temperature model (M3TM) or within a density functional theory (DFT) for qualitative and quantitative analyses of the experimental results. We will introduce the family of $4f$ antiferromagnets $Ln\,T_2Si_2$ and the microscopic three temperature in Chapter 2 and the experimental techniques that we employed, trARPES and trRXD, in Chapter 3. DFT calculations were conducted by Prof. Dr. Arthur Ernst consulting with us about the details of the experimental finding. Details for the density functional theory calculations are provided in Appendix A.

Exploring indirect exchange interaction in $4f$ antiferromagnets

Here we introduce the content of main chapters to briefly explain how comparative analysis of ultrafast spin dynamics of a family of $4f$ antiferromagnets $Ln\,T_2Si_2$ and combining surface-sensitive trARPES and bulk-sensitive trRXD techniques allow us to explore the role of the indirect exchange coupling in ultrafast spin dynamics of $4f$ antiferromagnets.

Exchange scaling of ultrafast angular momentum transfer rate in $4f$ antiferromagnets (Chapter 4)

Spatially localized $4f$ magnetic moments are the source of the indirect exchange interaction. We employ a family of $4f$ antiferromagnets $Ln Rh_2Si_2$ (Ln = Pr, Nd, Sm, Gd, Tb, Dy and Ho) which share almost identical lattice parameters and antiferromagnetic structure. By swapping Ln ions, we vary the number of the $4f$ electrons in Ln ions in the compounds, which determines the size of the $4f$ moment. By comparing ultrafast spin dynamics of $Ln Rh_2Si_2$ employing trRXD and with first-principles calculations within a DFT, we show that antiferromagnetic (AF) indirect exchange coupling between the nearest AF coupled Ln $4f$ moments within the compounds scales with the angular momentum transfer rate upon photoexcitation. This shows that direct spin transfer between antiferromagnetically coupled Ln $4f$ moments efficiently quenches angular momentum (i.e. magnetic moment) during ultrafast spin dynamics. Contribution of the phonon-mediated spin-flip

scattering, the main angular momentum transfer mechanism for ferromagnets, is also observed implying that the demagnetization process is driven by the both processes.

Singling out the role of the conduction electrons in ultrafast spin dynamics of $4f$ antiferromagnets (Chapter 5)

Itinerant conduction electrons are the mediator of the indirect exchange interaction. We employ a family of $4f$ antiferromagnets GdT_2Si_2 (T = Co (3d), Rh (4d) and Ir (5d); group 9 elements) which again share almost identical lattice parameters and comparably similar antiferromagnetic structure. By swapping the transition metal ions, we modify the character of the conduction electrons and measured ultrafast spin dynamics of GdT_2Si_2 employing trRXD. Upon optical excitation, $GdRh_2Si_2$ exhibit the largest angular momentum transfer rate followed by $GdIr_2Si_2$ and $GdCo_2Si_2$. First-principles calculations within a density functional theory show that transition metal ions significantly change the electronic density of states (eDOS) of Gd $5d$ electrons around the Fermi energy (E_F), which has a scaling relation with the experimental angular momentum transfer rate. The modification of the eDOS of Gd $5d$ electrons around E_F results significant change in non-local susceptibility of conduction electrons, and in consequence, in the strength of the antiferromagnetic indirect exchange coupling, which explains our experimental finding based on the conclusion from Chapter 4.

Robust magnetic order upon ultrafast excitation of an $4f$ antiferromagnet (Chapter 6)

The microscopic three temperature (M3TM) explains that ultrafast spin dynamics can be simulated by thermal interactions and angular momentum exchange between the three subsystems in magnetic materials, electrons, lattice and spins. To test the capability and limitations of the M3TM, we measured femtosecond dynamics of transient electronic temperature, exchange splitting of a Si-derived metallic surface state, and long-range $4f$ antiferromagnetic ordering of $GdRh_2Si_2$ employing trARPES and trRXD, and applied the M3TM to our experimental results. Resemblance of the demagnetization timescale of surface exchange splitting and bulk $4f$ AF ordering suggests a strong on-site indirect exchange coupling between localized $4f$ and itinerant conduction electrons. While the M3TM qualitatively well describes the experimental results, to explain robust magnetic ordering even when the equilibrated electronic temperature is above the Néel temperature T_N for hundreds of picoseconds (1 ps = 10^{-12} s), we phenomenologically introduce transiently increased T_N^*, which scales with the fluence of the optical excitation. Though it may not reflect actual increase of T_N in physical reality, we speculate that this may imply transient increase of indirect exchange couplings upon photoexcitation.

Disparate dynamics of exchange coupling and magnetic order in a frustrated $4f$ antiferromagnet (Chapter 7)

From first-principles calculations within a density functional theory (Chapter 5), we learned that $GdCo_2Si_2$ has a frustrated spin structure due to localization of $3d$ electrons of Co ions, which means that there are more than one possible ground states for the antiferromagnetic structure. Statics and ultrafast dynamics of long-range Gd $4f$ ordering in $GdCo_2Si_2$ were measured employing (tr)RXD. Since its exact spin structure is not known yet, we try identify the AF spin structure of $GdCo_2Si_2$ by comparing the experimental diffraction intensity with structure factor calculation of one candidate spin structure, a long-range helimagnet along the c-axis of the crystal structure repeating 483 rotations every 500 unit cells. Upon equilibrium heating, both the period of the helix and AF order evolve; the period monotonously increases and the AF order quenches. However, upon optical excitation, the two physical parameter exhibit disparate dynamics for the early 200 ps; while the period decreases for the first 30 ps and increases subsequently, the AF order exhibits simply

demagnetization dynamics. Since period is determined by indirect exchange coupling configuration in $GdCo_2Si_2$, this implies disparate dynamics of indirect exchange couplings and long-range AF order for 200 ps i.e. a 200-ps-long non-thermal state of Gd $4f$ moments upon photoexcitation.

This page is intentionally left blank.

Chapter 2

Theoretical backgrounds for studying ultrafast spin dynamics of 4f antiferromagnets

Disclaimer: A part of this chapter was published in "Exchange scaling of ultrafast angular momentum transfer in 4f antiferromagnets" *Nature Materials* **21**, 514–517 (2022) and in "Robust magnetic order upon ultrafast excitation of an antiferromagnet" arXiv: 2207.00789, (2022).

Lanthanides have exceptionally large magnetic moments compared to $3d$ transition metals. However, the majority of the magnetic moments reside in spatially localized $4f$ electrons. Due to its localized nature, the $4f$ electrons interact indirectly via itinerant conduction electrons. This indirect relation is described by the indirect Ruderman-Kittel-Kasuya-Yosida (RKKY) exchange interaction [JM91]. In this chapter, first, I will introduce the indirect RKKY exchange interaction, the main physical interaction governing the magnetism of the $4f$ antiferromagnets. Then, I will introduce the sample system that we employed for this thesis LnT_2Si_2 and discuss the validity and limitations of a direct comparison between the $4f$ dynamics of this family of $4f$ antiferromagnets. Lastly, in order to describe intricate energy and angular momentum flow in $4f$ antiferromagnets upon photoexcitation, we applied a microscopic three temperature model (M3TM) based on the Landau-Lifshitz-Bloch (LLB) equation to our experimental results (Chapter 6). Therefore, I will introduce the M3TM and the LLB equation, and explain how the M3TM operates by providing an exemplary application case.

2.1 Indirect RKKY exchange interaction

Indirect RKKY exchange interaction was introduced by Ruderman and Kittel for explaining an induced spin polarization of the conduction electrons by a nuclear spin [RK54]. Soon after Kasuya and Yosida applied this idea to explain a spin polarization of conduction electrons induced by a spatially localized unfilled electronic shell [Kas56; Yos57]. Kasuya's work is directly about $4f$ magnets, the main interest of this thesis. In honor of the four scientists who developed this idea of indirect exchange interaction, we call this interaction RKKY interaction as well. Readers interested may refer [Kas56; JM91; Gim+21] for detailed discussion of the RKKY interaction.

Assuming that the conduction electrons are nearly free-electron-like and that the $4f$ electrons are spatially localized and that the interaction between the 4f electrons in the different lattice points is small [Kas56], the indirect exchange interaction between the conduction and the localized $4f$ electrons can be described as a form of the following equation:

$$\mathcal{H}_{sf}(i) = -\frac{2}{N}\int I\left(\vec{r}-\vec{R}_i\right)\vec{S}_i\cdot\vec{s}\,(\vec{r})\,d\vec{r} \tag{2.1}$$

where N is the number of ions, $\vec{S}_i$, $\vec{s}(\vec{r})$ are the $4f$ electrons spin at i-th lattice and the conduction electron spin density, respectively. The exchange integral $I\left(\vec{r}-\vec{R}_i\right)$ depends on the overlap of the $4f$ electrons at i-th lattice and the conduction electron charge clouds [JM91]. We can see Eq. (2.1) in different perspective; an effective inhomogeneous magnetic field $\vec{H}_i(\vec{r})$ from the $4f$ electrons at i-th lattice interact with an induced magnetic moment distribution of the conduction electron $\vec{\mu}(\vec{r})$ at $\vec{r}$:

$$\mathcal{H}_{sf}(i) = -\int \vec{H}_i(\vec{r}) \cdot \vec{\mu}(\vec{r})\, d\vec{r}, \tag{2.2}$$

where

$$\vec{H}_i(\vec{r}) = \frac{1}{N\mu_B} I\left(\vec{r}-\vec{R}_i\right)\vec{S}_i \tag{2.3}$$

$$\mu_{i\alpha}(\vec{r}) = \frac{1}{V}\sum_{\beta}\int \chi_{\alpha\beta}\left(\vec{r}-\vec{r'}\right) H_{i\beta}\left(\vec{r'}\right) d\vec{r'}, \tag{2.4}$$

where $\chi_{\alpha\beta}$ is the non-local susceptibility tensor component for the conduction electrons and V the volume [JM91]. This induced magnetic moment of the conduction electrons at $\vec{r}$ can interact with $4f$ electrons at other lattice point, say j-th lattice with $\vec{S}_j$ leading to a coupling between the i-th and j-th lattice points:

$$\mathcal{H}_{ij} = -\int \vec{H}_j(\vec{r}) \cdot \vec{\mu}_i(\vec{r})\, d\vec{r} = -\frac{1}{V}\sum_{\alpha\beta}\int\int H_{j\alpha}(\vec{r})\,\chi_{\alpha\beta}\left(\vec{r}-\vec{r'}\right) H_{i\beta}\left(\vec{r'}\right) d\vec{r}d\vec{r'}, \tag{2.5}$$

where $\vec{H}_j$ is an effective magnetic field from the $4f$ electrons at j-th lattice (Eq. (2.3)). Neglecting any spin-orbit interaction of the conduction electrons and assuming that the crystal is not magnetized yet, $\chi_{\alpha\beta}$ can be assumed to be a scalar. With Fourier transformation of the spatial distribution of non-local susceptibility $\chi(\vec{r})$ and overlap integral $I(\vec{r})$, we can generalize Eq. (2.5) into RKKY interaction between $4f$ moments at different lattice sites $\mathcal{H}_{ff}$ by summing the interaction only once at each site, all over the lattice sites [JM91]:

$$\begin{aligned}
\mathcal{H}_{ff} &= -\frac{1}{2}\frac{V}{N^2\mu_B^2}\frac{V}{(2\pi)^3}\sum_{ij}\int \chi(\vec{q})\, I(\vec{q})\, I(-\vec{q})\, e^{i\vec{q}\cdot\left(\vec{R}_i-\vec{R}_j\right)}\vec{S}_i\cdot\vec{S}_j d\vec{q} && (2.6)\\
&= -\frac{1}{2N}\sum_{\vec{q}}\sum_{ij}\mathcal{J}_S(\vec{q})\, e^{i\vec{q}\cdot\left(\vec{R}_i-\vec{R}_j\right)}\vec{S}_i\cdot\vec{S}_j && (2.7)\\
&= -\frac{1}{2}\sum_{ij}\mathcal{J}_S(ij)\,\vec{S}_i\cdot\vec{S}_j && (2.8)
\end{aligned}$$

where

$$\mathcal{J}_S(ij) = \frac{1}{N}\sum_{\vec{q}}\mathcal{J}_S(\vec{q})\, e^{i\vec{q}\cdot\left(\vec{R}_i-\vec{R}_j\right)} \tag{2.9}$$

and

$$\mathcal{J}_S(\vec{q}) = \frac{V}{N\mu_B^2}\left|I(\vec{q})\right|^2\chi(\vec{q}). \tag{2.10}$$

Therefore, we can argue that the strength of the RKKY interaction between the $4f$ moments depends both on the overlap integral between the conduction and $4f$ electron wave functions $I(\vec{q})$ and on the non-local susceptibility of the conduction electrons $\chi(\vec{q})$. The non-local susceptibility $\chi(\vec{q})$ is a response function of the conduction electrons with respect to the inhomogeneous effective magnetic field due to a $4f$ moment, which can be written, in this case, as following [JM91]:

$$\chi(\vec{q}) = \frac{2\mu_B^2}{V}\sum_{nn'\vec{k}}\frac{f_{n\vec{k}}-f_{n'\vec{k}-\vec{q}}}{\epsilon_{n'}\left(\vec{k}-\vec{q}\right)-\epsilon_n\left(\vec{k}\right)} \tag{2.11}$$

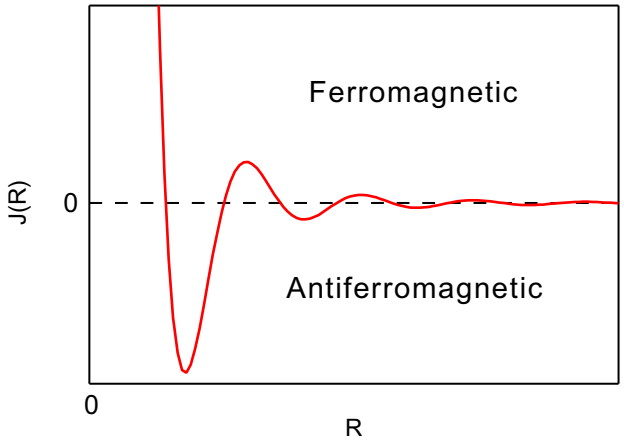

Figure 2.1: Distance-dependent behavior of the RKKY interaction $\mathcal{J}(R)$ (Eq. (2.13)). Distance R indicates the distance between two $4f$ moments. If $\mathcal{J}$ is positive (negative), the ground state is (anti-)ferromagnetic.

where $f_{n\vec{k}}$, $\epsilon_{n\vec{k}}$ are the Fermi-Dirac distribution function and the energy of the conduction electrons with a crystal momentum $\hbar\vec{k}$, respectively. Eq. (2.11) shows that the largest contribution to the sum comes from pairs of electronic states of energies very close to the Fermi level [JM91]. This tells us that while the sum counts for the entire states, the non-local susceptibility of the conduction electron $\chi(\vec{q})$ around the Fermi level contributes the most, hence determines the strength of the indirect RKKY exchange interaction between the $4f$ moments (Eq. (2.10)).

Using Eqs. (2.10) and (2.11), Eq. (2.9) can be rewritten as

$$\mathcal{J}_S(ij) = \frac{2}{N^2}\sum_{\vec{q}}\sum_{nn'\vec{k}} |I(\vec{q})|^2 \frac{f_{n\vec{k}} - f_{n'\vec{k}-\vec{q}}}{\epsilon_{n'}\left(\vec{k}-\vec{q}\right) - \epsilon_n\left(\vec{k}\right)} e^{i\vec{q}\cdot\left(\vec{R}_i - \vec{R}_j\right)}. \tag{2.12}$$

Since we assumed that the conduction electrons are near-free-electron-like, $\epsilon_{\vec{k}} = \hbar^2k^2/2m$. Replacing the momentum summation by integration, in the low temperature approximation where the Fermi-Dirac distribution is close to a rectangular shape, we can obtain [Gim+21]

$$\mathcal{J}_S(ij) \propto \frac{1}{R^4}\left(\sin(2k_FR) - 2k_FR\cos(2k_FR)\right). \tag{2.13}$$

where k_F is the Fermi momentum, and R is the distance between $4f$ moments. This means that the RKKY interaction is long-range interaction that exhibits oscillatory behavior with respect to the distance between the $4f$ moments. The oscillatory behavior tells us that the ground state of $4f$ magnetic materials can be either ferromagnetic ($\mathcal{J}_S(ij) > 0$) or antiferromagnetic ($\mathcal{J}_S(ij) < 0$) depending on the distance between the $4f$ moments (Figure 2.1). In this thesis, we study a family of $4f$ antiferromagnets $Ln\,T_2\mathrm{Si}_2$, which will be introduced in detail in the following subsection 2.1.1.

2.1.1 Sample system: $4f$ antiferromagnets

A systematic investigation into the role of $4f$ occupation and conduction electrons on ultrafast magnetization dynamics is essential to elucidate how the indirect RKKY exchange interaction governs the ultrafast spin dynamics. Previous attempts to address this question have focused on ferromagnetic (FM) lanthanide metals [Wie+11]. This limits the comparison to three heavier lanthanides (Gd $4f^7$, Tb $4f^8$ and Dy $4f^9$) and rules out demagnetization channels that do not involve interactions with the crystal lattice, such as the transfer of angular momentum between different magnetic sublattices. While reports of ultrafast $4f$ spin dynamics in antiferromagnets

elements	a (Å)	c (Å)	Structure (300 K)	T_N (K)	T_C (Å)	gJ (μ_B)	Ref.
Pr	3.672	11.833	dhcp	0.05	N/A	3.2	[JM91]
Nd	3.658	11.797	dhcp	19	N/A	3.27	[JM91]
Sm	3.628	26.233	rhom	106	N/A	0.71	[JM91]
Gd	3.634	5.785	hcp	N/A	293	7	[JM91]
Tb	3.606	5.697	hcp	230	220	9	[JM91]
Dy	3.592	5.650	hcp	179	89	10	[JM91]
Ho	3.578	5.618	hcp	132	20	10	[JM91]

Table 2.1: Crystal and magnetic structure parameters of elemental lanthanides. a, c, V are the horizontal and vertical lattice constants, and unit cell volume, respectively. Either the Curie temperature T_C or the Néel temperature T_N is presented depending on the magnetic phases they exhibit. The theoretical saturated $4f$ moment gJ are also shown. dhcp: Double hexagonal close-packed, rhom: Rhombohedral, hcp: Hexagonal close-packed.

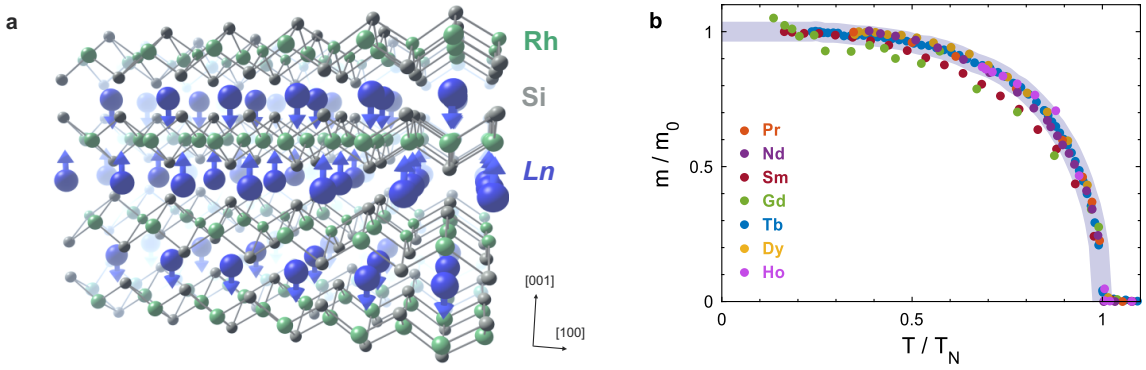

Figure 2.2: (a) Crystal structure of $Ln\mathrm{Rh_2Si_2}$. (b) Temperature dependence of the $\mathrm{Ln^{3+}}$ sites' ordered $4f$ moment in $Ln\mathrm{Rh_2Si_2}$, exhibiting mean-field-like behaviour. The axes are normalized by each material's saturated moment m_0 and Néel temperature T_N. The data were extracted from temperature-dependent resonant magnetic x-ray diffraction experiments. The gray line is a guide for the eye representing mean-filed behaviour. Reproduced with permission from Springer Nature [Win+22].

are scarce [Ret+16; Thi+17; Win+20], one experiment performed on an antiferromagnetic (AF) lanthanide suggested the existence of this direct spin transfer channel, which has been proposed as a route to overcome speed bottlenecks associated with the lattice [Thi+17]. However, a systematic study of elemental lanthanides is hindered by the large variety of different crystal structure and magnetic phases they exhibit (listed in Table 2.1) such as spin helices and spin spirals, further complicating a meaningful comparison.

In this regard, intermetallic compounds $Ln\,T_2\mathrm{Si_2}$ solves this trouble (Ln: lanthanides; T: transition metals). $Ln\,T_2\mathrm{Si_2}$ is a family of quasi-2D intermetallic material with a layered tetragonal crystal structure of $\mathrm{ThCr_2Si_2}$ type (space group I4/mmm (#139); a = b $\sim$ 4 Å, c $\sim$ 10 Å), where Ln atomic layers are separated by strongly bonded Si-T-Si blocks along the [001] direction as shown in Fig. 2.2-a [FN83; FN84]. The properties are listed in Table 2.2.

Furthermore, below T_N, $Ln\,T_2\mathrm{Si_2}$ undergo a phase transition into an antiferromagnetic (AF) state. Their magnetic structure consists of ferromagnetic Ln layers in the ab-planes aligned antiferromagnetically to each other along the c-axis, i.e. along the [001] direction (Table 2.2) [Kli+17; Sic+18]. Their collinear, compensated AF arrangement exhibits a mean-field-like temperature dependence (Figure 2.2-b) and allows neglecting stray fields and domain effects, which are necessary when considering ferromagnets. As such, these materials can be regarded as a lattice of AF-ordered

LnT_2Si_2	a (Å)	c (Å)	V (Å)	T_N (K)	gJ (μ_B)	Ln-Ln (Å)	Ref.
$PrRh_2Si_2$	4.079	10.14	168.68	68	3.2	5.83	[Kli+20; Hos+09]
$NdRh_2Si_2$	4.069	10.11	167.39	58	3.27	5.82	[Kli+20; Szy+84]
$SmRh_2Si_2$	4.055	10.04	165.09	64	0.71	5.78	[Kli+20]
$GdCo_2Si_2$	3.91	9.81	149.98	45	7	/	[Czj+89]
$GdRh_2Si_2$	4.042	9.986	163.15	107	7	5.75	[Kli+20]
$GdIr_2Si_2$	3.97	9.90	156.03	86	7	/	[Kli+20]
$TbRh_2Si_2$	4.037	9.95	162.16	94	9	5.73	[Kli+20; ŚLS83]
$TbIr_2Si_2$	4.143	10.155	174.30	82	9	/	[Kli+20; ŚLS83]
$DyRh_2Si_2$	4.022	9.90	160.15	52	10	5.71	[Kli+20]
$HoRh_2Si_2$	4.015	9.89	159.43	29	10	5.70	[Kli+20]
$HoIr_2Si_2$	4.043	9.884	161.56	22	10	/	[KBK18]

Table 2.2: Crystal and magnetic structure parameters of LnT_2Si_2 compounds studied in this thesis. a, c, V are the in-plane and out-of-plane tetragonal lattice constants, and unit cell volume, respectively. The Néel temperature T_N, the theoretical saturated $4f$ moment gJ and the distance between Ln ions in adjacent layers are also shown. Reproduced with permission from Springer Nature [Win+22].

Ln ions in a T_2Si_2 cage and can serve as an ideal test bed for comparing dynamics of the $4f$ moments with varying $4f$ occupation and the conduction electrons layers in between. Unlike the elemental lanthanides, these compounds share almost identical magnetic and lattice structures, which makes it much easier to apply comparative analysis of their ultrafast spin dynamics. There are two factors to be clarified, however:

Local ion anisotropy The antiferromagnetic arrangement of spins within the unit cell was determined through the azimuthal dependence of the [0 0 l] magnetic reflection, where l=1 for all the $4f$ antiferromagnets studied in this thesis, unless specified. All materials except $SmRh_2Si_2$, $GdRh_2Si_2$ and $GdIr_2Si_2$ exhibited no azimuthal modulation of the diffraction intensity, indicating that the local anisotropy aligns the spins along the c axis (alternatingly parallel or antiparallel to it). For $SmRh_2Si_2$, $GdRh_2Si_2$ and $GdIr_2Si_2$, it is reported that the $4f$ spins are aligned within the ab plane, while spins of adjacent planes remain antiparallel to each other [Lec87]. In the case of $GdRh_2Si_2$ the direction along which the spins point within the ab plane varies as a function of temperature allowing deterministic control of the AF spin arrangement, as shown in Ref. [Win+20]. The difference lays in the low anisotropy of the $4f$ shell of Gd and Sm ions compared to other Ln ions. This does not modify the on-site exchange coupling between the $4f$ electrons and the conduction electrons, so the RKKY interaction is not affected, justifying the systematic comparison between the materials' spin dynamics we will present in Chapters 4 and 5. Furthermore, magnetic anisotropy energies in these systems are significantly smaller than the RKKY coupling energies.

Additional magnetic transitions Two of the probed materials ($HoRh_2Si_2$, $DyRh_2Si_2$) exhibit an additional canted antiferromagnetic phase at very low temperatures, in which the $4f$ moments are tilted away from the (001) direction. This phase is easily identifiable, because below its transition temperature, the intensity of the (001) magnetic reflection changes significantly. In both cases we conducted the experiments above this transition in the normal phase that is equivalent to the other materials in the LnT_2Si_2 series in order to avoid this complication.

Given the above considerations, LnT_2Si_2 offer a unique playground for the study of $4f$ antiferromagnets: By swapping the lanthanide ions, we can change the number of localized $4f$ electrons (Chapter 4), while by swapping the transition metal ions we can control the character of itinerant

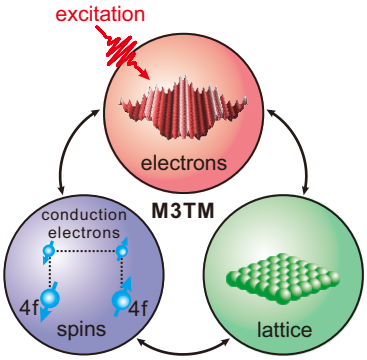

Figure 2.3: M3TM for $4f$ antiferromagnets

conduction electrons. Very importantly, these two parameters can be explored in a rather consistent magnetic and lattice environment. Assuming that the RKKY interaction governs the ultrafast spin dynamics of these compounds, as it is shown the case for elemental heavy lanthanides [ALW21; Fri+15; Thi+17; Ret+16; Wie+11], we can clearly single-out the contribution of the $4f$ and the conduction electrons from comparison of the ultrafast spin dynamics of LnT_2Si_2.

2.2 Microscopic three-temperature model for antiferromagnets

Since magnetic moments are derived from spin and orbital angular momentum of electrons, the most important question in ultrafast spin dynamics is "*To where does the angular momentum go?*" Especially for $4f$ magnets which have exceptionally large magnetic moments, this angular momentum transfer is the bottleneck process of the entire ultrafast spin dynamics. The external energy from optical excitation heats up a magnet, and spin structure disorders subsequently. Then how do we physically formulate the relation between energy, temperature and spin ordering? As one attempt of various theoretical approaches, in this section, I will introduce the microscopic three temperature model, which provides an intuitive picture on this relation and has successfully described various experimental ultrafast spin dynamics [Koo+10; Shi+20; Atx+14; Che+19; Fri+20; Sul+12; Rad+11; Fri+15; Atx+10].

To explain the experimental ultrafast spin dynamics of FM Ni phenomenologically, Beaurepaire et al. introduced the three-temperature model (3TM) [Bea+96]. By introducing effective temperatures for the transient electronic, lattice and spin degrees of freedom (see Fig. 2.3), the 3TM explains that photo-induced ultrafast magnetization dynamics can be described by mutual energy transfer between three different subsystems in a magnet, electrons, lattice and spins. While solving three coupled differential equations of thermal interactions provides an easy-to-understand picture for ultrafast spin dynamics, it has a few critical issues: First, spin temperature is not always equivalent to magnetization. It may be equivalent for $3d$ magnets which have relatively small magnetic moments and high phase transition temperature (above room temperature). However, $4f$ magnets have large magnetic moments and low phase transition temperature (below room temperature). Since spin heat capacity is derived from statistical distribution of spins, it is almost non-existent above the phase transition temperature where the sample is totally demagnetized. In case a material exhibits robust magnetic order even above the phase transition temperature during ultrafast spin dynamics [And+15; ALW21; Thi+17], the equivalence between the spin temperature and magnetization is no longer valid. Second, and most importantly, the model does not explain how the angular momentum quenches or where the angular momentum is transferred to during ultrafast spin dynamics.

The microscopic three-temperature model (M3TM) improved the 3TM by considering momentum conservation during the ultrafast magnetization dynamics via the phonon-mediated Elliott-Yafet-like spin-flip scattering substituting a phenomenological spin temperature with magnetization

[Koo+10]. As the name of the scattering implies, in the M3TM, the electron spin is flipped by the scattering with a phonon dumping angular momentum to the lattice vibration [Dor+19; Koo+10]. Such formulations are related to the Landau-Lifshitz-Bloch (LLB) equation, where the specifics of the couplings to the electrons and phonons in magnets are encoded in the damping parameter of the macrospin dynamics, which will be explained in the subsequent subsection [Atx+10; AHN16; AC11; Nie+14]. M3TMs also explain the two-step demagnetization behavior typically found in lanthanides, such as Gd [Wie+11], due to enhanced spin-flip scattering within a non-thermal system [Koo+10]. However, as these materials are characterized by indirect RKKY exchange interaction between localized $4f$ electrons with large magnetic moments, mediated through weakly spin-polarized conduction electrons, distinct dynamics of these magnetic subsystems also needs to be considered, and has been recently reported for Gd and Tb [Fri+20]. Since the model has been applied mostly to ferromagnetic materials, we applied a modified version of M3TM based on a LLB equation to take account of the direct spin transfer channel in antiferromagnets, which will be explained in the following subsection.

2.2.1 Landau-Lifshitz-Bloch equation for antiferromagnets

Landau-Lifshitz-Bloch equation is a macroscopic counterpart of stochastic Landau-Lifshitz-Gilbert (s-LLG) equation, which phenomenologically describes atomistic spin dynamics. The s-LLG equation is an equation of motion describing precession, damping and relaxation of a spin under external magnetic field application:

$$\frac{\partial \vec{S}_i}{\partial t} = \frac{-\gamma}{1+\alpha^2}\left(\vec{S}_i \times \vec{H}_i + \frac{\alpha}{S_i}\vec{S}_i \times \left(\vec{S}_i \times \vec{H}_i\right)\right), \tag{2.14}$$

where γ=1.76×10^{11}(T·s)$^{-1}$, α are the gyromagnetic ratio, and the damping parameter at atomic level, respectively. $\vec{S}_i = \vec{\mu}_i/\mu_S$ is the normalized spin vector made out of the atomic magnetic moment μ_S, and $\vec{H}_i = \vec{B}_i^{ex} + \vec{\zeta}$ is the effective magnetic field including contributions from exchange interaction B_i^{ex}, crystalline anisotropies, and external magnetic field [AHN16]. Here, the Weiss field $\vec{B}_i^{ex} = -\frac{\partial \mathcal{H}}{\partial S_i}$ is related to the underlying spin-Hamiltonian $\mathcal{H}$. In order to take thermal excitation effect into account, Langevin field $\vec{\zeta}$ representing thermal noise is introduced in the effective field. The Langevin field $\vec{\zeta}$ is assumed to have a white noise properties, i.e. [AHN16]

$$\langle \zeta_x(t) \rangle = 0 \tag{2.15}$$

$$\left\langle \zeta_x(t)\zeta_y(t') \right\rangle = \frac{2\alpha k_B T}{\mu_S \gamma}\delta_{xy}\delta(t-t') \tag{2.16}$$

where x and y are Cartesian components, and k_B, T are the Boltzmann constant, the temperature of the heat bath to which the spins are coupled, respectively [AHN16].

The first term of Eq. (2.14) is to describe a precession, which can be derived from Heisenberg equation of motion in the classical limit, and the second term includes the relaxation of the magnetization phenomenologically through damping, which describes a dissipation of energy and angular momentum to electronic and to phononic degrees of freedom [AHN16].

While s-LLG equation allows atomistic description of spin dynamics, it is computationally costly unless we moderately limit the lattice size of the system. To overcome this drawback, Landau-Lifshitz-Bloch (LLB) equation is developed as a macroscopic approach. To construct the LLB equation, we have to assume the mean-field-approximation. In other words, all individual spins $\vec{S}_i$ are lumped into one macrospin $\vec{m}$, and the effective field $\vec{H}_{eff}$ acts on each spin with equal amount (Figure 2.4). After some algebra, the LLB equation for a ferromagnet looks [AHN16]

$$\frac{1}{\gamma}\frac{d\vec{m}}{dt} = -\left[\vec{m} \times \vec{H}_{eff}\right] + \alpha_{\parallel}\frac{\left(\vec{m}\cdot\vec{H}_{eff}\right)\vec{m}}{m^2} - \alpha_{\perp}\frac{\left[\vec{m} \times \left[\vec{m} \times \vec{H}_{eff}\right]\right]}{m^2} \tag{2.17}$$

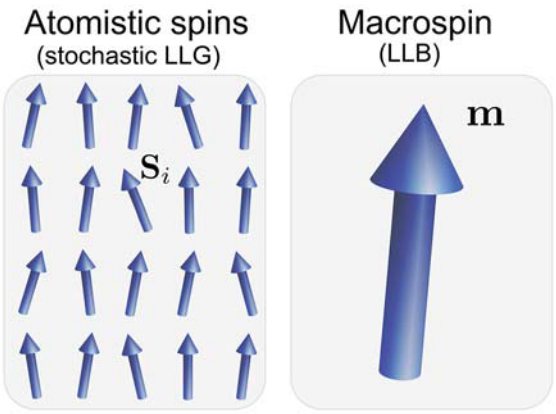

Figure 2.4: Left: Schematic representation of the atomistic spin model. The dynamics of each atomic spin $\vec{S}_i$ is given by the stochastic Landau-Lifshitz-Gilbert equation of motion (Eq. (2.14)). Right: Schematic representation of the macrospin model. The dynamics of the average magnetization $\vec{m} = \sum_i \left\langle \vec{S}_i \right\rangle / N$ is governed by the LLB equation (N, number of spins) Reproduced with permission from IOP Publishing [AHN16].

where $\alpha_\perp$, $\alpha_\parallel$ are transverse and longitudinal damping parameters, respectively. These two different damping parameters are the most important feature of the LLB equation. The transverse damping parameter $\alpha_\perp$ (also known as the LLG damping parameter) describes the relaxation of the ferromagnetic resonance mode, and increases with temperature [AC11]. The longitudinal damping parameter $\alpha_\parallel$ describes the behaviour of the high-frequency spin waves under a strong exchange field, which makes its corresponding relaxation time $\tau_\parallel$ increase with temperature (also known as 'critcal slowing down') [AC11]. This critical slowing down has been observed in ultrafast spin dynamics of $Ln\,T_2\mathrm{Si}_2$ as well (Chapters 4 and 5) and discussed in detail in subsection 4.2.2.

Another notable feature of the LLB equation is the coupling parameter λ encoded in the two damping parameters; the damping parameters have a linear relation with the coupling parameter λ [AHN16]. Since λ contains matrix elements describing the scattering events, it is proportional to the spin-flip scattering rate due to the interaction with the environment, hence it can be temperature-dependent [AC11]. Unlike Koopmans' M3TM, which explains that the demagnetization dynamics is driven by the Elliot-Yafet-like phonon-mediated spin-flip scattering, the LLB equation (and its atomistic counterpart, s-LLG equation) does not distinguish the origin of the spin-flip scattering. This flexibility helps to apply the LLB equation to antiferromagnetic cases, which will be discussed subsequently.

Exchange-enhancement in antiferromagnets

Direct spin transfer channel between different magnetic sublattices in antiferromagnets can enhance demagnetization rate upon optical excitation as shown experimentally for Dy [Thi+17]. LLB equation or s-LLG equation explains that this is due to exchange-enhancement of the damping parameter from the direct spin transfer [JA22a; AHN16]. In this subsection, we briefly derive this enhancement effect. Since s-LLG equation involves only one damping parameter, it is more convenient to show this. As s-LLG equation is an atomistic counterpart of the LLB equation, derivation from the s-LLG equation is more or less equivalent to that from the LLB equation. Readers interested in detailed discussion of enhancement effect in the transverse and longitudinal damping parameters of the LLB equation may refer [Sch+12; Atx+14; AHN16].

Upon rapid heating of electrons and lattice from optical excitation, the magnetic order in ferromagnets evolves according to $\frac{d\vec{m}}{dt} \sim \alpha_{fm}\vec{H}_{eff}$ (Eq. (2.14)). In this picture, the effective magnetic field $\vec{H}_{eff}$, which includes the thermal excitation, is driving the spin dynamics at a rate

of α_{fm} towards the next equilibrium point [JA22a]. This demagnetization picture is still valid for antiferromagnets, however, at a different rate due to the direct spin transfer channel.

Except $GdCo_2Si_2$, antiferromagnetic (AF) $Ln\,T_2Si_2$ that we study in this thesis consists of two oppositely aligned magnetic sublattices. Considering the direct spin transfer between the two sublattices, the spin dynamics expression should be modified as following: $\frac{d\vec{m}_\uparrow}{dt} \sim \alpha_\uparrow \vec{H}_\uparrow + \alpha_{ex}\left(\vec{H}_\uparrow - \vec{H}_\downarrow\right)$, where α_{ex} represents the damping parameter of inter-atomic spin transfer between $\uparrow$ and $\downarrow$ sublattices [JA22a]. Since $\vec{H}_\downarrow = -\vec{H}_\uparrow$ in AF $Ln\,T_2Si_2$, the resulting spin dynamics expression is

$$\frac{d\vec{m}_\uparrow}{dt} \sim \alpha_\uparrow \vec{H}_\uparrow + \alpha_{ex}\left(\vec{H}_\uparrow - \vec{H}_\downarrow\right) = \left(\alpha_\uparrow + 2\alpha_{ex}\right)\vec{H}_\uparrow = \alpha_{afm}\vec{H}_\uparrow. \tag{2.18}$$

Therefore, according to the model prediction, both the demagnetization and recovery dynamics rates are *exchange-enhanced* in antiferromagnets by $2\alpha_{ex}$ compared to the ferromagnetic case.

Another notable feature of the exchange-enhancement is the dependence on the crystal structure of an antiferromagnet. With the mean-field approximation, we can assume that $\alpha_\uparrow = \alpha_\downarrow$ and $|\vec{m}_\uparrow| = |\vec{m}_\downarrow| = m$. According to Ref. [JA22a], under these assumptions, $\alpha_{ex} = \alpha_\uparrow/(z_{n.n.}m)$, where $z_{n.n.}$ is the number of the nearest neighboring spins. Hence, the exchange-enhanced AF damping parameter can be re-written as following:

$$\alpha_{afm} = \alpha_{fm}\left(1 + \frac{2}{z_{n.n.}m}\right). \tag{2.19}$$

This result tells us that, unlike ferromagnets, depending on $z_{n.n.}$, in other words, depending on the crystal structure of a considering antiferromagnet, the amount of the exchange-enhancement in α_{afm} can significantly vary.

2.2.2 Application of the microscopic three temperature model

As will be presented in Chapter 6, we are going to apply the M3TM to experimental results of AF $GdRh_2Si_2$. In this subsection, by introducing an actual application case, main physical parameters and their role will be explained to show how this model operates. Within this model, the electronic temperature T_e, the lattice temperature T_p, and the magnetization m are described by three coupled differential equations:

$$C_e\frac{dT_e}{dt} = G_{ep}\left(T_p - T_e\right) + \nabla\left(k_e\nabla_z T_e\left(z\right)\right) + S\left(z,t\right) \quad , \tag{2.20}$$

$$C_p\frac{dT_p}{dt} = -G_{ep}\left(T_p - T_e\right) \quad , \tag{2.21}$$

$$\frac{dm}{dt} = Rm\frac{T_p}{T_N}\left(1 - \frac{m}{B_{7/2}(mE_{ex}/k_BT_e)}\right)\left(1 + \frac{2}{z_{n.n.}m}\right) \quad . \tag{2.22}$$

In Eq. (2.20), $C_e = \gamma_0 T_e$ is the electronic heat capacity, where γ_0 is the Sommerfeld coefficient. G_{ep} is the electron-phonon coupling constant. k_e is the electronic thermal conductivity, and $S(z,t)$ models the depth- and time-dependent pump excitation given by a Gaussian distribution of the pump pulse temporal width and its exponential suppression according to the pump pulse penetration depth of 20.6 nm [Win+20]. In Eq. (2.21), C_p is the lattice heat capacity. As we see a predominant reduction of magnetic order on a timescale comparable to lattice heating, and the localized nature of the Gd $4f$ moments, we include the spin heat capacity in the lattice heat capacity (Fig. 6.4-b). The lattice heat capacity is taken from the specific heat of $LuRh_2Si_2$ (a paramagnetic (PM) sister compound of AF $GdRh_2Si_2$ due to the fully-filled $4f$ orbital of the Lu ions) and the spin heat capacity extracted as the difference of the specific heat between AF $GdRh_2Si_2$ and PM $LuRh_2Si_2$ as detailed in subsection 6.2.2 [KK15]. In Eq. (2.22), $R = (8a_{sf}G_{ep}\mu_B k_B T_N^2)/(\mu_{at}E_D^2)$ is a material-specific factor proportional to a_{sf}, the spin-flip scattering probability. T_N is the Néel

temperature. $B_{7/2}(E_{ex}/k_BT_e)$ is the Brillouin function, where E_{ex} is the exchange energy (proportional to the Néel temperature of AF $GdRh_2Si_2$), and k_B is the Boltzmann constant. μ_{at}, E_D are the atomic magnetic moment of Gd $4f$ and the Debye energy, k_BT_D, respectively. The Debye temperature T_D is estimated by fitting the Debye model to the lattice heat capacity. The term $2/(z_{n.n.}m)$ in Equation (2.22) describes the antiferromagnetic angular momentum transfer between different Gd $4f$ sublattices (Eq. 2.19), where $z_{n.n.} = 8$ is the number of AF coupled nearest neighbors. We note here that while the model considers the response of a bulk-coordinated system, the reduced magnetic coordination at the surface will cause slightly larger demagnetization for a given pump excitation compared to a pure bulk system. As will be shown in Chapter 6, the model predicts much larger demagnetization even in the bulk limit. Therefore, we do not consider surface effects in the AF coordination in this study.

Eqs. (2.20) and (2.21) (the standard two-temperature model) describe the energy flow from the electrons, which are heated by the source term S, into the lattice and the heat transport due to diffusion [Lis+04]. Eq. (2.22) is derived from the LLB equation, which is extended to antiferromagnets and combined with the M3TM as explained previously [JA22a]. It describes the magnetization dynamics depending on T_e and T_p. In order to account for the different probe depths of the two probes (trARPES: ∼0.5 nm [Güt+16], trRXD: ∼4.2 nm [Win+22]), simulations are performed as function of depth z, and weighted with the respective probe depths.

The role of each parameter in the M3TM simulation

Eq. (2.22) depends on various physical parameters. In this subsection, we present the role of each parameter in ultrafast temperature and magnetization dynamics simulation within the M3TM.

Electron-phonon coupling constant G_{ep} The electron-phonon coupling constant determines the rate of equilibration process between hot electrons (T_e) and cold lattice (T_l) upon photoexcitation. Larger G_{ep} yields quicker electron-lattice relaxation (Figure 2.5-a). Since spin-flip scattering efficiently occurs at large thermal inequilibrium state at early stage of the dynamics [Koo+10], the longer the inequilibrium state lasts, the more prominent the subpicosecond demagnetization dynamics is (Figure 2.5-b). G_{ep} is determined by fitting to the experimental electronic temperature dynamics

Sommerfeld coefficient γ_0 The Sommerfeld coefficient γ_0 is the slope of linearly increasing electronic heat capacity C_e with respect to temperature T_e. Smaller γ_0 causes larger thermal inequilibrium but with shorter duration of inequilibrium state (Figure 2.5-c). Since the size of the thermal inequilibrium determines the rate of the subpicosecond demagnetization process, smaller γ_0 yields faster subpicosecond demagnetization (Figure 2.5-d). γ_0 is determined by fitting to the experimental electronic temperature dynamics.

Thermal conductivity k_e The thermal conductivity k_e determines how quickly the system cools down upon photoexcitation. Larger k_e yields smaller T_e and T_l globally, shorter duration of inequilibrium state and faster cooling through efficient heat diffusion in the bulk system (Figure. 2.5-e). According to Eq. (3), the recovery dynamics sets in only if the equilibrated temperatures (T_e, T_l) are below the Néel temperature. Since larger k_e yields efficient cooling of the system, the recovery dynamics becomes more prominent for larger k_e (Figure 2.5-f). k_e is determined by fitting to the experimental electronic temperature dynamics.

Material-specific R factor The material-specific R factor determines how efficiently the spin-flip scattering occurs upon photoexcitation since it is proportional to the spin-flip scattering probability a_{sf}. While they all share almost identical temperature dynamics (Figure 2.5-g), the magnetization dynamics with larger R factors exhibit faster and larger demagnetization and recovery dynamics (Figure 2.5-h).

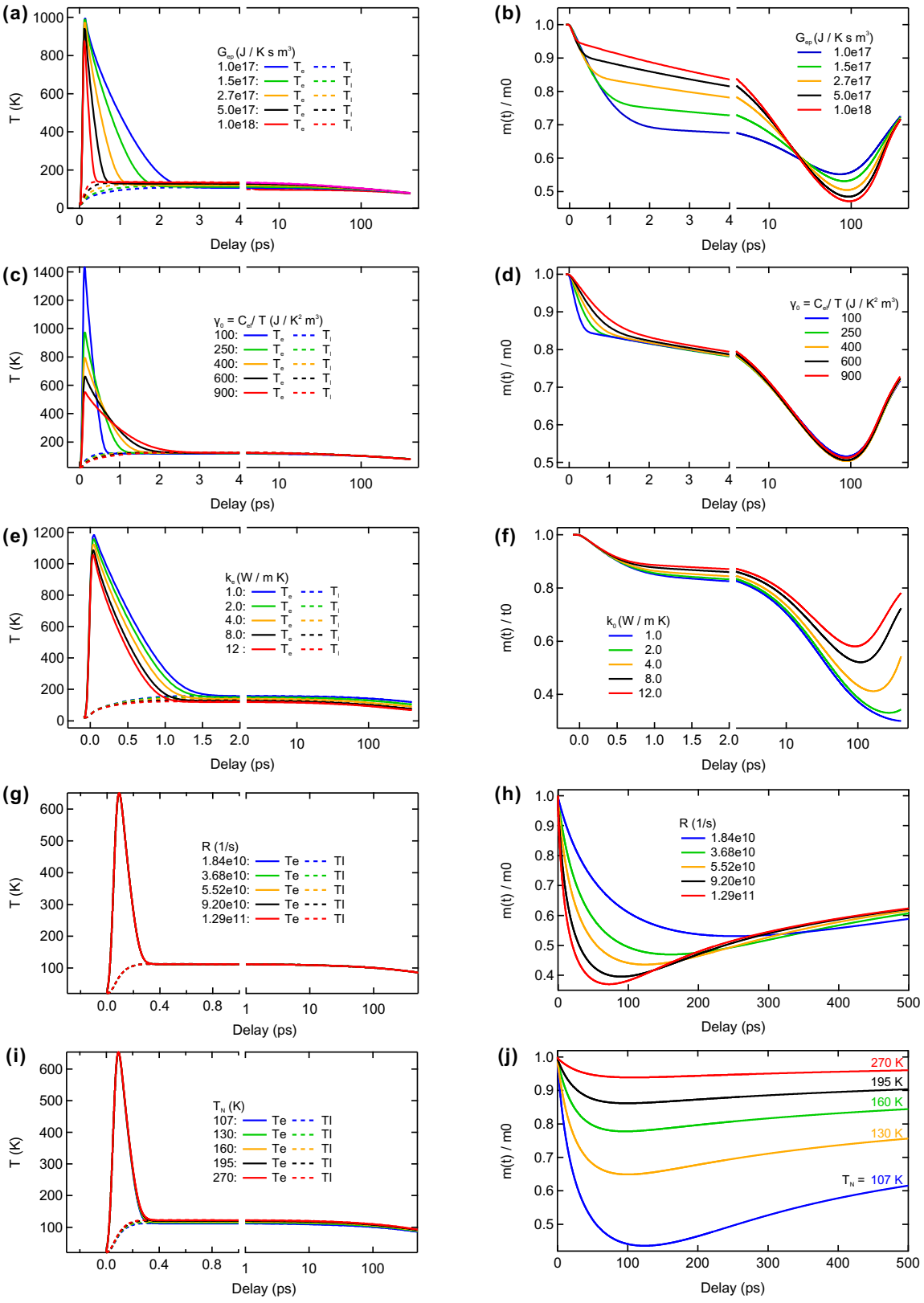

Figure 2.5: Parameter dependence of simulated curves of the M3TM applied in this study (see text). Left (right) column is temperature T (magnetic order m) dynamics. Dynamics at at various values of electron-phonon coupling constant G_{ep} (T: (a), m: (b)), Sommerfeld coefficient γ_0 (T: (c), m: (d)), electron diffusion constant k_e (T: (e), m: (f)), material-specific R factor (T: (g), m: (h)), and Néel temperature T_N (T: (i), m: (j)). Note that the second horizontal axes are log-scaled except (h) and (j).

Néel temperature T_N The Néel temperature T_N determines the threshold temperature when the recovery dynamics sets in; once the equilibrated temperature reaches below T_N, demagnetization stops and recovery starts. The temperature dynamics at various T_N values share almost identical dynamics (Figure 2.5-i). On the other hand, the magnetization dynamics exhibit drastically different demagnetization amplitude (Figure 2.5-j). However, the timescale of the demagnetization and recovery is more or less similar, unlike the material-specific R factor, which drastically changes the timescale as well.

This page is intentionally left blank.

Chapter 3

Two experimental approaches to study $4f$ antiferromagnets

Disclaimer: A part of this chapter was published in "Exchange scaling of ultrafast angular momentum transfer in 4f antiferromagnets" *Nature Materials* **21**, 514–517 (2022)

While the self-cancelling spin arrangement makes antiferromagnets intriguing both in the theoretical and in the practical perspectives, it also poses significant challenges: Accessing the antiferromagnetic order parameter. Accessing the AF order parameter, indeed, demands new experimental approaches that do not rely on mesoscopically imbalanced spin populations or broken time reversal symmetry. In this thesis of studying AF LnT_2Si_2, we achieve this by combining time-resolved resonant elastic x-ray diffraction (trRXD) sensitive to out-of-plane bulk AF order and time- and angle-resolved photoemission spectroscopy (trARPES) sensitive to in-plane surface ferromagnetic (FM) order. In this chapter, we will introduce the working principles and the experimental setups of trRXD and trARPES techniques.

3.1 Time-resolved resonant elastic magnetic x-ray diffraction

Elastic x-ray diffraction experiments are one of the most powerful ways to obtain information on the microscopic structure of matter. In solid state physics, conventional elastic diffraction of photons is a standard method to study the precise spacing and the location of atoms in solids. Resonant elastic magnetic x-ray diffraction is performed at primary photon energies close to an absorption edge, and involves virtual transitions (Figure 3.1) from core levels into unoccupied states close to the Fermi level. These virtual transitions depend strongly on the spin configurations of the resonant scattering centers, strongly enhancing the magnetic scattering cross section by even eight orders of magnitude. Moreover, since the virtual excitations in RXD are related to specific core-level excitations, the excitation energy of which changes from element to element, the method is element specific, allowing us to probe magnetic structure associated with individual specific elements. As the penetration depth of the x-ray light is a few nanometer (see Table 3.1), RXD is bulk sensitive. Hence, it is an element-resolved, bulk-sensitive technique, sensitive to the long-range spin ordering encompassing several unit lattices of LnT_2Si_2. The purpose of RXD experiments in this thesis is to probe the long-range antiferromagnetic order by elastic scattering at an angle that fulfills Bragg's law for this order. In this thesis, unless specified, we probe magnetic order with a modulation vector defined by Miller indices [001] where lattice contribution is prohibited, and only magnetic contribution, more precisely, antiferromagnetic order repeating every unit lattice, is prominent.

The cross section for magnetic scattering of x-rays is very small compared to charge scattering [Blu85]. Therefore, specific photon energies have to be used that correspond to atomic resonances of a specific ion. The scattering cross section can then be resonantly enhanced by several orders of magnitude, to the point that the signal is effectively dominated by scattering from the resonant

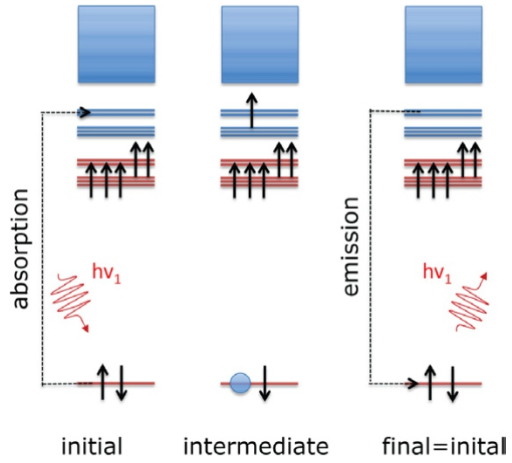

Figure 3.1: Schematics of the virtual transition in the elastic resonant scattering process. An incident soft x-ray light excites an occupied core electron, Ln $3d$ (left). The excited electron promotes to the unoccupied state, Ln $4f$ (middle). The excited electron returns to the initial Ln $3d$ state emitting a soft x-ray light of the same energy as the incident light (right). Reproduced with permission from IOP Publishing [Fin+13]. All rights reserved.

ions. In the present case, we use energies that correspond to the $M_{4,5}$ edges of lanthanides, where the scattering length can reach $200r_0$ [Han+88; Ott+06] (r_0 is the classical electron radius). The dominant resonant process is assumed to be an E1 electric dipole transition ($3d \rightarrow 4f$), meaning that the resonant magnetic signal we collect is primarily sensitive to the $4f$ states.

3.1.1 Extraction of changes in local moment

For an electric dipole-dipole transitions (E1-E1 event), the intensity of a magnetic reflection I probed by RXD is proportional to the squared structure factor F, written as [Han+88; HM96]

$$F(\vec{Q}) = (\hat{\epsilon}' \times \hat{\epsilon}) \cdot \sum_i f_i e^{i\vec{Q}\cdot\vec{r}_i} \propto (\hat{\epsilon}' \times \hat{\epsilon}) \cdot \vec{m} \tag{3.1}$$

Here the $(\hat{\epsilon}' \times \hat{\epsilon})$ term is the cross product between the incoming and scattered polarization vectors, $\vec{Q}$ is the scattering vector, and the sum is over all resonant ions in the magnetic unit cell (other ions are neglected, as their scattering contribution is non-resonant i.e. negligibly small), each with position r_i. The resonant scattering factor f_i is proportional to the local moment $\vec{m}$.

In the second step of Eq. (3.1), we describe the present experiment by evaluating the sum for the magnetic [0 0 L] reflection (L=1, unless specified), summing only over the resonant Ln ions. The sum in Eq. (3.1) is then proportional to $\vec{m}$, such that the proportionality encodes the spectroscopic features of the resonance (see subsection 3.1.3), and the dot product represents the anisotropy of the scatterers (i.e., the magnetic moments) with respect to the scattering plane. Furthermore, this means that the respective intensity can be expressed as $I(x) \propto |\vec{F}|^2 \propto m^2(x)$, with x representing pump-probe time delay (t) or temperature (T).

This illustrates that for the case of $Ln\,T_2Si_2$ materials, relative changes in the ordered Ln $4f$ moment can be directly extracted from intensity. Exceptions to this are coherent rotations of all spins, resulting from changes to the anisotropy of the $4f$ system with T or t. This manifests through the dot product in Eq. (3.1).

3.1.2 Domain effects

The presence of antiferromagnetic domains can affect the RXD signal if more than one domain is probed by the x-ray spot. The magnetic modulation in these domains is the same, though separated

by a phase, complicating the analysis using Eq. (3.1). Here we consider the effect that could have on our experiments.

All dynamic experiments in this thesis were conducted with incoming σ polarized (linear) x-rays, so only the $\sigma \to \pi'$ polarization channel is considered because $\sigma \to \sigma'$ is zero by symmetry [HM96]. This simplifies Eq. (3.1), and what remains is to consider the orientations of the moments in the unit cell. Two limiting cases exist:

Moments are alternatingly aligned along the [001] axis : This occurs for most of the studied materials (Ln=Pr, Nd, Tb, Dy, and Ho). In this case Eq. (3.1) yields $I \propto m^2$, meaning that the intensity is insensitive to antiferromagnetic domain effects that cause $m \to -m$. Furthermore, 90° twinning caused by the tetragonal symmetry of the crystals does not affect this signal either.

Alternating moments lie in the planes normal to [001] This occurs for Ln= Gd and Sm. Here Eq. (3.1) yields $I \propto m^2 \cos^2 \Psi$, in which Ψ represents azimuthal rotation of the sample around [001]. The signal remains insensitive to domain effects of the form $m \to -m$. Unlike the previous case, 90° twinning can affect the validity of using Eq. (3.1), because domains of $\cos^2 \Psi$ and $\cos^2(\Psi + 90°)$ can be simultaneously probed by our x-ray beam. This effect can influence our results if the temperature- or delay-dependent behavior of the system includes changes in the local magnetic anisotropy. This concern is relevant only to Ln = Gd, and Ref. [Win+20] provides a detailed account of how this was overcome.

We therefore conclude that our experiments are insensitive to domain effects, except for the case of Ln = Gd, which was carefully accounted for by measuring diffraction intensity at various azimuthal orientations to extract the correct AF order parameter.

3.1.3 Spectroscopic features of the resonance

In this subsection we consider how the behavior of the [0 0 L] (L=1 unless specified) reflection varies through the M edges used in our experiments. These resonances are the main difference between the $Ln T_2Si_2$. Data were collected at beamlines with high energy resolution (either using the ReSoXS end station [Sta+08] at the SIM beamline [Fle+10] of the Swiss Light Source (SLS), or at the PM3 beamline in HZB [KEF15]), so that a reliable description of the resonant behavior (e.g. resonant amplification, penetration depth) of the [0 0 l] reflection is assumed in the data presented below. In contrast, the time-resolved experiments were conducted at the FemtoSpeX facility at beamline UE56/1-ZPM [Hol+14], in which a zone plate monochromator (ZPM) is used to maximize photon flux. A drawback of the ZPM is its low energy resolution, such that a reliable description of the resonance is not possible.

For high resolution measurements, features of the atomic resonance are extracted by conducting reciprocal space scans through the [0 0 L] (L=1 except $GdCo_2Si_2$) reflection (θ-2θ scans) at several energies around the absorption edge. This is presented in the left column of Fig. 3.2 for $Ln Rh_2Si_2$. The figure's rows each present data from a different Ln element. We focus on two quantities:

Integrated intensity Integrated intensities are presented in the middle column as function of energy (solid icons). Equivalent energy scans were taken using the ZPM in the time-resolved experiment (open circles). To estimate the spectral resolution at each resonance, the high-resolution data were convolved with a Gaussian resolution function. This is presented as solid lines, and Gaussian width at half maximum is indicated in units of eV for each element. Values are listed in Table 3.1.

Diffraction peak width (inverted) Diffraction peak widths are presented in the right column as a function of energy. It is a measure of the effective magnetic volume contributing to the diffraction signal. While off resonance the width is dominated by the magnetic correlation length,

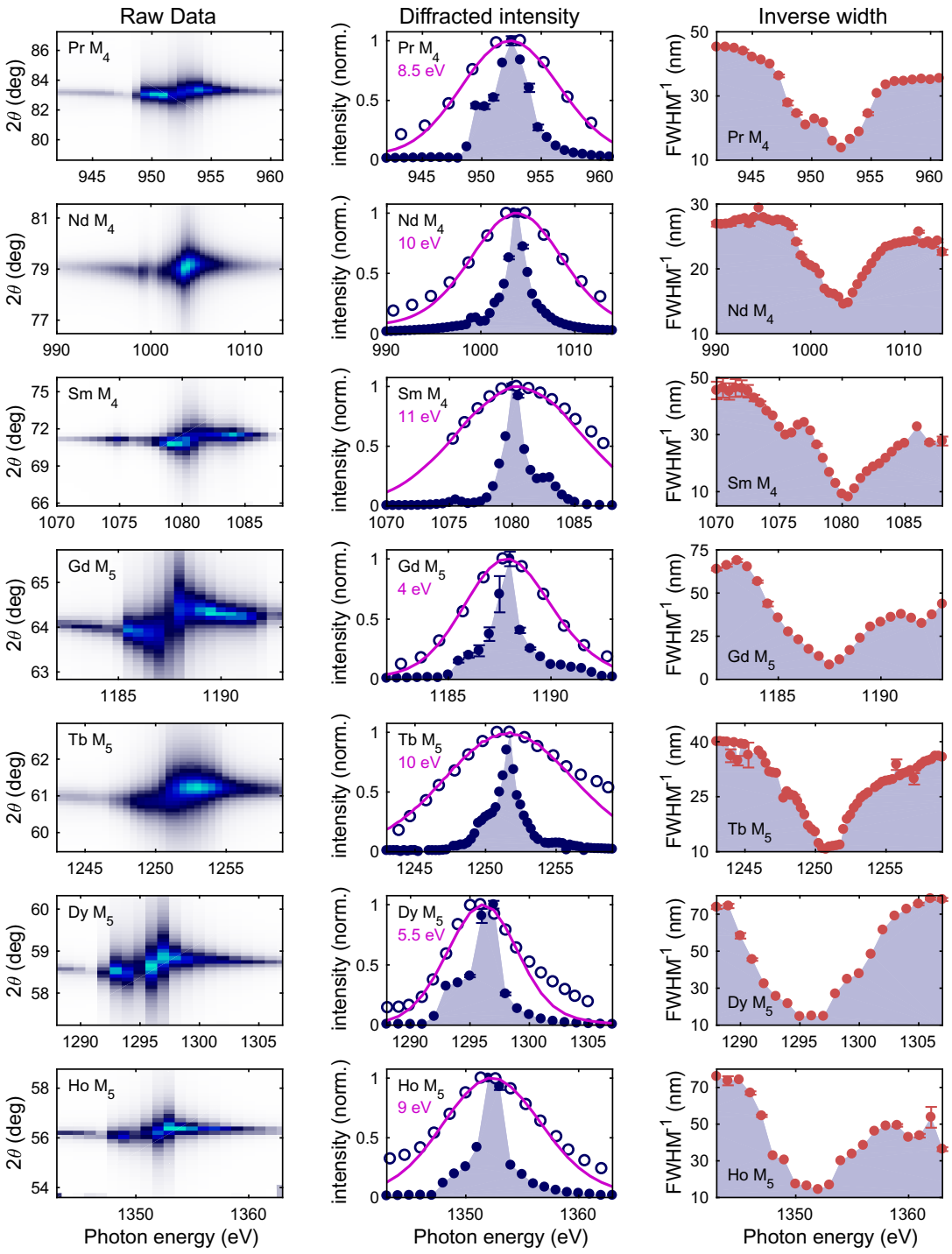

Figure 3.2: The left column presents θ-2θ scans (equivalent to reciprocal space cuts along [001]) at several energies across the resonance. These scans were conducted at beamlines with high energy resolution. The color scale represents scattered intensity (from high to low: light blue $\rightarrow$ dark blue $\rightarrow$ white background). The middle column presents the integrated intensity extracted from such scans (solid circles), alongside the energy scans of (001) taken at FemtoSpeX (open circles). To determine the ZPM energy resolution, a Gaussian of the indicated width in energy (full width at half maximum) is convolved with the high energy resolution data (solid pink lines). The right column presents the inverse width of the Bragg reflection, providing a measure of the probe depth as function of energy. Reproduced with permission from Springer Nature [Win+22].

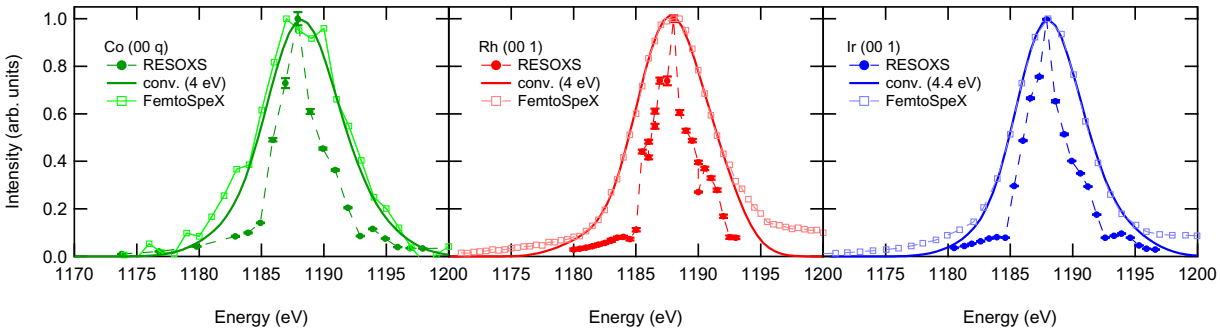

Figure 3.3: Photon energy dependence of the magnetic diffraction intensities of Gd T_2Si$_2$ acquired at high energy resolution beamline (solid symbols) and FemtoSpeX beamline (open symbols). To determine the ZPM energy resolution, a Gaussian of the indicated width in energy (full width at half maximum) is convolved with the high energy resolution data (solid lines).

at resonance it becomes limited by the finite penetration depth of the x-rays. We define the effective probe depth as half of this value as the scattered light is attenuated again when leaving the solid.

3.1.4 Description of the synchrotron setups

Most of equilibrium resonant soft x-ray diffraction (RXD) experiments were performed at the ReSoXS end station of the SIM beamline in Swiss Light Source, Villigen, Switzerland [Fle+10; Sta+08], which provides high photon energy resolution, precise polarization of incident light, and 6-axis manipulation (x, y, z translational movements, and polar, azimuthal, tilt rotations) of a sample. A part of the equilibrium measurements were performed at the PM3 beamline at the Helmholtz-Zentrum Berlin, Germany. From the equilibrium measurements, we characterized the $Ln\,T_2$Si$_2$ samples by observing photon energy dependence of the magnetic diffraction peak and spin structure evolution upon equilibrium heating. Ref. [Fin+13] explains the RXRD technique in detail.

Time-resolved resonant soft x-ray diffraction (trRXD) experiments were performed at the FemtoSpeX beamline of BESSY II in Berlin, Germany, which uses femtosecond slicing to provide ultrashort soft x-ray pulses [Hol+14], which will be introduced in subsection 3.1.5. We used 50 fs-long laser pulses centered at 1.55 eV, at repetition rate of 3 kHz to excite the sample, and measured the transient diffraction intensity with 100 fs-long, sliced soft x-ray pulses of photon energy at Ln ion's respective dominant M absorption edge (M_4 for Pr, Nd and Sm ($3d_{3/2} \rightarrow 4f$); and M_5 for Gd, Tb, Dy and Ho ($3d_{5/2} \rightarrow 4f$) at a repetition rate of 6 kHz with an avalanche photodiode (APD) covered with an aluminum foil to prevent a pump pulse counting (Fig. 3.4). We measured the resonantly enhanced magnetic diffraction intensity at constant momentum transfer Q=[0 0 L], sensitive to long-range Ln $4f$ AF ordering repeating along the c axis. All dynamic experiments were conducted at 20 K unless specified. Samples were single crystals [Kli+20]. Due to the layered crystal structure, the sample surface is precisely perpendicular to the tetragonal [001] axis. The crystals used were approximately 1-2 mm^3 in size, with faces much larger than the pump and probe beam spots.

3.1.5 Femtoslicing

Femtosecond-short soft x-ray pulses are essential component to achieve time-resolved magnetic soft x-ray diffraction in 150-fs resolution. FemtoSpeX beamline at BESSY II, Berlin in Germany achieved this with a technique called 'femtoslicing'. In this subsection the working principles of femtoslicing will be introduced.

Electron bunch in a storage ring of a synchrotron can gain/lose energy from interference of

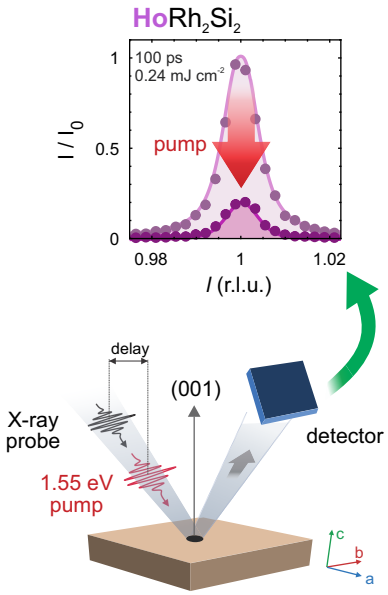

Figure 3.4: Sketch of the time-resolved resonant soft x-ray diffraction (trRXD) experimental scheme, with the scattering vector parallel to the sample's [001] crystal direction and the two pulses arriving collinearly. The graph on top shows reciprocal space scans of the (001) magnetic reflection of $HoRh_2Si_2$ before excitation (bright) and 100 ps after excitation (dark) using an absorbed fluence of 0.24 mJ/cm^2. r.l.u. are reciprocal lattice units. Reproduced with permission from Springer Nature [Win+22].

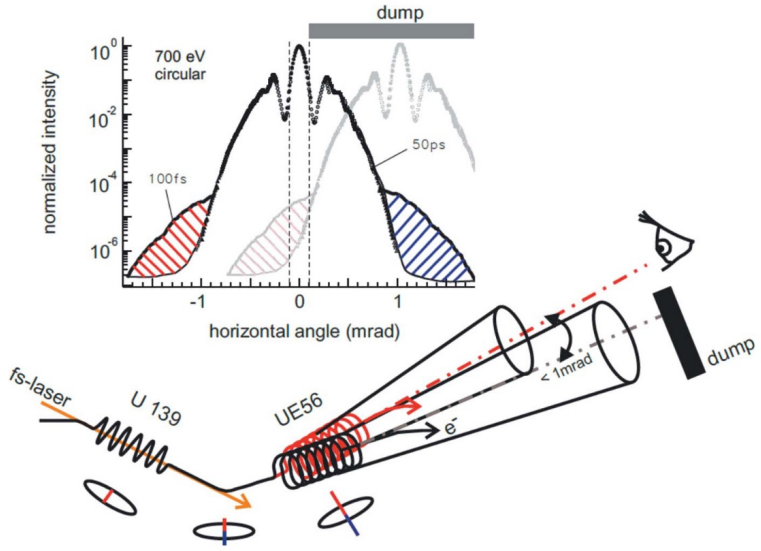

Figure 3.5: Schematics describing modulation of ps-electron bunch with fs-pulsed-laser for femtoslicing. U139: a planar wiggler of 10 periods, UE56: an elliptical undulator of 30 periods [Hol+14]. Users can switch between soft x-rays of ∼100 fs and ∼50 ps on demand with dump. Reproduced with permission of the International Union of Crystallography [Hol+14].

the electric fields of laser pulses $\vec{E}_L$ and of far-field radiation of undulator magnets $\vec{E}_R$. This interaction between the electron bunch and laser pulses is called energy modulation. In 1996, Zholents & Zolotorev showed that the energy modulation can be applied to slice x-ray pulses in femtosecond timescale (femtoslicing) [ZZ96]. Since the total field energy E is determined by the square of the superimposed electric field $\left|\vec{E}_L + \vec{E}_R\right|^2$, we can express E as follows [ZZ96]:

$$E = E_L + E_R + 2\sqrt{E_L E_R \frac{\Delta\omega_L}{\Delta\omega_R}} \cos\phi, \tag{3.2}$$

where E_L, E_R are energy of the laser pulses and spontaneous radiation of electrons in the undulator, respectively. $\Delta\omega_L$, $\Delta\omega_R$ are the bandwidth of the laser pulses and undulator radiation, respectively, assuming $\Delta\omega_L > \Delta\omega_R$. The third term on the right hand side of Eq. (3.2) is the energy gain/loss of the electron bunch from the energy modulation, and phase difference ϕ between the laser pulses and electron wiggling trajectory in the undulator determines the sign, i.e. gain or loss. This energy gain/loss causes the sliced bunch to have slightly different orbit when it propagates in an undulator allowing spatial separation of the sliced bunch from the core bunch.

In its implementation at FemtoSpeX, it employs a fs-pulsed Ti:Sa laser to generate an energy modulation of a single electron bunch in the storage ring, as the electrons and the laser co-propagate in a wiggler. The bunch, then crosses an undulator (UE56, Apple II type): the modulated "slice" emits soft x-rays in an ultrashort pulse (100 fs) at a slightly different angle (-1 mrad) from the long pulse (50 ps) coming from the main part of the bunch (Figure 3.5) [Hol+14]. Using small electron orbit corrections, it is possible to shine short or long pulses through the beamline to the experimental endstation. Synchronization is regulated by the master clock of the accelerator so that the fs laser pulses hit the maximum of the electron bunch [Hol+14].

However, the rest part of the energy-modulated electron bunch still remains in the storage ring even after the spatial separation of the sliced bunch and performs betatron [HPT55] and synchrotron oscillations around the core bunch. The betatron oscillation emits a 'halo' beam, and some of the halo beam provides unwanted ps-long background worsening signal-to-background ratio even to 1:1 at 6 kHz of the repetition rate [Sch+16]. To eliminate this halo background, FemtoSpeX beamline introduced a special pulse providing plan, 'sequence mode'. Instead of providing one electron bunch, the storage ring provides three (since 2020, seven) electron bunches temporally separated by 12 ns for the femtoslicing, which virtually decreases the slicing repetition rate to 6/(number of bunches) kHz and, in consequence, improves the signal-to-background ratio significantly [Hol+14; Sch+16].

Since the "sliced" x-ray pulses are derived from only a part of the electron bunch modulated by a pulsed laser, there is a significant amount of photon flux reduction. Furthermore, for frequency synchronization of the Ti:Sa fs-laser (6 kHz) and the electron bunch revolution of the storage ring (1.25 MHz), the available photon flux for femtoslicing further decreases. This, in the end, results 8 orders of magnitude smaller photon flux in the femtoslicing mode [Hol+14]. Due to this large photon flux reduction, typical operation requires identifying and optimizing the magnetic x-ray diffraction condition first at ∼50-ps-mode, then switching to ∼100-fs mode for femtosecond dynamics measurement.

As a byproduct, femtosecond far-infrared THz radiation is generated from the energy modulation of electrons by fs pulsed laser [Hol+06]. When operating the beamline in ∼100-fs mode, users can utilize the THz radiation as a live diagnostic to check and optimize the overlap quality of the laser and electron bunch. For this scope, at FemtoSpeX, a dedicated THz beamline has been set-up, equipped with active laser beam stabilization [Hol+14].

Two coupled Ti:Sa amplifiers driven by the same oscillator run at 6 and 3 kHz for the femtoslicing and the optical pump, respectively (Fig. 3.6) [Hol+14]. Since the amplifier and the oscillator are 40 m apart, solid beam stabilization in-vacuum under controlled temperature environment is introduced to prevent timing jitter or drifts [Hol+14]. Users can conveniently check the beam stabilization status at the control room from a dedicated oscilloscope screen captured by a camera

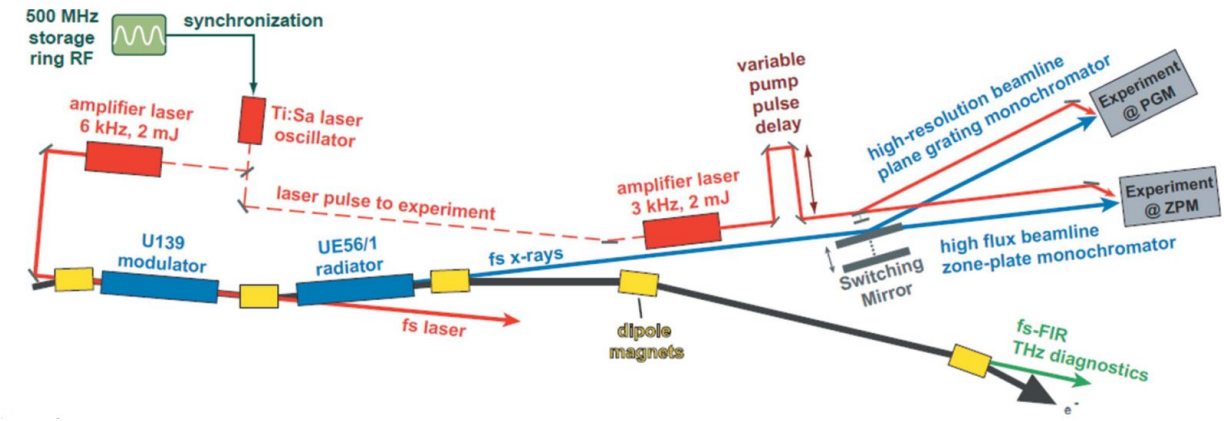

Figure 3.6: Schematic layout of the full optical pump-soft-x-ray probe set-up at the FemtoSpeX beamline. Reproduced with permission of the International Union of Crystallography [Hol+14].

LnT_2Si_2	ZPM resolution (eV)	Probe depth (nm)
$PrRh_2Si_2$	8.5	6.9
$NdRh_2Si_2$	10.0	7.3
$SmRh_2Si_2$	11	4.1
$GdCo_2Si_2$	4.0	4.0
$GdRh_2Si_2$	4.0	4.2
$GdIr_2Si_2$	4.4	4.1
$TbRh_2Si_2$	10.0	5.3
$DyRh_2Si_2$	5.5	7.3
$HoRh_2Si_2$	9.0	7.2

Table 3.1: Zone-plate monochromator energy resolution and penetration depth for the probe beams in each of the LnT_2Si_2 samples. Reproduced with permission from Springer Nature [Win+22].

installed in the laser hutch. With 50-fs long pump pulses and 100-fs long "sliced" soft x-ray pulses, 120-150 fs temporal resolution is achieved [Hol+14].

As discussed earlier, femtoslicing brings significant photon flux reduction. Therefore, in order to achieve the highest possible transmission of soft x-ray light (up to 21% [Brz+13]) from a monochromator, single-element reflection zone plates (RZPs) are employed. However, the focal length of a reflection zone plate depends very much on the wavelength of the incident light. In other words, each RZP has a very narrow working energy range. To encompass large working energy range (410 - 1333 eV) at the FemtoSpeX beamline, an array of nine different RZPs is employed: Two are for K-edges of oxygen and nitrogen, five for $L_{2,3}$-edges of $3d$ transition metals, and two for $M_{4,5}$-edges of $4f$ lanthanides [Brz+13]. This array of RZPs is called the zone plate monochromator (ZPM). Users can choose a corresponding RZP by moving the ZPM perpendicular to the beam axis. ZPM allowed us to work at various Ln $M_{4,5}$ absorption edges (1000 - 1300 eV) for studying LnT_2Si_2 compounds. The energy resolution of the zone plate monochromator (ZPM) at BESSY II is determined by comparing the energy-dependent behavior of the magnetic diffraction intensity acquired at ReSoXS endstation which provides more precise photon energy resolution with the energy dependent behavior acquired at BESSY II (see Fig. 3.2, vertical axes in the center column and Fig. 3.3).

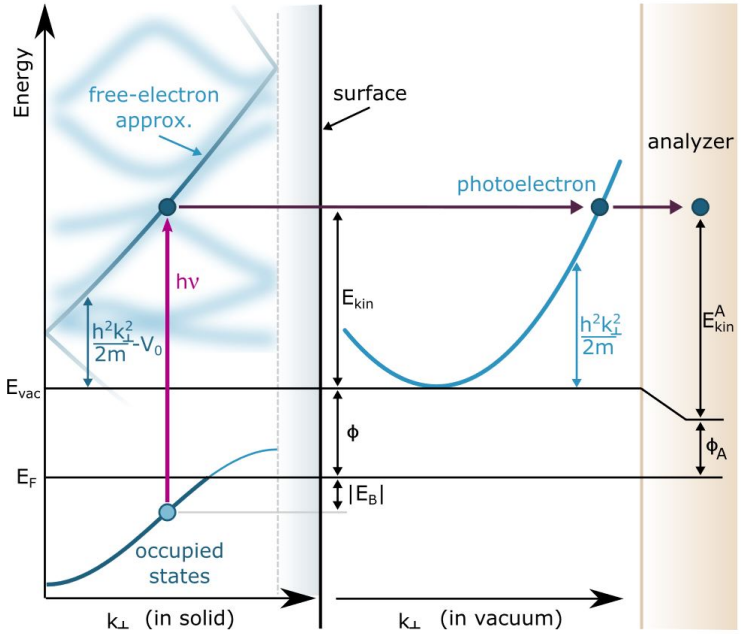

Figure 3.7: Kinematics of photoelectron effect. Φ_A is the work function of the electron analyzer, and E^A_{kin} is the kinetic energy of a photoelectron with respect to Φ_A. In this thesis, the sample and analyzer are grounded to the lab earth ($\Phi = \Phi_A$, $E_{kin} = E^A_{kin}$). Reprinted figure with permission from [SHS21]. Copyright 2021 by the American Physical Society.

3.2 Time- and angle-resolved photoemission spectroscopy

Time- and angle-resolved photoemission spectroscopy (trARPES) is an essential experimental technique to study temporal evolution of the electronic structure of solids. Unlike the previously discussed RXD, which is a photon-in, photon-out technique, ARPES is a photon-in, electron-out technique. The kinetic energy and angular distribution of emitted photoelectrons provide a powerful insight on the electronic band structure of solids (Figure 3.7). As will be explained in subsection 3.2.1, due to surface-sensitive character of the ARPES technique, we can study properties of itinerant conduction electrons in $4f$ antiferromagnets such as electronic temperature and exchange splitting of a surface state as shown in Chapter 6. Extending in the time domain with a pump-probe approach employing a femtosecond-short pulsed laser, we can investigate photo-induced ultrafast phase transition in the perspective of the conduction electrons. TrARPES nicely complements the information of trRXD: As the former is surface sensitive and probes the electronic structure, while the latter is bulk sensitive and probes the magnetic order parameter. In this section, we are going to review the working principle of ARPES and the optical setup for time-resolved measurement. Readers interested in detailed discussion of ARPES technique are recommended to read [DHS03; SHS21].

3.2.1 Working principle of ARPES

When light shines on a material, it interacts mostly with electrons. If the energy of the light $h\nu$ (where h, ν are the Planck's constant and frequency of the light, respectively) is larger than the sum of the work function of the material Φ and the binding energy of the electron E_B , a photoelectron is emitted with following kinetic energy:

$$E_{kin} = h\nu - \Phi - E_B \tag{3.3}$$

Photoemission spectroscopy refers to various techniques based on this phenomenon, the photoelectric effect [Ein05; Her87]. Due to the lack of translational symmetry along the surface normal,

perpendicular component of the photoelectron momentum $\vec{p}_\perp$ is not conserved. Instead, applying the conservation laws of energy and momentum, we can deduce the crystal momentum component parallel to the surface $\vec{p}_\parallel$:

$$p_\parallel = \hbar k_\parallel = \sqrt{2mE_{kin}} \sin\theta \tag{3.4}$$

where θ is the emission angle of photoelectrons. Eqs. (3.3) and (3.4) tell us that by collecting the kinetic energy and emission angle of photoelectrons, we can study the binding energy E_B and crystal momentum $\hbar\vec{k}$ of materials with periodic crystal structure, e.g. solids (Fig. 3.7). In this study, we used a hemispherical electron analyzer to record E_{kin} and θ. Photoelectrons passes a set of electrostatic lenses inside the hemispherical analyzer, and depending on E_{kin}, the photoelectrons are deflected on orbits of different radius and thus spatially separated. Then, the photoelectrons are detected by a 2D multichannel plate (MCP) detector. The MCP detector detects the kinetic energy E_{kin} and emission angle θ of photoelectrons in parallel. Our hemispherical electron analyzer (SPECS Phoibos 150) offers a momentum resolution of 0.04 $\mathring{A}^{-1}$ ($\sim 1°$) [Mak+20].

There are two ways to describe the photoelectric effect: (i) one-step model [Mah70] and (ii) three-step model [BS64]. The one-step model treats photon absorption, electron excitation, and electron detection as a single coherent process whereas the three-step model treats them separately [SHS21]. While, in pedagogical perspective, the three-step model is still helpful for intuitive understanding of the photoelectric effect, the one-step model is more accurate for explaining spectral intensities and matrix element effects. In this thesis we follow the one-step model description.

Using Fermi's golden rule, we can describe (the rate of) the probability of the photoelectric effect of an N-electron system as following:

$$w_{fi} = \frac{2\pi}{\hbar} \left| \left\langle \Psi_f^N \right| \hat{\mathcal{H}}_{int} \left| \Psi_i^N \right\rangle \right|^2 \delta\left(E_f^N - E_i^N - h\nu\right), \tag{3.5}$$

where $\left|\Psi_i^N\right\rangle$, $\left|\Psi_f^N\right\rangle$ are the initial and final state vectors with energies of E_i^N, E_f^N, respectively. $\hat{\mathcal{H}}_{int}$ is a perturbative Hamiltonian that can be simplified by choosing the Coulomb gauge ($\nabla \cdot A = 0$):

$$H_{int} = \frac{1}{2m}\left(\vec{p} + \frac{e}{c}\vec{A}\right)^2 - e\Phi - \frac{\vec{p}^2}{2m} \approx \frac{e}{2mc}\left(\vec{A}\cdot\vec{p} + \vec{p}\cdot\vec{A}\right) \approx \frac{e}{mc}\left(\vec{A}\cdot\vec{p}\right), \tag{3.6}$$

where the second-order processes are disregarded in the first-order approximation. Considering that the initial state consists of an electron in a N-electron system and that the final state consists of a photoelectron freely propagating in vacuum with $(N-1)$-electron system, under the sudden approximation where there is no interaction between a photoelectron and the rest of the system, we can describe the initial and final states as follows:

$$\left|\Psi_f^N\right\rangle = A\left|\phi_f^{\vec{k}}\right\rangle \otimes \left|\Psi_m^{N-1}\right\rangle, \tag{3.7}$$

$$\left|\Psi_i^N\right\rangle = A\left|\phi_i^{\vec{k}}\right\rangle \otimes \left|\Psi_i^{N-1}\right\rangle. \tag{3.8}$$

With these in mind, Eq. (3.5) can be rewritten as follows:

$$w_{fi} = \frac{2\pi}{\hbar}\frac{e}{mc}\left|\left\langle\phi_f^{\vec{k}}\right|\vec{A}\cdot\vec{p}\left|\phi_i^{\vec{k}}\right\rangle\left\langle\Psi_m^{N-1}\middle|\Psi_i^{N-1}\right\rangle\right|^2 \delta\left(\hbar\omega - h\nu\right), \tag{3.9}$$

where $E_f^N - E_i^N = \hbar\omega$. We name the interaction process between $\hat{\mathcal{H}}_{int}$ and the initial and final photoelectron states as photoemission matrix element $M_{f,i}^{\vec{k}} = \left\langle\phi_f^{\vec{k}}\right|\vec{A}\cdot\vec{p}\left|\phi_i^{\vec{k}}\right\rangle$. The rest of the terms describing the remaining electrons with a "photo-hole" can be described with the Fermi-Dirac distribution function $f(\omega)$ multiplied by the one-electron removal spectral function $A(\vec{k},\omega)$. Then the ARPES intensity can be written as follows:

$$I(\vec{k},\omega) \propto \left|M_{f,i}^{\vec{k}}\right|^2 f(\omega) A(\vec{k},\omega) \tag{3.10}$$

Note that for trARPES intensity, the electronic distribution may not follow the Fermi-Dirac distribution $f(\omega)$ at short pump-probe delays, especially when the electronic system is out of equilibrium. It is thus very important to consider the thermalization state of the electronic system when determining the transient electronic temperature from trARPES intensity.

3.2.2 Optical setup for time-resolved measurement

The optical setup we used for trARPES measurement is explained in [Pup+15; Mak+20] in detail. Employing an optical parametric chirped pulse amplifier (OPCPA) based on a fs Yb:fiber laser system, fs light pulses centered at 800 nm (1.55 eV) are generated at a repetition rate of 500 kHz at an average power of 19.7 W (30 μJ pulse energy) [Pup+15; Mak+20]. A part of the beam is splitted by a beam splitter when it exits the OPCPA, and serves as optical pump. The rest of the beam is frequency-doubled (3.1 eV) in a beta barium borate (BBO) crystal via sum frequency generation. The frequency-doubled light is focused onto a high-pressure argon gas jet for phase matching for higher-order harmonic generation at high repetition rates (500 kHz) [Rot+14; Hey+12]. Only the 7th-order light (21.7 eV) is filtered through a combination of a multi-layer XUV mirror and free-standing metal-foil filters. The 21.7 eV pulses serve as probe pulses and are transmitted to the experimental ARPES vacuum chamber ($\sim 10^{-11}$ mbar) where the sample is mounted, and cooled by a flow-type cryostat. The sample was cooled at 20 K for trARPES measurement, unless specified.

Since electrons interact with their surroundings (electrons themselves, phonons etc.), the mean free path before scattering is very limited. Since photoelectrons lose energy and emission angle information after the scattering, this seriously limits the electron escape depth in the samples. For extreme ultraviolet (XUV) light of 21.7 eV, the electron escape depth in LnT_2Si_2 is a few Å[Güt+16], less than the c lattice constant of LnT_2Si_2 compounds ($\sim$10 Å). This tells us that our trARPES measurement is very surface-sensitive. Because trARPES is a surface-sensitive technique, any contaminants on top of the surface of the sample should be eliminated so that we probe only the sample contribution. In order to achieve surface-clean sample, we exfoliated the sample by cleaving it in in-situ environment.

Then, the pump and probe pulses are spatially and temporally overlapped onto the sample in a near-collinear geometry. From optical path difference produced by a delay stage, we can control the temporal delay between the pump and probe pulses. Photoelectrons emitted from the sample are detected with a hemispherical electron analyzer (SPECS Phoibos 150). Due to the tens of fs high temporal resolution, the energy resolution of our trARPES setup is limited to $\sim$150 meV [Mak+20].

This page is intentionally left blank.

Chapter 4

Exchange scaling of ultrafast angular momentum transfer rate in $4f$ antiferromagnets

Disclaimer: This chapter was published in "Exchange scaling of ultrafast angular momentum transfer in 4f antiferromagnets" *Nature Materials* **21**, 514–517 (2022)

Ultrafast manipulation of magnetism bears great potential for future information technologies. While demagnetization in ferromagnets is governed by the dissipation of angular momentum [Dor+19; Boe+10; Esc+13], materials with multiple spin sublattices, for example antiferromagnets, can allow direct angular momentum transfer between opposing spins, promising faster functionality. In lanthanides, $4f$ magnetic exchange is mediated indirectly through the conduction electrons [JM91] (the RKKY exchange interaction), and the effect of such conditions on direct spin transfer processes is largely unexplored. Here, we facilitate a direct comparison of $4f$ dynamics under comparable conditions by studying ultrafast magnetization dynamics in a series of lanthanide intermetallic antiferromagnets with nearly identical crystal and magnetic structure all across the lanthanide series. This approach allows us to single out the influence of $4f$ occupation. Employing time-resolved resonant magnetic soft x-ray diffraction, we investigate ultrafast magnetization dynamics in $4f$ antiferromagnets $Ln\mathrm{Rh_2Si_2}$ and systematically vary the $4f$ occupation, thereby altering the magnitude of the RKKY coupling energy. While demagnetization timescales are found to differ by nearly two orders of magnitude between materials, the corresponding angular momentum transfer rates clearly exhibit a scaling relation known as de Gennes scaling. Our ab initio calculations identify this as transfer between antiparallel moments and show that it scales with the magnitude of the RKKY coupling between them. Our approach provides a microscopic picture of such AF angular momentum transfer, yielding insight substantially beyond phenomenological models [Koo+10; AC11; Eri+17], which often do not consider this transfer channel. Given the high sensitivity of RKKY to the conduction electrons, our results offer a useful approach for fine tuning the speed of magnetic devices.

4.1 Experimental results

We study the long-range AF order of Ln $4f$ moments in $Ln\mathrm{Rh_2Si_2}$ (Ln = Pr - Ho) using resonant magnetic soft x-ray diffraction. The validity of the comparative analysis of the $Ln\mathrm{Rh_2Si_2}$ family is extensively discussed in subsection 2.1.1. Exclusive sensitivity to the $4f$ moments is achieved by tuning the incoming photon energies to the Ln ions' $M_{4,5}$ resonances ($3d \rightarrow 4f$ excitations). The AF-ordered moment m is extracted from the intensity of the magnetic Bragg reflection (normalized to its saturated value m_0 at the base temperature 20 K). To achieve the high temporal resolution needed for this experiment, we used ultrashort x-ray pulses produced by the femtoslicing facility

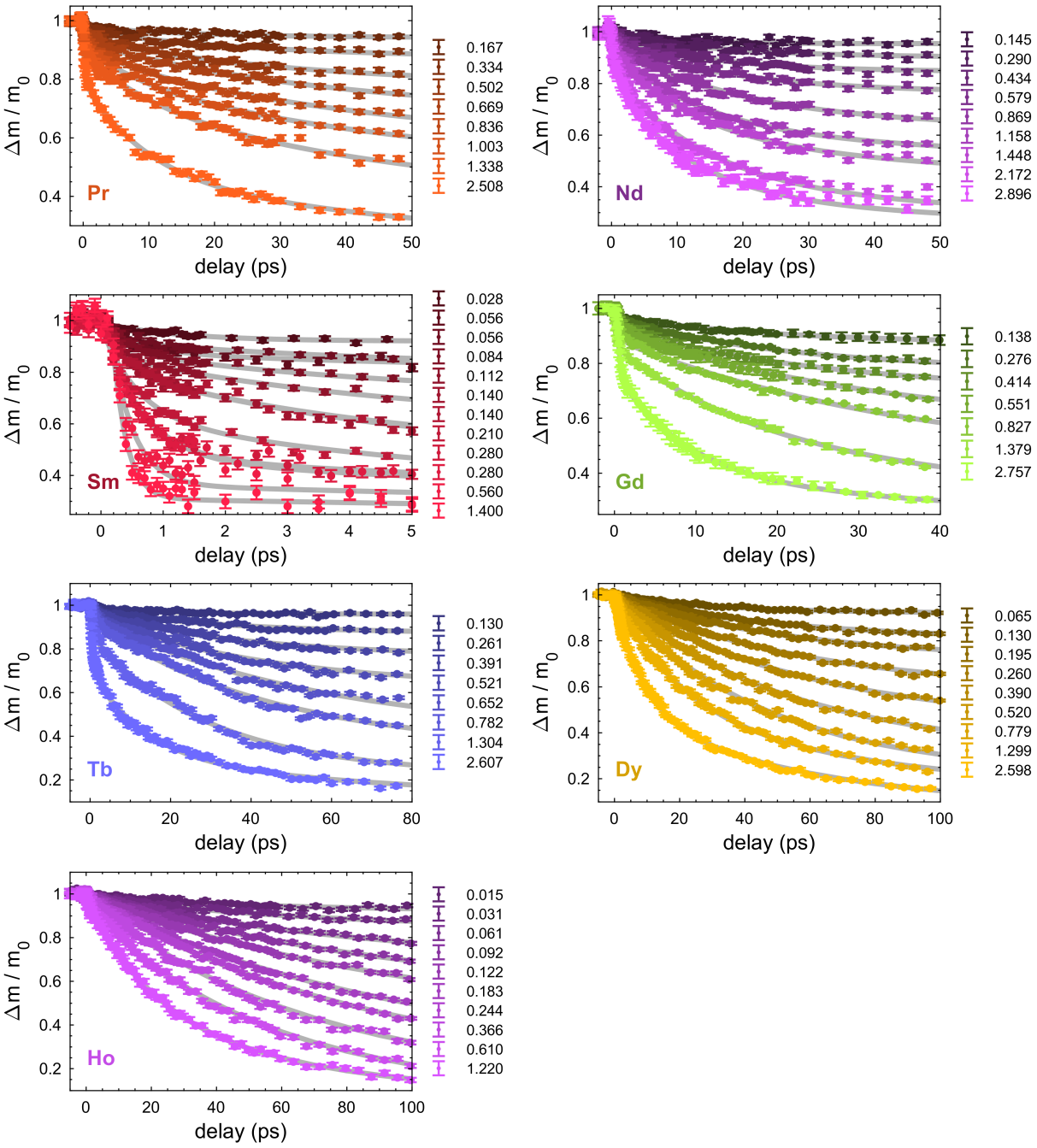

Figure 4.1: Demagnetization dynamics of $Ln\mathrm{Rh_2Si_2}$ at various fluences (symbols). *Ln* element is noted in the graphs. Lines are fits, as described in the text. Legend values represent absorbed fluences. Reproduced with permission from Springer Nature [Win+22].

FemtoSpeX at BESSY II [Hol+14] (see subsection 3.1.5).

We excite the materials with 1.55 eV laser pulses at various fluences, and the response is qualitatively identical in all materials: the excitation suppresses the ordered AF moment in a process that begins with a fast sub-picosecond drop, followed by a second slower drop (Figure 4.1). The fast drop accounts for a smaller fraction of the total reduction (except for *Ln*=Sm), and is vanishingly small for the heaviest *Ln* ions studied (Dy and Ho). However, quantitatively the materials' response times vary widely, ranging from 1 ps to over 100 ps. Two-step demagnetization is typical for lanthanide systems [Koo+10]. The two timescales are understood as one process,

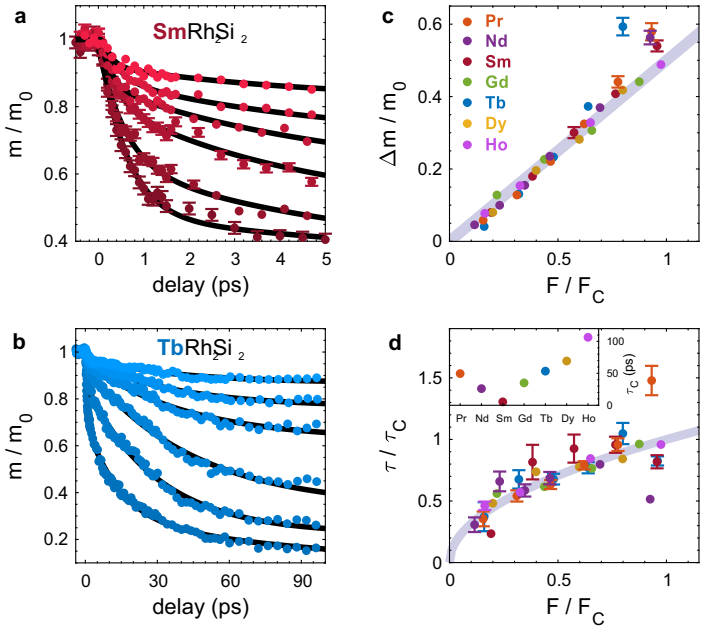

Figure 4.2: (a), (b) Pump-induced changes in the antiferromagnetically ordered $4f$ moment for Ln=Sm and Tb, respectively, representing data from both light and heavy lanthanides, highlighting the large difference in timescales and fluences. Different curves (in differently shaded color) correspond to different pump fluences: from F/F_c=0.38 to 1.9 for Sm (0.05 to 0.28 mJ/cm^2) and from F/F_c=0.32 to 3.2 for Tb (0.26 to 2.6 mJ/cm^2). (c) Total demagnetization amplitude as a function of normalized fluence F/F_c for all materials (line is guide for the eye). (d) Exponential time constant of the dominant (slower) drop as a function of normalized fluence. The data are normalized to τ_c, the value at F_c (inset). τ_c values are extracted for each compound from the best fit between all shown data and the relation $\tau/\tau_c = \sqrt{F/F_c}$ (gray curve; see text). Reproduced with permission from Springer Nature [Win+22].

which slows down when thermalization of the electronic and lattice degrees of freedom occurs before demagnetization is complete [Koo+10; Rot+12]. Such a case is expected for the large $4f$ moments of many lanthanides, which require more time to release their angular momentum, compared to the smaller moments in transition metal $3d$ systems.

4.2 Analysis and Discussion

4.2.1 Material-dependent critical fluences

For systematically comparing the behavior we observe in the LnRh$_2$Si$_2$ family, the excitation fluence was varied. For phenomenological description of the demagnetization dynamics we employed a following exponentially decaying function:

$$m(t)/m_0 = 1 - \Theta\left(t, t_0\right) \sum_i^2 A_i \left(1 - e^{-(t-t_0)/\tau_i}\right), \tag{4.1}$$

where t_0 is the photoexcitation time. A_i, τ_i are the amplitude and time constant of an exponentially decaying function, and $\Theta(t, t_0)$ is the Heaviside function where $\Theta(t, t_0) = 0$ for $t < t_0$ and $\Theta(t, t_0) = 1$ for $t > t_0$. Most of them exhibit sub-picosecond (<1 ps) and tens of picoseconds (∼10 ps) two-step demagnetization. Exemplary fitting results are plotted in Figure 4.2-a/b, and full fitting results are presented in Figure 4.1 (gray lines).

The total reduction in m scales linearly with fluence up to a material-dependent critical fluence F_c, which also varies widely between materials (Figure 4.2-c). We define F_c as the fluence at

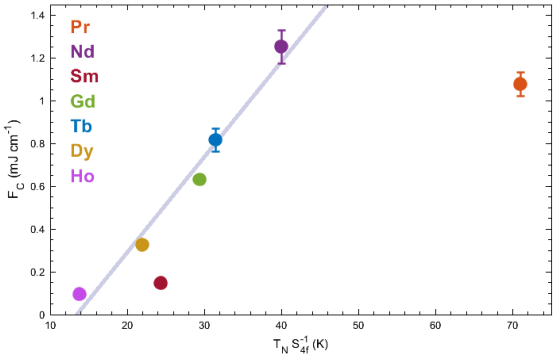

Figure 4.3: Critical absorbed fluence F_c as function of T_N/S, the ratio between the Néel temperature and the theoretical $4f$ spin moment. Reproduced with permission from Springer Nature [Win+22].

which the total demagnetization amplitude Δm reaches $m_0/2$. Figure 4.2-c/d presents the total demagnetization amplitude m/m_0 and the dominant (slower) time constant. The data are presented as functions of normalized fluence F/F_c, and the time constants τ are also normalized by τ_c, their values at the critical fluence F_c (inset), demonstrating similar scaling in all materials, despite the markedly different timescales and $4f$ filling. Exact τ_c values are extracted by fitting all data in Fig. 4.2-d for each material.

The relations to the critical fluences shown in Figs. 4.2-c/d demonstrate a universal behavior with respect to the critical fluence F_c, which is different for each material. We believe that F_c values are intrinsic quantities reflecting the material-dependent energy scale required to observe the same qualitative behavior seen in all other materials.

Fig. 4.3 presents the F_c values extracted for each material as functions of T_N/S_{4f}, the ratio between the Néel temperature and the theoretical $4f$ spin moment of the same material. This ratio is proportional to the Weiss molecular field, reflecting a measure of the mean magnetic coupling that is overcome by the excitation with F_c. Such a picture is valid when spin dynamics are dominated by classical processes, such that highly non-equilibrium processes or pure quantum fluctuations do not contribute.

We find that the optimal F_c values chosen for Ln=Sm and Pr do not scale as the rest of the materials. In the case of Ln=Sm, a significant portion of the total moment is demagnetized before electron-lattice thermalization (i.e. the sub-picosecond channel amplitude is larger), which can be attributed to its comparably smaller ordered $4f$ moments ($gJ = 5/6 \sim 0.7$). Quantum effects of such a small moment can be significant, and we propose that this is why $SmRh_2Si_2$ in Fig. 4.3 deviates from the linear behavior exhibited by most of the materials. The second outlier in Fig. 4.3 is $PrRh_2Si_2$. This system has in fact been previously studied, with focus on its unusually high ordering temperature of 70 K [Shi+10]. This is the reason for its deviation from the linear trend in Fig. 4.3, and a value closer to 35 K would place the value for $PrRh_2Si_2$ almost precisely on the interpolated curve. Shigeoka et al. demonstrated that the reason for this exceptionally large ordering temperature is the crystal-field-induced enlarged magnetic anisotropy, which causes this material to behave like an Ising magnet [Shi+10].

4.2.2 Fluence dependence of the demagnetization time scales

As shown in Fig. 4.2-d, the exponential demagnetization time scales on the laser fluence exhibit square-root dependence. To understand this, we interpret the underlying microscopic mechanisms in the demagnetization process, in the limit of low fluences. An effective spin temperature T is approximated to be linearly dependent on fluence F, which is the outcome of the empirical three-temperature model [Kam03]. Temperature enters naturally into the equation of motion of the atomistic magnetic moments S_i at site i by the stochastic Landau-Lifshitz-Gilbert equation (Eq.

(2.14)). Eq. (2.14) describes the evolution of the moment as a superposition of precessional motion around, and dissipative motion towards an effective field with thermal field $\vec{\zeta}$ with white-noice-like properties (Eqs. (2.15), (2.16)). From the correlation of thermal field $\vec{\zeta}$ (Eq. (2.16)) it follows that the thermal field averaged over time scales as $\sqrt{T}$ and, consequently, also $\frac{\partial S_i}{\partial t}$. Upon excitation, the total magnetic moment $M = \frac{1}{N}|\sum_i S_i|$ demagnetizes exponentially (approximated as $M = M_0 e^{-\frac{t}{\tau}}$, with an amplitude M_0 that is linearly proportional to fluence) [Koo+10]. Finally, we combine all relations with the fluence to reach:

$$\sqrt{F} \propto \frac{\partial M}{\partial t} = -\frac{1}{\tau} M \propto -\frac{M_0}{\tau} \propto -\frac{F}{\tau} \rightarrow \tau \propto \sqrt{F}. \tag{4.2}$$

Dependences of demagnetization times on fluence have been previously observed experimentally and reproduced by calculations [Atx+10; Men+14].

4.2.3 Equivalence of time-resolved experiments

Before we proceed to our main interpretation of this chapter, let's stop for a moment and discuss about the validity of the comparative analysis we have done so far. Despite the great similarity between the materials (see section 2.1.1), the different *Ln* ions require use of different *M* edge resonance energies for each material, rendering some differences between the experiments inevitable. Here we consider these differences.

The different *M* edge photon energies require different scattering angles to fulfill Bragg's law for the (001) reflection (see angles of the left column of Figure 3.2). The effect that this has on the probe depth is already accounted for by the data in Table. 3.1. However, since the pump arrives nearly collinearly with the probe, its angle also changes. This leads to only small differences in the refracted beam within the materials (15 - 18°), and the reflection coefficient at the Bragg angle is also similar (around 0.7; see Table B.1 in Appendix B). As such, we conclude the pump's depth profile is very similar in all materials.

The main concern surrounds the different probe depths, as shown in Table 3.1. These vary between the resonances by nearly a factor of two. This indicates that for different materials there is a different sensitivity to deeper layers. Deeper layers experience weaker pump excitation, reducing the observed pump effect. This would change the effective critical fluence values, and in worse case change the qualitative demagnetization behavior observed. Since all materials still fall on the systematic fluence-dependent demagnetization behaviors (Figure 4.2-c/d), we conclude that this effect is minor. Furthermore, the critical fluences systematically scale with the Néel temperature (Figure 4.3), further indicating that effect of the varying probe depths is minor. Lastly, the variation in ZPM resolution (Table 3.1) also affects the probe depth, such that higher values increase the contribution of deeper layers. We find no qualitative effect of this issue.

4.2.4 Exchange scaling of angular momentum transfer rate

Different Ln^{3+} ions vary appreciably in their moment sizes $gJ\mu_B$ (μ_B, g and J are Bohr's magneton, the Lande factor and the total $4f$ angular momentum quantum number, respectively), ranging from $0.7\mu_B$ to $10\mu_B$. To account for the varying moment sizes, and given the universal dynamics observed, we facilitate a more direct comparison of the demagnetizations by considering angular momentum transfer rate α, in units of μ_B ps^{-1}. These are calculated separately for the two demagnetization steps from the total moment J, but since they both represent the same physical process, we focus on the slow step, which we clearly resolve in all compounds. We find that α exhibits a linear relation to the *de Gennes factor* $G = (g-1)^2 J(J+1)$ (Figure 4.4-a), which approximates the projection of the spin $\vec{S}$ on $\vec{J}$, squared [Ell+72]. De Gennes scaling has been experimentally demonstrated in several $4f$ systems [Ell+72; Koe65] for quantities including the interlayer spin turn angle [Koe65; DS63] and magnetic ordering temperatures, and therefore also for the strength of RKKY coupling [Ell+72].

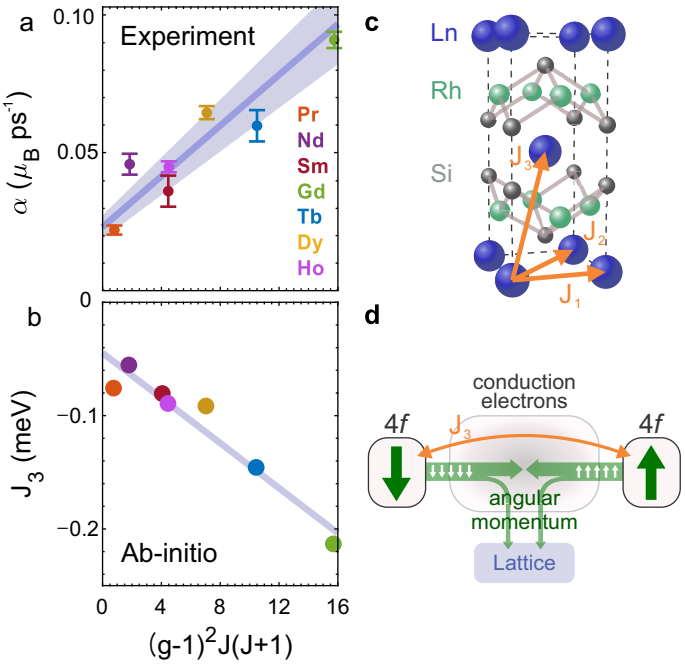

Figure 4.4: (a) Experimental values of the maximal angular momentum transfer rates (explanation in main text) as a function of the de Gennes factor $G = (g-1)^2 J(J+1)$. Data are shown for F/F_c=0.37 (other fluences behave very similarly). The best fit to a linear trend is presented, with a shaded area representing the error margin (slope:$(4.5\pm0.6)\times10^{-3}\mu_B$/ps; offset:$(2.3\pm0.4)\times10^{-2}\mu_B$/ps. (b) Calculated RKKY coupling between the nearest antiferromagnetically aligned Ln ions, also plotted against G. The line is a guide for the eye. (c) Sketch of an extended unit cell with the nearest RKKY couplings indicated; J_3 is the interlayer coupling. (d) Diagram depicting the flow of $4f$ angular momentum after excitation, in which conduction electrons mediate the flow between $4f$ states on antiparallel sites, as well as the flow to the lattice. Reproduced with permission from Springer Nature [Win+22].

The linear relation we observe strongly suggests that ultrafast demagnetization in $Ln\mathrm{Rh_2Si_2}$ antiferromagnets depends on the strength of RKKY coupling between antiferromagnetically aligned moments and is therefore governed by the angular moment transfer between opposite spins. To test this, ab initio calculations of all primary RKKY couplings of $Ln\mathrm{Rh_2Si_2}$ were performed using the density functional theory calculations by our theory collaborator (see Appendix A). These predict that the inter-planar coupling J_3 (between antiparallel spins) indeed scales linearly with G. By contrast, the in-plane couplings J_1 and J_2 do not show a clear trend with the de Gennes factor (Figure 4.5).

Note that the linear scaling of α does not cross the origin (Figure 4.4-a). This suggests a contribution from an additional angular momentum transfer channel, independent of G, and therefore independent of $4f$ occupancy (that is, a process that is nearly the same in all $Ln\mathrm{Rh_2Si_2}$ materials). One such process is the dissipation of $4f$ angular momentum to the lattice through the conduction electrons. To analyse this, we can consider a scenario in which angular momentum transfer between opposing $4f$ spins is turned off. The $4f$ demagnetization would then depend on two processes, (1) the transfer of $4f$ angular momentum to the conduction electrons, and (2) its dissipation from there to the lattice. The first process is governed by on-site exchange (and therefore by G), so we could assume that it is faster than the second process. However, since the conduction electron moment is small, it represents a bottleneck for angular momentum transfer such that process (1) is limited by the rate of process (2), and the observed $4f$ demagnetization would thus be limited by process (2) in a similar way in all $Ln\mathrm{Rh_2Si_2}$ materials. When the $4f$ spin-spin channel is turned back on,

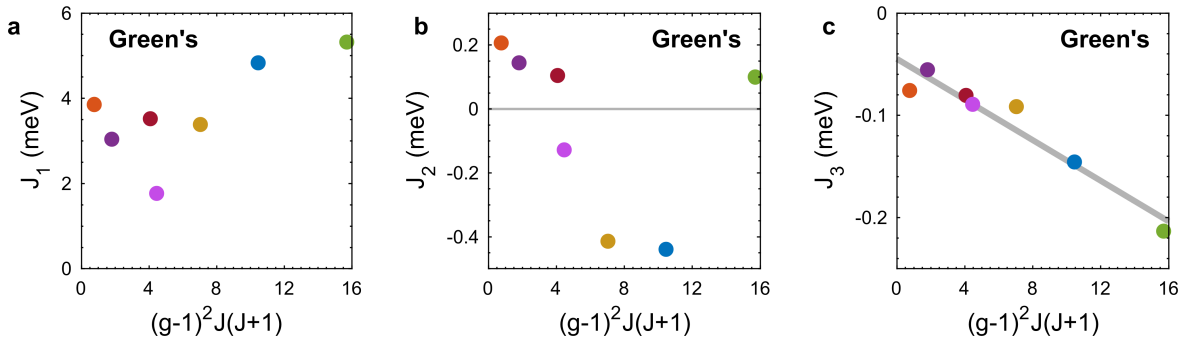

Figure 4.5: The three nearest neighbor couplings between Ln ions in $Ln\mathrm{Rh_2Si_2}$ systems, as functions of de Gennes factor, calculated with Green's function methods (see Appendix A). The numbering of each coupling follows Fig. 4.4-c. Reproduced with permission from Springer Nature [Win+22].

it works in parallel to process (2), so this limit is relaxed by the additional angular momentum transfer rate, leading to the linear trend in Fig. 4.4-a. The angular momentum transfer scenario we describe is sketched in Fig. 4.4-d. The bottleneck aspect is similar to the case of $sp-d$ FM semiconductors [CS07; Wan+08]. Previous works have discussed another channel primarily in the context of FM systems, in which the $4f$ shell couples directly to the lattice [Wie+11; Fri+20; ALW21]. Such a channel should depend on the $4f$ occupation and on G via the strength of spin-orbit coupling, which shows a non-monotonous dependence on G [JM91]. While our data confirm that the dominating contribution to the angular momentum transfer rates depends on the strength of the RKKY interaction, we cannot rule out additional contributions within the scatter of the data around the line.

Our results underline the importance of angular momentum transfer directly between opposite moments, as a channel that can dominate the entire process. This is in line with reports in other RKKY-mediated systems, such as the AF phases of lanthanide metals. Notably, in metallic Dy, which harbours FM and AF phases in different temperature ranges, an efficient demagnetization channel in the AF phases was recently observed, which is absent in the FM phase [Thi+17]. This is understood as the RKKY-mediated spin-spin channel we discuss here, and these observations are also in line with $4f$ demagnetization in AF metallic Ho [Ret+16]. However, demagnetization in the FM system Tb reportedly also exhibited an ultrafast channel like AF Dy [Wie+11]. The authors of the Dy work concluded that this was an extrinsic effect due to spin transport [Thi+17]. The difference in demagnetization rates between these three isostructural ferromagnets (Gd, Tb and Dy) were therefore understood as due to different coupling strengths between the $4f$ shell and the lattice, with a particularly weak coupling for the half-filled $4f$ shell of Gd.

4.3 Conclusion

In conclusion, we have investigated the role of direct angular momentum transfer between spin sublattices in the ultrafast magnetization dynamics of $4f$ antiferromagnets. By a systematic comparison of the ultrafast angular momentum transfer rates with ab initio calculations, we find that the rate of this transfer channel is proportional to the magnitude of the antiferromagnetic indirect (RKKY) exchange coupling. Our findings open avenues for ultrafast control of magnetization, for example, by tuning indirect exchange coupling through manipulation of the conduction electrons (Chapter 5) via doping, voltage biasing or applied pressure, or even transiently, for example through photodoping, without affecting the magnitude of the $4f$ moments themselves. The implications of our results are not limited purely to antiferromagnets, as direct angular momentum transfer can also occur between inequivalent spins in, for example, ferrimagnets [Hen+19; Ber+14; Men+12] or alloys [Fer+17] such as $\mathrm{Gd}_{1-x}\mathrm{Tb}_x$, where direct Gd-Tb angular momentum transfer was demon-

strated [Esc+14]. Such control over angular momentum transfer rates is also essential for the design and optimization of new device functionalities, such as ultrafast all-optical switching, which has been shown to depend on angular momentum transfer between magnetic sublattices [Ost+12; Ost+11]. The ability to tune the demagnetization rate of selected sublattices and the transfer rate between them opens the possibility to engineer such devices, either shortening or prolonging the short-lived collective spin states that enable such effects [Rad+11].

This page is intentionally left blank.

Chapter 5

Singling out the role of the conduction electrons in ultrafast spin dynamics of $4f$ antiferromagnets

As Eq. 2.10 shows, conduction electrons play a key role in determining the strength of the RKKY interaction. It determines the non-local susceptibility χ of conduction electrons around E_F. While the role of the localized $4f$ moments has been explored extensively in ultrafast spin dynamics of lanthanides [Wie+11; ALW21; Fri+20; Win+22], the role of the itinerant conduction electrons has received less attention. The reason for this is mainly because it is difficult to systematically modify only the conduction electrons in $4f$ magnets. As discussed in Chapter 2, elemental lanthanides share almost identical conduction electrons. Therefore, it is difficult to deduce the role of the conduction electrons from comparative analysis of lanthanides magnetism. Furthermore, since elemental lanthanides do not share identical lattice and magnetic structures (Table 2.1) [JM91], to single out the role from comparative analysis of the ultrafast spin dynamics becomes even more difficult.

As shown in Chapters 3 and 4, members of the antiferromagnetic $Ln\mathrm{Rh_2Si_2}$ family (Ln: Pr - Ho) shares nearly identical lattice and magnetic structures exhibiting comparably different ultrafast spin dynamics and successfully singled out the role of the localized $4f$ moments in ultrafast spin dynamics of $4f$ antiferromagnets. As a continuation of the previous chapter, in this chapter, we employ a similar family of $4f$ antiferromagnets $\mathrm{Gd}T_2\mathrm{Si_2}$ (T= Co, Rh, Ir) to single out the role of the itinerant conduction electrons in ultrafast spin dynamics of $4f$ antiferromagnets. We modify the itinerant conduction electrons by swapping transition metal ions in between the antiferromagnetically coupled $4f$ moments (Fig. 5.1-a), and explore ultrafast spin dynamics of $4f$ antiferromagnetic ordering employing time-resolved resonant magnetic soft x-ray diffraction (trRXD) and first-principles calculation.

5.1 Experimental results

5.1.1 Photon-energy dependence of the magnetic diffraction peaks

The main point in this chapter is to compare experimental ultrafast spin dynamics from different materials $\mathrm{Gd}T_2\mathrm{Si_2}$. An important part of this comparative analysis is to have very similar experimental conditions. But even with this, different materials can have different optical properties. Therefore, we need to account for optical properties of the samples to have a meaningful and valid comparison. That is the reason why we study photon energy dependence of the magnetic diffraction peaks around the Gd M_5 absorption edge. $\theta - 2\theta$ scans of the magnetic diffraction intensity measured at various energies are presented in Figures 7.1 ($\mathrm{GdCo_2Si_2}$), 3.2 ($\mathrm{GdRh_2Si_2}$) and 5.2 ($\mathrm{GdIr_2Si_2}$). As Fig. 5.3-a shows, resonant amplification of the magnetic [0 0 L] Bragg peak is the

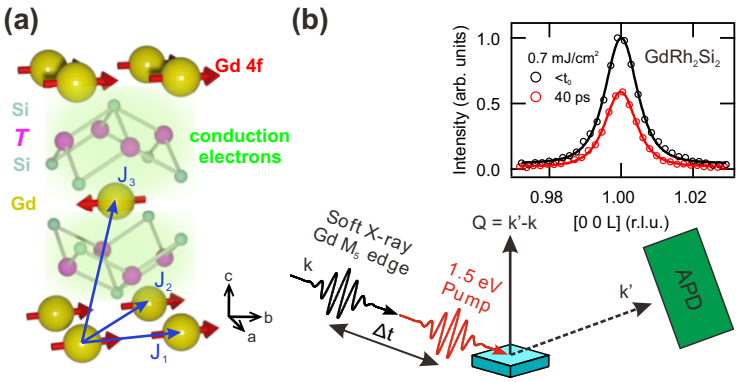

Figure 5.1: (a) Crystal structure of GdT_2Si$_2$. J_1, J_2 (J_3, J_4) indicate the RKKY coupling between the nearest and the next nearest neighboring Gd $4f$ moments in-plane (out-of-plane). (b) (bottom) Experimental setup of trRXD experiment. (top) Magnetic diffraction of (001) reflection of GdRh$_2$Si$_2$ before (black) and after the photoexcitation (red).

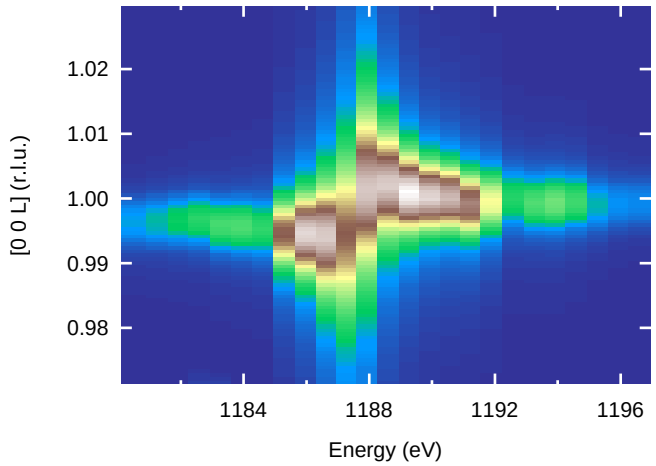

Figure 5.2: $\theta-2\theta$ scans of GdIr$_2$Si$_2$ at various incident photon energies around the Gd M_5 absorption edge. Color scale: From white to brown, yellow, green and dark blue, intensity decreases.

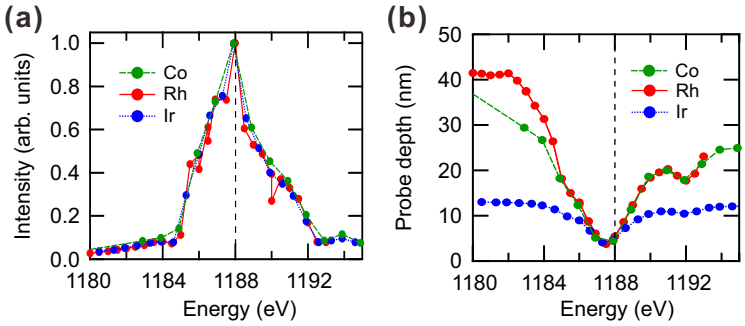

Figure 5.3: Photon-energy dependence of (a) magnetic diffraction intensity and (b) probe depth of GdT_2Si$_2$. For GdCo$_2$Si$_2$, [0 0 0.965] peak is chosen.

most prominent at 1188 eV for all the three samples, where $L = 1$ for T=Rh, Ir and $L \sim 0.965$ and 1.035 for T=Co as will be explained in the following subsection. As will be discussed in Chapter 7, both $L \sim 0.965$ and 1.035 peaks exhibit almost identical behavior. Therefore, in this chapter, we present only $L \sim 0.965$ peak for GdCo$_2$Si$_2$.

From the photon-energy dependent broadening of the magnetic diffraction peak we estimated

the penetration depth (=1/[2*2π*FWHM]) of the x-ray light (Fig. 5.3-b). At 1187.5 eV of photon energy at M_5 absorption edge, the penetration depths of the three samples are estimated to be ∼4 nm.

Around the resonance, while $GdCo_2Si_2$ and $GdRh_2Si_2$ exhibit comparable penetration depths in the energy window we measured, $GdIr_2Si_2$ exhibits exceptionally small penetration depth. This may be due to the exceptionally large density of $GdIr_2Si_2$, which enhances secondary scattering probability within the material. The density numbers of the three compounds support this postulate: $GdCo_2Si_2$ (7.34 g cm^{-3}) and $GdRh_2Si_2$ (8.55 g cm^{-3}) have comparable densities while $GdIr_2Si_2$ (12.73 g cm^{-3}) has much larger density.

Therefore, the probe depth of the long-range antiferromagnetic order by soft x-ray light at Gd M_5 absorption edge of the three samples are identical, which simplifies the comparative analysis between $Gd\,T_2Si_2$. In order to achieve the maximum resonant amplification of the signal with the same probe depth, photon energy of 1187.5 eV is chosen for the following experiments, unless specified.

5.1.2 Equilibrium temperature dependence

In order to characterize the magnetic properties of the materials, we measured the magnetic diffraction peaks of $Gd\,T_2Si_2$ (Fig. 5.4) af various sample temperatures. First, we conducted reciprocal space scans of [0 0 L] near $L = 1$. We observe commensurate resonant magnetic diffraction peaks [0 0 1] for $GdRh_2Si_2$ [Win+20] and $GdIr_2Si_2$ (Figure 5.4-a). In contrast, $GdCo_2Si_2$ is not. $GdCo_2Si_2$ exhibits two magnetic diffraction peaks at $L = 0.965$ and $L = 1.035$ at 20 K.

As sample temperature increases, the magnetic diffraction intensity gradually quenches. Interestingly enough, the magnetic diffraction peaks of $GdCo_2Si_2$ exhibits not only peak intensity quenching but also peak position shift upon heating (Figure 5.4-b). In order to extract this behavior accurately, we fit the peaks with a consistent model.

The diffraction peaks of the three samples are phenomenologically modeled with a Voigt profile for quantitative analysis. Though peak shape of the incommensurate diffraction peak of $GdCo_2Si_2$ is asymmetric, for consistent comparison of the three samples, a Voigt profile is applied. The magnetic order parameter of the three samples i.e., the square root of the diffraction intensity is plotted along the sample temperature normalized by T_N of each sample in Figure 5.4-c. The three samples exhibit quenching of AF order upon heating; while $GdRh_2Si_2$ and $GdIr_2Si_2$ demagnetize resembling the mean-field-like behavior of S=7/2 (∼Gd), $GdCo_2Si_2$ exhibit significantly different demagnetization behavior. Equilibrium properties of $GdCo_2Si_2$ will be discussed in depth in Chapter 7.

5.1.3 Femtosecond dynamics of long-range Gd 4*f* antiferromagnetic ordering

Femtosecond dynamics of the [0 0 L] magnetic diffraction peak amplitude for various pump fluences are presented in Fig. 5.5. For $GdRh_2Si_2$, peak amplitudes have been separated from a transient reorientation of its magnetic in-plane orientation based on a procedure combining several azimuthal orientations [Win+20]. Since $GdCo_2Si_2$ exhibit transient peak shift (Fig. 5.6-a), to account for intensity loss from the shift, the peak amplitudes for $GdCo_2Si_2$ have been corrected to reconstruct the actual peak amplitude dynamics. The correction process will be detailed in the following subsection 5.2.1.

While all three compounds exhibit similar demagnetization behavior in general, there are some notable differences. First, for $GdRh_2Si_2$ and $GdIr_2Si_2$, the normalized diffraction amplitude dynamics exhibit a two-step decay, with time constants of ∼1 ps, and ∼10ps as determined using an exponential fitting procedure, followed by a slow recovery after ∼100 ps. In contrast, for $GdCo_2Si_2$, the ∼1 ps decay component is nonexistent. Second, the amount of absorbed fluence to trigger the same amount of the demagnetization is notably different, with $GdRh_2Si_2$ required the strongest fluence, and $GdCo_2Si_2$ the weakest (see legend in Fig. 5.7-a, and see Appendix B for calculation of

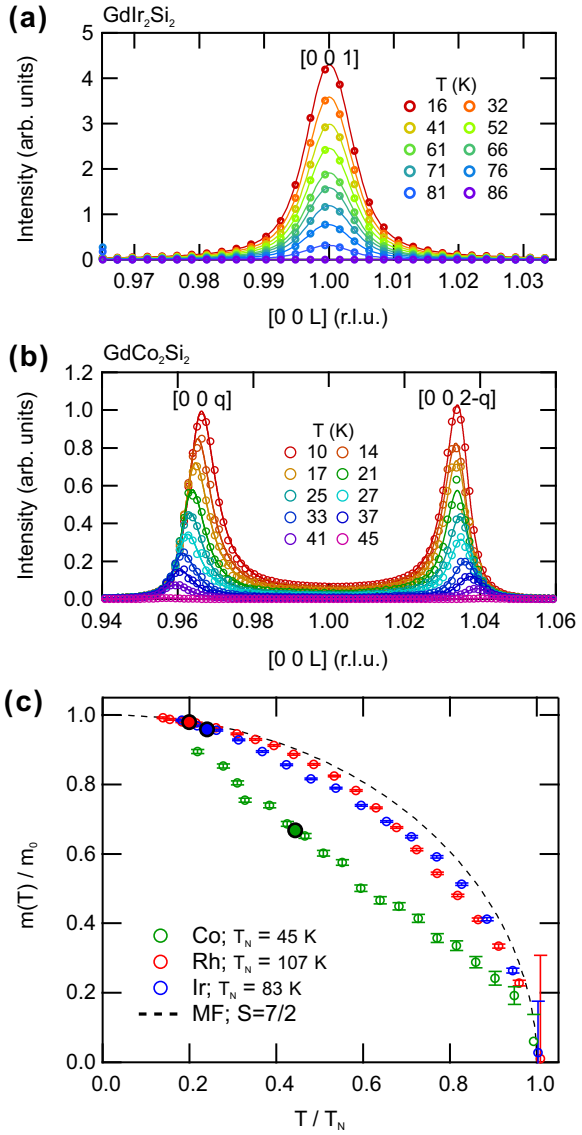

Figure 5.4: Temperature-dependent evolution of the [0 0 L] magnetic diffraction amplitude(s) of (a) $GdIr_2Si_2$ and (b) $GdCo_2Si_2$. (c) Temperature-dependent evolution of the long-range antiferromagnetic order of GdT_2Si_2. Larger solid circles indicate the staggered magnetization of each material at 20 K; GdT_2Si_2 samples are 67.1% (Co) 97.7% (Rh) 96.1% (Ir) magnetized, respectively.

the absorbed fluence). Finally, differences in the demagnetization rate are apparent, with $GdRh_2Si_2$ showing the fastest and $GdCo_2Si_2$ the slowest dynamics.

5.2 Analysis

5.2.1 Reconstructing the actual peak intensity dynamics of $GdCo_2Si_2$

Since $GdCo_2Si_2$ exhibits transient change in [0 0 L] upon pump excitation (Fig. 5.6-a), diffraction intensity dynamics acquired at constant momentum transfer does not accurately represent the actual peak intensity dynamics. In order to reconstruct the actual peak intensity dynamics, we measured the transient evolution of the diffraction peak of $GdCo_2Si_2$ at selected fluences (0.17. 0.34, 0.68 mJ/cm2) and at selected delays ($< t_0$, t_0+15, 30, 50, 75, 100, 200, 1000, 1250 ps) (Fig. 5.6-a). The delay scans of $GdCo_2Si_2$ are acquired at the "shoulder" of the peak (the vertical dashed line) to minimize the intensity loss from the shift. Due to asymmetric shape of the incommensurate

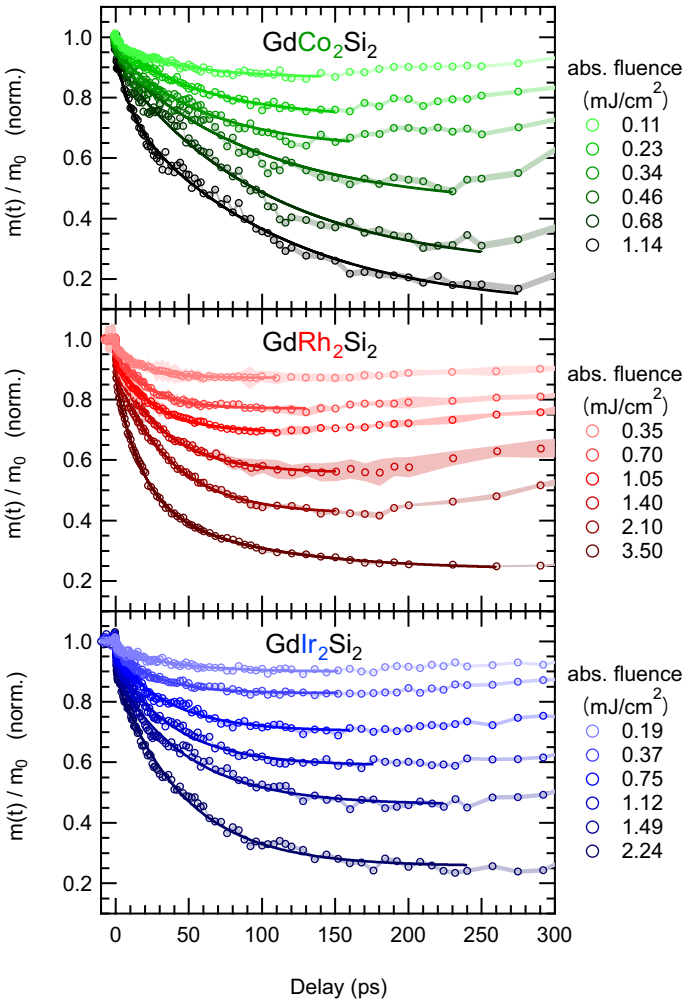

Figure 5.5: Temporal evolution of the normalized magnetic diffraction amplitudes of Gd T_2Si_2 upon photoexcitation. Note that the magnetic order dynamics of $GdCo_2Si_2$ is corrected for transient peak shift (subsection 5.2.1). Solid lines are phenomenological exponential fitting (Eq. (5.4)).

diffraction peak of $GdCo_2Si_2$, it is modeled with a phenomenological Doniach-Sunjic function for precise description:

$$DS(L;\alpha,\Gamma,Q) = A\left(\frac{\cos\left[\frac{\pi\alpha}{2}+(1-\alpha)\tan^{-1}\left(\frac{L-Q}{\Gamma}\right)\right]}{\left(\Gamma^2+(L-Q)^2\right)^{(1-\alpha)/2}}\right), \tag{5.1}$$

where L is position in reciprocal space [0 0 L]. A is the amplitude of the peak, Q is the effective peak position, Γ is the effective peak width, and α determines the degree of asymmetry of the peak. For $\alpha = 0$, Eq. 5.1 becomes Lorentzian profile [Moe+22], and asymmetry increases as α increases towards 1. The modeled intensity at the delay scan acquisition point (vertical dashed line) I_{probe} is clearly different from the modeled maximum intensity of the peak $I_{max.}$. The ratio between the two (I_{probe} / $I_{max.}$) are plotted in Fig. 5.6-b. As we acquired the diffraction peak at selected delays, the ratio at delay points in between the delay points that we acquired the entire diffraction peak has to be linearly interpolated for continuity:

$$Ratio\,(t) = Ratio\,(t_1) + \left(\frac{Ratio\,(t_2) - Ratio\,(t_1)}{(t_2 - t_1)}\right)(t - t_1) \quad \text{,where } t_2 > t_1. \tag{5.2}$$

Also, as we acquired the diffraction peaks at selected fluences, the ratio at other fluences in between the measured fluences has to be linearly interpolated using the delay-interpolated ratio

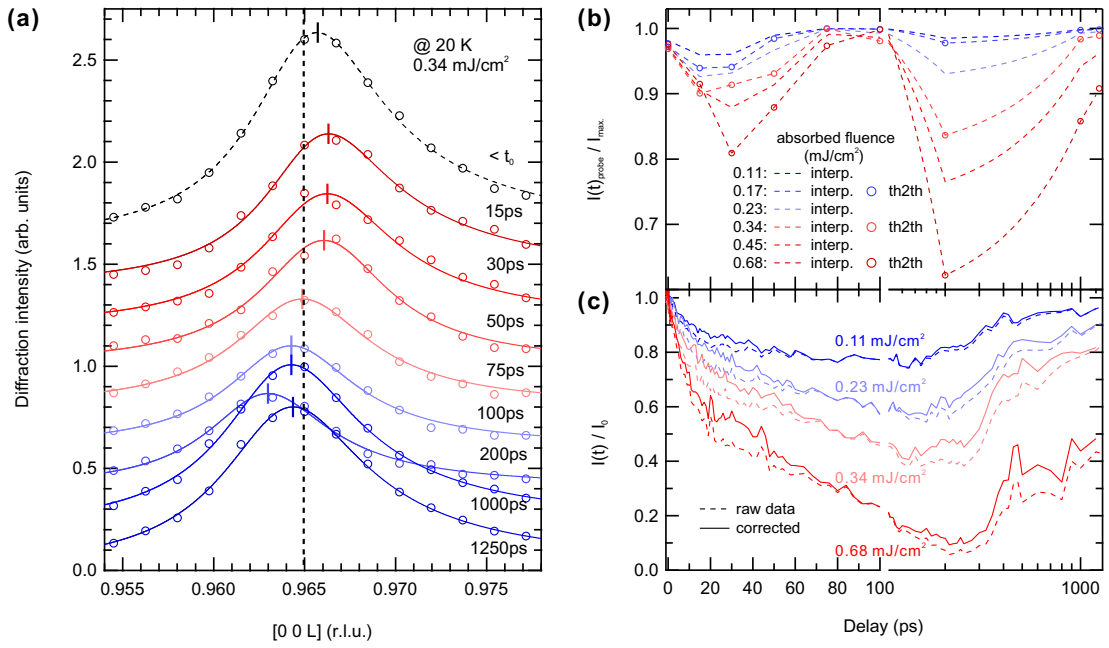

Figure 5.6: (a) Transient diffraction intensity evolution of [0 0 0.965] reflection of $GdCo_2Si_2$ upon ultrafast optical excitation at selected delays. The vertical dashed line indicates the diffraction geometry for acquiring delay scans (see text). (b) The ratio between the intensity for probing the delay scan I_{probe} and the actual maximum intensity of the magnetic diffraction intensity I_{max} at various pump fluences. Dashed lines are interpolated ratio dynamics for time delays and fluences not measured with $\theta - 2\theta$ scans in (a) (see Eqs. 5.2, 5.3 in text) (c) The raw diffraction intensity dynamics (dashed lines) and the corrected diffraction intensity dynamics (solid lines) at various pump fluences.

that we constructed in the previous step:

$$Ratio\,(f, t_0) = Ratio\,(f_1, t_0) + \left(\frac{Ratio\,(f_2, t_0) - Ratio\,(f_1, t_0)}{(f_2 - f_1)} \right) (f - f_1) \quad \text{,where } f_2 > f_1. \tag{5.3}$$

After preparing all the I_{probe}/I_{max} ratios for all the delays and fluences (Fig. 5.6-b), we corrected the intensity by dividing the raw delay scan intensity measured at the constant momentum transfer L by the I_{probe}/I_{max} ratio: $I_{corrected}\,(t_0, f_0) = I_{probe}\,(t_0, f_0)\,/Ratio\,(t_0, f_0)$

Fig. 5.6-c presents the corrected delay scans (solid lines) along with the raw delay scans (dashed lines) at selected fluences. As we see, the corrected intensity compensates the intensity loss from the transient peak shift.

5.2.2 Modeling demagnetization dynamics with exponentially decaying functions

For quantitative comparison of the demagnetization dynamics of the three materials, we modeled the demagnetization curves with a phenomenological exponentially decaying function with two time constants (Figure 5.7-a):

$$A(t) = 1 - \Theta\,(t, t_0) \sum_{i=1}^{2} A_i \left(1 - e^{-(t-t_0)/\tau_i}\right), \tag{5.4}$$

where A_i, and τ_i are amplitude and time constant of the exponentially decaying function, respectively. t_0 is the photoexcitation time. $\Theta\,(t, t_0)$ is the Heaviside function, where $\Theta\,(t, t_0) = 0$ for

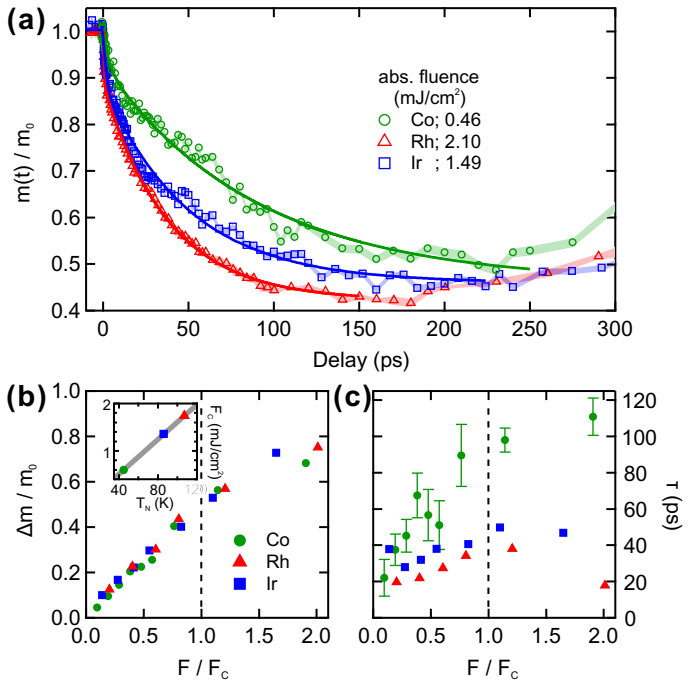

Figure 5.7: (a) Ultrafast dynamics of the normalized [0 0 L] magnetic diffraction amplitude of GdT_2Si$_2$ (T = Co, Rh, and Ir) at selected pump fluences acquired at a constant momentum transfer L. Note that the amplitude of GdCo$_2$Si$_2$ is corrected for the amplitude loss from the peak position shift dynamics (see subsection 5.2.1). Solid lines are exponential decaying functions for phenomenological description (Eq. (5.4)). (b) Demagnetization amplitude of the three materials plotted along the fluence normalized by the critical fluence F_c (see text) of each material. (Inset) The relation between the critical fluence and the Néel temperature of each material. A gray solid line is a linear fit (see text). (c) Demagnetization time constant of the three materials plotted along the normalized fluence.

$t < t_0$ and $\Theta(t, t_0) = 1$ for $t > t_0$. Figure 5.7- b/c present the fitting parameters A_i, and τ_i as function of fluence normalized to the critical fluence F_c, respectively. As in Chapter 4, F_c is defined for each material as fluence necessary to induce $m_0/2$ amount of demagnetization.

F_c of the three samples are 0.60 (Co), 1.74 (Rh), and 1.36 (Ir) mJ/cm^2, respectively. As the inset of Fig. 5.7-b shows, F_c and T_N has a scaling relation. This relation has been observed for LnRh$_2$Si$_2$ series as well (Figure 4.3). The slope for LnRh$_2$Si$_2$ in Figure 4.3 is 0.0457 ± 0.004 mJ/cm^2 K (Ln = Sm and Pr are excluded from the linear fit for the reason discussed in subsection 4.2.1). The corresponding slope for GdT_2Si$_2$ in the inset of Figure 5.7-b is $(7/2) \times 0.0184 \pm 0.0001 = 0.0644 \pm 0.0003$ mJ/cm^2 K, which is in the same order with LnRh$_2$Si$_2$ cases. Considering that GdRh$_2$Si$_2$ is not perfectly following the scaling relation among LnRh$_2$Si$_2$, this amount of difference is acceptable. Ref. [Win+22] explained that, for LnRh$_2$Si$_2$ (Ln = Pr – Ho), this scaling relationship between the critical fluence and T_N implies that the RKKY interaction between the antiferromagnetically coupled Ln $4f$ moments is the main coupling to determine their antiferromagnetism. Based on this interpretation, the fact that GdT_2Si$_2$ exhibits almost identical linear relation with LnRh$_2$Si$_2$ means that the antiferromagnetic RKKY interaction is the main physical interaction governing the ultrafast spin dynamics in GdT_2Si$_2$. Although GdCo$_2$Si$_2$ exhibits incommensurate spin order not following the mean-field-like behavior unlike the other two, it follows classical expectation (the Weiss molecular field) to some degree even in ultrafast dynamics since its ultrafast demagnetization behavior scales in temperature unit with other two materials which follow the mean-field-like behavior as shown in the inset of Figure 5.7-b. In other words, the mean magnetic coupling to be overcome is still explainable within a classical picture for the three GdT_2Si$_2$ samples. This, in

consequence, supports the validity of the comparative analysis of the ultrafast spin dynamics of GdT_2Si_2.

As shown in Figure 5.7-b, the demagnetization amplitudes share almost the same F/F_c dependence; below F_c, the amplitude linearly scales with the fluence and from above F_c, the amplitude saturates upon fluence increase (Fig. 5.7-b). Since $GdCo_2Si_2$ only exhibits slow demagnetization, only time constants of the ∼10 ps process are plotted in Fig. 5.7-c. They share similar F_c dependence, but with different timescales. The time constant scaling results agree with our previous observation of the raw data dynamics: $GdRh_2Si_2$ demagnetizes the fastest followed by $GdIr_2Si_2$, and $GdCo_2Si_2$. While the time constants of $GdRh_2Si_2$ and $GdIr_2Si_2$ increase towards F_c, the time constants of $GdCo_2Si_2$ simply increase with increasing pump fluence. For $GdCo_2Si_2$, due to its low T_N (45 K), we could not apply stronger pump fluence to explore the fluence dependence further as the sample suffered from average heating, meaning that it does not fully recover the initial magnetic order until the next pump excitation.

While the three materials share the same Gd $4f$ moments μ_{4f}=7.55μ_B, due to different T_N of each sample, the normalized staggered magnetization $m_{stag.}$ at 20 K of each sample is different; at 20 K, GdT_2Si_2 samples are 67.1% (Co) 97.7% (Rh) 96.1% (Ir) magnetized, respectively. Therefore, for accurate estimation of the demagnetization rate, we have to calculate the angular momentum transfer rate α with the following equation:

$$\alpha = \frac{m_{stag.}\,(T = 20K) \times \mu_{4f} \times A_{slow}}{\tau_{slow}} \tag{5.5}$$

A_{slow}, τ_{slow} are amplitude and time constants of the slow demagnetization process extracted from the above-mentioned exponential fitting, respectively. Similar to the time constant, $GdRh_2Si_2$ has the largest α followed by $GdIr_2Si_2$, and $GdCo_2Si_2$; at critical fluence, Rh: 0.078 μ_B/ps, Ir: 0.058 μ_B/ps and Co: 0.034 μ_B/ps. This seemingly simple experimental result is surprising because the only discernible difference among the three materials are T ions, which affect the population and susceptibility of the conduction electrons between the antiferromagnetically coupled Gd $4f$s (Fig. 5.1-a). In other words, the angular momentum transfer rate α of $4f$ antiferromagnets can change significantly by simply modifying the conduction electrons between the antiferromagnetically coupled $4f$ moments.

5.3 Discussion

In order to understand the mechanism behind of this experimental finding, our theory collaborator calculated exchange coupling constants and electronic densities of states (eDOS) of the three materials employing the density functional theory (DFT) introduced in Appendix A. According to our DFT calculations, in GdT_2Si_2, the conduction electrons are mostly of Gd $5d$ electrons character. Thus, the interaction between the local magnetic moments is mediated predominantly via spin-polarized $5d$ states of Gd. As Eq. (2.10) shows, the strength of the RKKY interaction $J_{RKKY} \propto |I|^2\chi$ depends on two factors: (i) The value of the local magnetic moments and (ii) the spin polarization of conduction electrons. The first factor modifies the overlap integral I between the $4f$ and conduction electron wave functions. In all the studied materials, the theoretical local magnetic moments are of the same size. Therefore, we can ignore the first factor for the moment. The second factor, the Gd $5d$ spin polarization around E_F is related to the non-local susceptibility χ. The spin polarization is calculated from the difference of the eDOS between majority- and minority-spin channels around E_F. Since we ignore the first factor, only the spin polarization of the conduction electrons can be responsible for any differences. In Fig. 5.8-a, we show the calculated Gd $5d$ spin polarization of the three compounds in the vicinity of the Fermi level. At the Fermi energy E_F, $GdRh_2Si_2$ has the largest spin polarization followed by $GdIr_2Si_2$ and $GdCo_2Si_2$. As shown in Fig. 5.8-b, the spin polarization at E_F also directly correlates with the strength of the RKKY interaction between the nearest in-plane and out-of-plane Gd $4f$ moments (J_1, J_3, respectively in

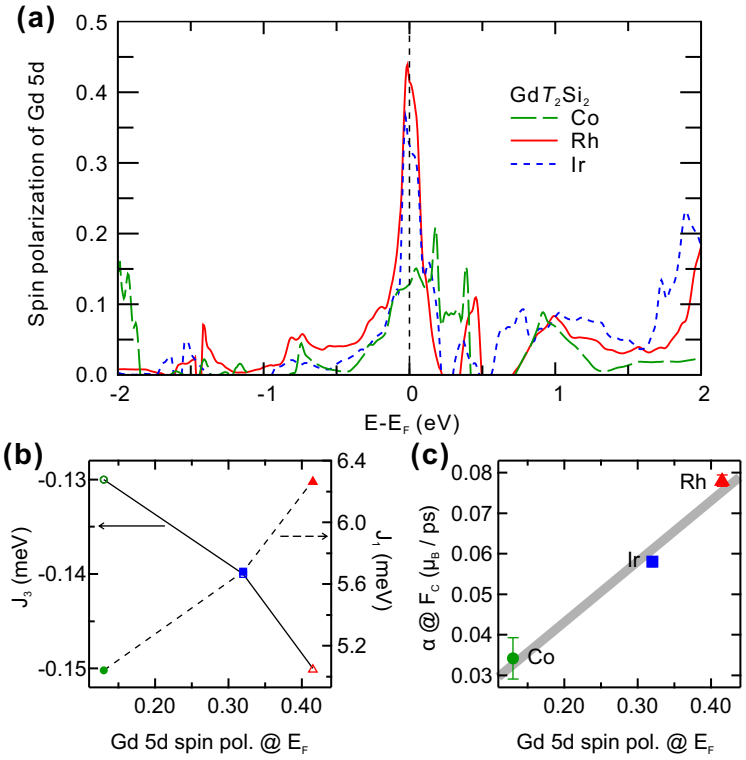

Figure 5.8: (a) The spin polarization of Gd 5d electrons of GdT_2Si$_2$. (b) The indirect RKKY exchange interaction between the nearest in-plane $4f$ moments J_1 (closed markers, dashed line) and the nearest antiferromagnetically coupled $4f$ moments J_3 (open markers, solid line) plotted along the calculated Gd 5d spin polarization. (c) The experimental angular momentum transfer rate plotted along the Gd $5d$ spin polarization of the three materials. A gray solid line is a guide to the eye for the scaling relation discussed in the text.

Fig. 5.1-a). We also find a clear scaling relation of the experimental angular momentum transfer rate with the Gd $5d$ spin polarization at E_F (Fig. 5.8-c). This tells us that the transition metal ions, which have zero magnetic moments, modify the distribution of the eDOS at the vicinity of the Fermi level. As the conduction electrons mediate the RKKY interaction, the change in eDOS at the Fermi energy effectively modifies non-local susceptibility χ and, in consequence, the strength of the RKKY exchange interaction, which scales with the angular momentum transfer rate in this family of $4f$ antiferromagnets as shown in Chapter 4. This finding proves that we can tune the strength of the RKKY interaction and the angular momentum transfer rate upon optical excitation by modifying only the conduction electrons of $4f$ magnets.

The behaviour of $5d$ electrons in GdT_2Si$_2$, explored in our calculations can be explained by two important factors. The first is related to the particular crystalline structure of GdT_2Si$_2$. As it was shown in Ref. [Hug+07], magnetic properties of rare earth compounds are highly sensitive to the unit cell volumes (as the result of the lanthanide contraction): a reduction of the unit cell volume leads to a reduction of $5d$ eDOS at the Fermi level strongly modifying the magnetic interaction in the system. In our case, GdCo$_2$Si$_2$ (150.0 $\mathring{A}^3$) has the lowest unit cell volume and, as a result, the lowest $5d$ eDOS and spin polarization at the Fermi level [Czj+89]. GdRh$_2$Si$_2$ (162.9 $\mathring{A}^3$) has the largest unit cell volume and, as a consequence, the largest eDOS and spin polarization at the Fermi level (the volume of GdIr$_2$Si$_2$ (156.0 $\mathring{A}^3$) is smaller than GdRh$_2$Si$_2$ and is larger than in GdCo$_2$Si$_2$, consistent with the obtained results) [KK15; Kli+20]. The second important factor is the extension of the transition metal wave functions. $3d$ Co orbitals are strongly localized in GdCo$_2$Si$_2$. Therefore, the hybridization between Si and Co states is much weaker than in GdIr$_2$Si$_2$ (Si - Rh $4d$) and GdRh$_2$Si$_2$ (Si - Ir $5d$). The vacant valence Si electrons interact therefore more

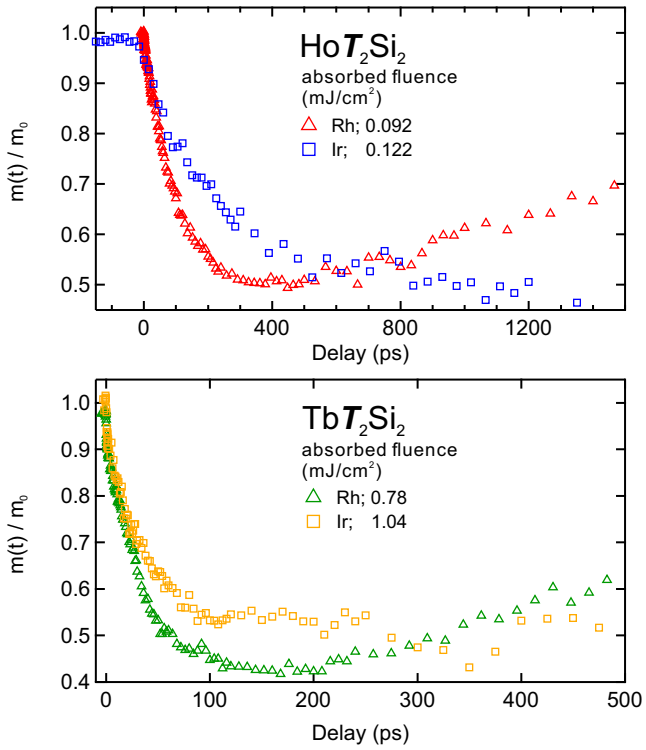

Figure 5.9: Temporal evolution of (001) magnetic diffraction amplitude of $Ln\,T_2Si_2$ (Ln=Tb, Ho; T=Rh, Ir) at a selected pump fluence. For the calculation of the absorbed fluence, since the optical constants for calculating the absorbed fluence of $Ln Ir_2Si_2$ were not available, the optical constants of $Ln Rh_2Si_2$ were arbitrarily applied based on the observation that the consisting atoms are 60% identical (one Ln and two Si ions) and that the reflectivity of $GdRh_2Si_2$ and $GdIr_2Si_2$ are almost identical (Table B.1).

with Gd $5d$ states reducing the $5d$ DOS and their spin polarisation at the Fermi level. Rh $4d$ states are more extended than Co $3d$ but less than Ir $5d$ orbitals. This would favour a stronger Si sp - Gd $5d$ hybridization, placing the Rh case between $GdCo_2Si_2$ and $GdIr_2Si_2$. However, the larger c/a ratio in $GdRh_2Si_2$ reduces the interaction between Si sp bands and Gd $5d$ states. In addition, the first factor, the lanthanide unit cell volume, increases the $5d$ eDOS at the Fermi level in $GdRh_2Si_2$ making it have the largest Gd $5d$ spin polarization at E_F.

To crosscheck whether our finding in Gd case is solely due to conduction electrons modification, we measured ultrafast demagnetization dynamics of antiferromagnetic $Ln\,T_2Si_2$ (Ln=Tb, Ho; T=Rh, Ir) as well (Figure 5.9). Similar to Ln = Gd case, compounds with Ir ions demagnetize slower than that with Rh ions when compared with curves exhibiting similar amount of demagnetization amplitude. Therefore, we argue that the differences in the angular momentum transfer rate is due to T ions and is universal among other $Ln\,T_2Si_2$ compounds as well.

5.4 Conclusion

In this chapter, we studied the role of the conduction electrons in ultrafast spin dynamics of $4f$ antiferromagnets. We modified the conduction electrons only by effectively swapping T ions in antiferromagnetic $Gd\,T_2Si_2$ (T= Co, Rh, Ir), and measured femtosecond dynamics of magnetic diffraction intensity at various pump fluences employing time-resolved resonant elastic magnetic soft x-ray diffraction. The three samples share comparably similar demagnetization behavior upon optical excitation at 1.55 eV: We observed a linear relation between T_N and F_c. This suggests that the ultrafast spin dynamics of the three samples are governed by the antiferromagnetic indirect

RKKY exchange interaction of Gd $4f$ moments mediated by conduction electrons from Gd $5d$, Si and T ions, like other family 4f antiferromagnets $Ln\mathrm{Rh_2Si_2}$ (Chapter 4). However, modifying conduction electrons drastically changes the angular momentum transfer rate α (α: $\mathrm{GdRh_2Si_2}$ > $\mathrm{GdIr_2Si_2}$ > $\mathrm{GdCo_2Si_2}$). The first-principles calculations employing density functional theory (DFT) of the electronic density of states and the exchange coupling constants explain that the spin polarization of $5d$ electrons scales with the antiferromagnetic exchange coupling J_3 in the three materials, and hence also with the experimental angular momentum transfer rate. This finding provides insights that may prove useful towards designing lanthanide-based devices by tuning itinerant conduction electrons, which are much easier to modify and access compared to localized $4f$ moments.

This page is intentionally left blank.

Chapter 6

Robust magnetic order upon ultrafast excitation of an $4f$ antiferromagnet

This chapter was published in "Robust magnetic order upon ultrafast excitation of an antiferromagnet" arXiv: 2207.00789, (2022) as a preprint.

The photo-induced ultrafast spin dynamics of lanthanides is governed by the intricate flow of energy and angular momentum between the conduction electron, lattice and localized $4f$ spin subsystems. While various models are commonly employed to describe these dynamics, a prominent example being the microscopic three temperature model (M3TM), systematic, quantitative comparisons to both the dynamics of energy flow and magnetic order are scarce. Here, we investigate the ultrafast magnetic order dynamics and transient electronic temperature in the layered intermetallic antiferromagnet, $GdRh_2Si_2$ using time- and angle-resolved photoelectron spectroscopy (trARPES) and time-resolved resonant magnetic soft x-ray diffraction (trRXD) (Fig. 6.1-a). Due to the localized nature of the $4f$ moments, magnetic order is mediated through the spin-polarized itinerant Gd $5d$, Si and Rh conduction electrons via the indirect RKKY exchange interaction. Our choice of experimental methods allows us to get a full picture on the ultrafast dynamics of both localized and itinerant magnetic order, as well as the electronic temperature evolution after excitation: Surface-sensitive trARPES allows for the simultaneous analysis of the magnetization-dependent transient exchange splitting of a Si-derived surface state and of the time-dependent electron distribution function (Fig. 6.1-b). It thereby provides the unique opportunity to study the ultrafast dynamics of both the electronic temperature and the in-plane surface magnetization of itinerant conduction electrons within a single experiment. Additionally, bulk-sensitive trRXD is used to study directly the temporal evolution of long-range, out-of-plane AF order of the localized Gd $4f$ moments (Fig. 6.1-c). Then, we apply a suitable M3TM for AF systems based on the LLB equation, and *quantitatively* compare the model's prediction using the measured electronic temperature as input to the magnetic order dynamics of both the itinerant conduction electrons and the localized $4f$ moments from trARPES and trRXD, respectively, as schematically shown in Fig. 6.1-d. While the model allows for a good qualitative description of the ultrafast magnetic order dynamics, for increasing excitation fluence, the material shows an increased robustness against demagnetization. Phenomenologically, we can describe this behavior with a transiently enhanced Néel temperature. Additionally, the initial, sub-ps demagnetization significantly exceeds the model prediction, suggesting an enhanced inter-sublattice momentum transfer rate in the non-thermal system.

6.1 Experimental results

The following experiments were conducted at 20 K unless specified.

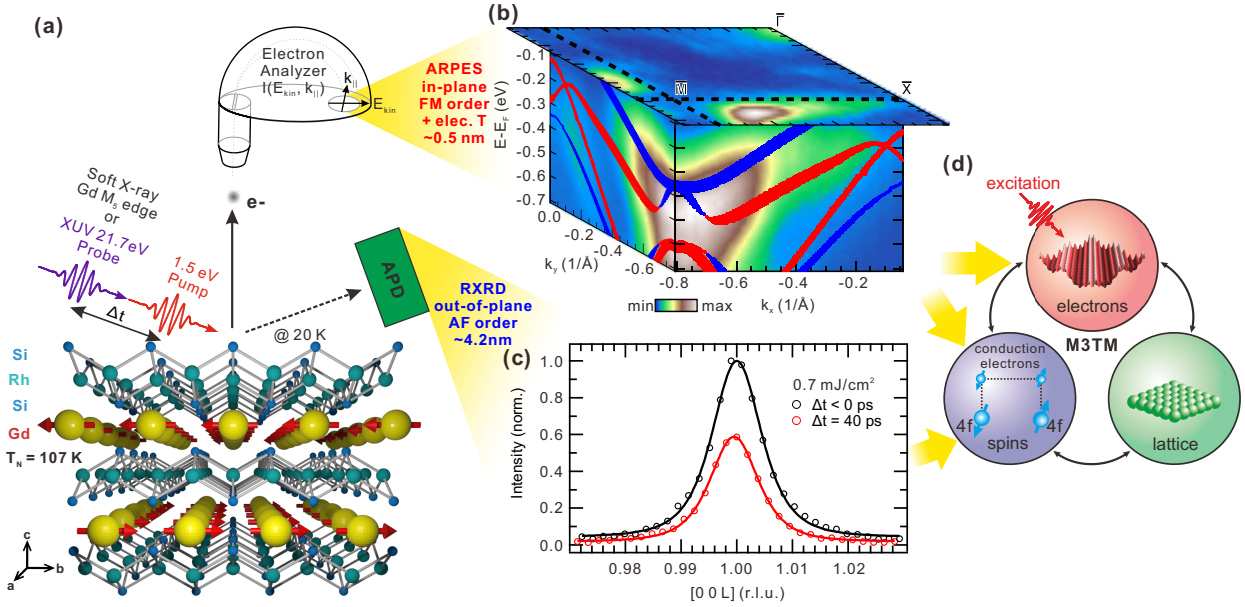

Figure 6.1: (a) Crystal structure of $GdRh_2Si_2$ and sketch of experimental setups. (b) Volumetric representation of the ARPES intensity around the $\overline{\text{M}}$ point of the surface Brillouin zone of the Si-terminated surface of $GdRh_2Si_2$. The constant energy contour at E-E$_F$ = 0 shows the Fermi surface topology (integration width = 7.7 meV). The direction of the k$_x$ and k$_y$ cuts along the $\overline{\text{M}}$-$\overline{\text{X}}$ directions are indicated by dashed lines. A density functional theory (DFT) calculation of the spin-resolved surface state band structure is overlaid [Güt+16]. Majority (minority) spin states are shown as red (blue) ribbons. (c) (001) magnetic diffraction peak of $GdRh_2Si_2$ measured with tr-RXD. 40 ps after excitation (red), the diffraction intensity is suppressed compared to the diffraction intensity before t$_0$ (black). (d) Schematics of the M3TM for lanthanide-based antiferromagnets. The M3TM takes the electronic temperature dynamics from trARPES measurement as an input to predict magnetic order dynamics of the itinerant conduction electrons and the localized 4f magnetic moments, which will be compared with the experimental results from (b) trARPES and (c) trRXD measurements in Section 6.2.

6.1.1 Femtosecond dynamics of long-range Gd 4f antiferromagnetic ordering

Using resonant magnetic x-ray diffraction we measured the response to photoexcitation of the (001) intensity of $GdRh_2Si_2$. The femtosecond dynamics of the (001) diffraction peak amplitude recorded at constant momentum transfer Q is shown in Fig. 6.2-a for selected pump fluences (squares). Here, as discussed in the previous chapters, the peak amplitudes have been separated from a transient reorientation of the magnetic structure based on a procedure combining several azimuthal orientations [Win+20]. The normalized diffraction amplitude dynamics exhibits two-step decay according to a biexponential fit with time constants of a < 1 ps, and a $\sim$10 ps [Win+20], as commonly observed in lanthanide magnets, followed by a slow recovery after $\sim$100 ps.

6.1.2 Exchange splitting of the Si-derived metallic surface state

Next, we used trARPES to study the photo-induced evolution of a Si-derived surface state residing at the large projected band gap at the $\overline{\text{M}}$ point (Fig. 6.1-b). In $GdRh_2Si_2$, the localized Gd 4f electrons predominantly carry the magnetic moments, and the conduction electrons from Rh, Si and Gd 5d6s mediate the RKKY interaction between the Gd layers [KK15; Win+22]. In the AF state, the surface state exhibits a sizeable exchange splitting, which is mediated via RKKY exchange coupling to the localized Gd 4f moments from the sub-surface in-plane FM Gd layer [Güt+16]. The exchange splitting sets in at 90 K, notably lower than the bulk Néel temperature $T_N = 107$

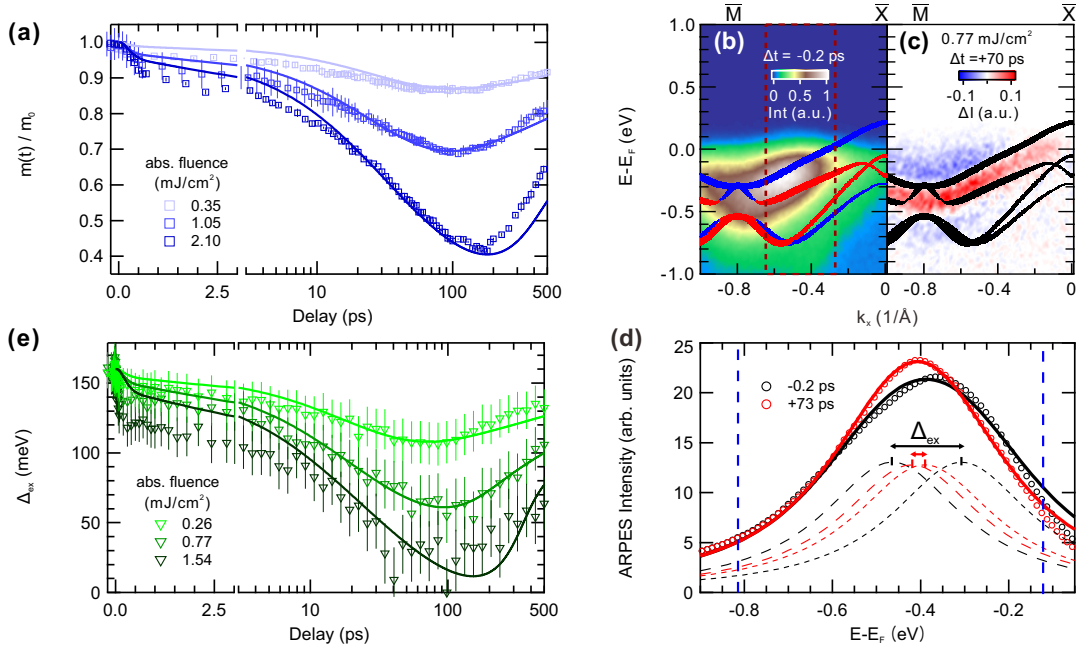

Figure 6.2: (a) Ultrafast dynamics of the normalized (001) magnetic diffraction amplitude (squares). Solid lines show the simulated magnetization dynamics by the M3TM (see Section 6.2) taking the probe depth of RXD into account. Note that the second half of the time axis is log-scaled. (b) ARPES intensity at -0.2 ps and (c) its intensity difference upon pump excitation at 70 ps delay normalized by the maximum intensity at -0.2 ps. The ARPES intensity is homogeneously increased along the dispersion of the surface state after excitation. DFT calculations of the spin-resolved (red: Majority state, blue: Minority state) and spin-integrated (black) surface state from Ref. [Güt+16] are overlaid. (d) EDCs of the momentum-integrated surface state (energy-corrected for its dispersion, see text) at -0.2 ps and 70 ps (open circles) modeled by two Lorentzian profiles convolved with a Gaussian instrument response function (thick solid lines). The transient exchange splitting (Δ_{ex}), extracted from the distance between the two peaks (thin dashed lines: Majority spin state, thin dotted lines: Minority spin state), decreases after excitation. The blue dotted lines mark the region of interest used for extracting the exchange splitting. (e) Ultrafast dynamics of the exchange splitting (triangles). Error bars are confidence interval of exchange splitting extraction detailed in subsection 6.1.2. Solid lines describe the simulated magnetization dynamics by the M3TM (see Section 6.2) taking the probe depth of trARPES into account, scaled to the exchange splitting at 19 K (160 meV) [Güt+16]. Note that the second half of the time axis is log-scaled. Note that the figures are placed in clockwise order.

K, and reaches ∼160 meV at 19 K [Güt+16].

The trARPES intensity along the $\overline{\text{M}}$-$\overline{\text{X}}$ direction is shown in Fig. 6.2-b. Due to the limited energy resolution of our trARPES setup (150 meV), which is of similar magnitude as the exchange splitting, the exchange-split bands of the surface state are difficult to resolve and appear as a single dispersing band. The transient trARPES intensity along this cut was measured for various pump-probe delays. The pump-induced difference $\Delta I/I = [I\,(70ps) - I\,(-0.2ps)]/I_{max.}\,(-0.2ps)$ is shown in Fig. 6.2-c, and exhibits a narrowing of the surface state profile, consistent with a decrease of the exchange splitting.

Extracting the exchange splitting from the Si-derived surface state

The exchange-split surface state exhibits an approximately constant exchange splitting along the $\overline{\text{M}} - \overline{\text{X}}$ direction in the Brillouin zone (Fig. 6.3-a, left) [Güt+16]. In order to utilize the statistics

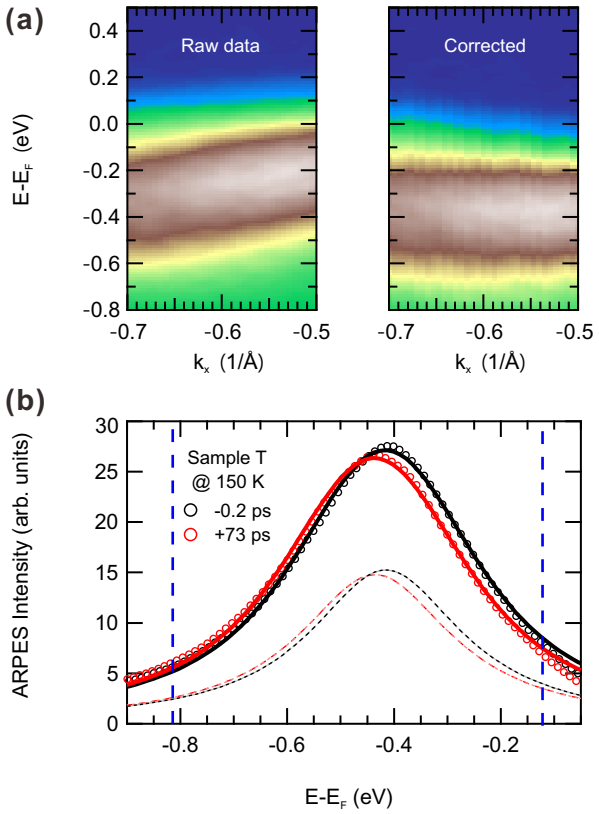

Figure 6.3: (a) The ARPES intensity before (left) and after (right) the energy correction of the dispersion of the surface state. (b) The modeling applied for extracting the exchange splitting from EDCs measured at 150 K, above T_N=107 K. The data are well described with a vanishing exchange splitting before (black) and after (red) pump excitation. The blue dotted lines mark the region of interest used for extracting the exchange splitting.

within the entire momentum range, we adopted a method to compensate for its energy dispersion. The energy distribution curves at each momentum have been shifted by the energy position of the surface state peak center, yielding a momentum-independent peak position (Fig. 6.3-a, right). These corrected surface state data were integrated along the momentum axis between -0.7 – -0.5 $Å^{-1}$ to yield the EDCs shown in Fig. 6.2-d and 6.3-b.

The exchange splitting has been extracted by fitting the dispersion-corrected, integrated EDC with two Lorentzian profiles representing the two spin-split surface states, convolved with a Gaussian accounting for the energy resolution (Fig. 6.2-d). Its width is determined from the EDC at T = 150 K (Fig. 6.3-b) where the exchange splitting vanishes [Güt+16]. The distance between the two Lorentzian peaks is defined to be the exchange splitting Δ_{ex}. While we find a pump-probe dependent Δ_{ex} below T_N (Fig. 6.2-d), data taken at T=150 K (above T_N) show a vanishing exchange splitting for all pump-probe delays within error bars (Fig. 6.3-b), confirming the viability of our analysis.

6.1.3 Exchange splitting dynamics

The exchange splitting dynamics at various fluences extracted from the above-mentioned procedure are shown in Fig. 6.2-e (triangles), and the exchange splitting before excitation is found in agreement with published results [Güt+16]. Similar to the dynamics of the normalized diffraction amplitude, the exchange splitting dynamics exhibits a two-step demagnetization (<1 ps and ∼10 ps [Win+20]), followed by a slow recovery after ∼100 ps.

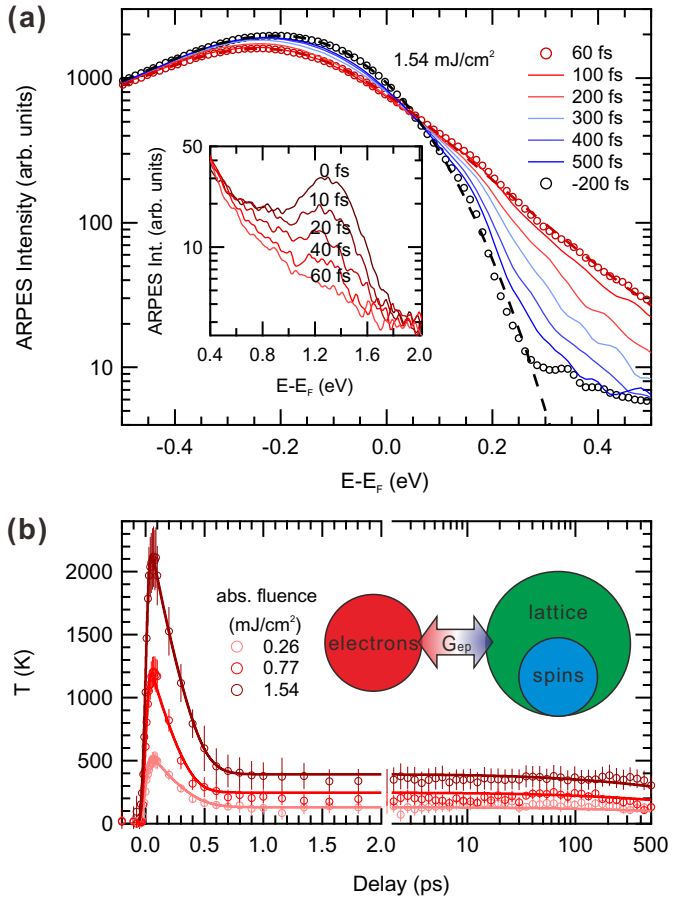

Figure 6.4: (a) EDCs integrated at the Fermi momentum (red dashed box in Fig. 6.2-b) for various pump-probe delays on a logarithmic intensity scale. Dashed lines are fits to a model function (see text) plotted for the EDCs at -200 fs and 60 fs. (Inset) Evolution of the transient trARPES intensity of an unoccupied state during the thermalization time of the system. (b) Ultrafast electronic temperature dynamics (circles). Solid lines show the electronic temperature dynamics by the 2TM (see Section 6.2) taking the probe depth of trARPES into account. The 2TM is schematically described by a diagram in the corner. Note that the second half of the time axis is log-scaled.

6.1.4 Electronic temperature dynamics

The electronic temperature is extracted from the transient trARPES intensity evolution integrated around the Fermi momentum k_F (red dashed lines in Fig. 6.2-b). Note that the Si-derived surface state has considerable amount of spectral weight across E_F, especially in the integration interval we chose to determine the electronic temperature. Fig. 6.4-a shows EDCs integrated at k_F for various pump-probe delays on a logarithmic intensity scale. The sharp drop-off at E_F is due to the Fermi-Dirac distribution function (Eq. (3.10), which encodes the transient electronic temperature. In order to quantify the change of the electronic temperature as function of delay, we have modeled the EDC by a phenomenological density-of-states function consisting of a Lorentzian profile and constant background multiplied with the Fermi-Dirac distribution function, and convolved with the instrumental response function. Fig. 6.4-a shows exemplary fits to the data at -200 fs and +60 fs, which describes the data very well especially the Fermi-edge region ($E\text{-}E_F \leq \pm 0.3$ eV), which is relevant for extracting the electronic temperature. At early times (<60 fs), there are some deviations at energies above $E\text{-}E_F > +0.3$ eV, originating from non-thermalized electrons right after excitation, which do not follow a Fermi-Dirac distribution. In particular, we also observe the transient occupation of an electronic state at +1.2 eV above E_F, which decays on a timescale of

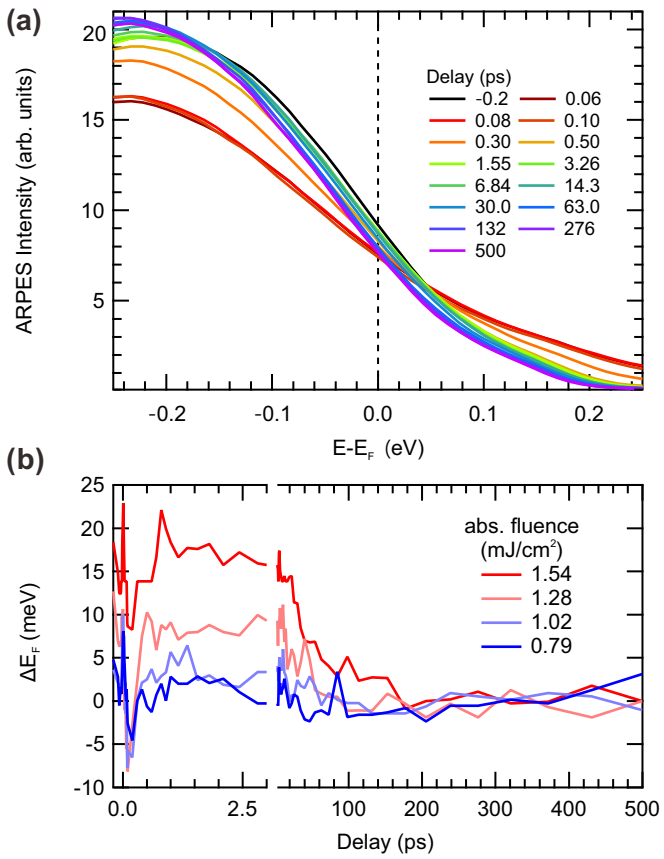

Figure 6.5: (a) EDC at the Fermi momentum used to extract the electronic temperature for selected pump-probe delays at 1.54 mJ/cm^2. (b) Temporal evolution of the space-charge induced energy shift. Note that the second half of the time axis is log-scaled.

~60 fs (see inset of Fig. 6.4-a). Subsequently, the system is thermalized and is well described by fits to the Fermi-Dirac function.

The extracted transient electronic temperatures at various pump fluences are shown in Fig. 6.4-b. At all pump fluences, the extracted effective electronic temperature steeply increases within the first 50 fs due to the absorption of the pump pulse energy, subsequently decreases within ~0.5 ps via redistribution of energy to the lattice governed by electron-phonon (e-ph) coupling, and finally slowly recovers to the starting temperature within several 100 ps by heat diffusion (Fig. 6.4-b).

At pump fluences larger than 1 mJ/cm^2, the EDCs are influenced by space charge effects [Olo+16] leading to a time-dependent shift of the Fermi energy. Therefore, a time-dependent correction of the Fermi energy has been applied (Figure 6.5). Upon strong pump excitation, pump-induced photoelectrons emitted from the sample lead to a broadening and energy shift of the photoelectron spectra due to space charge effects. Due to the varying distance of pump- and probe-induced electron clouds with pump-probe delays, the strength of this effect becomes time-dependent, with its strongest influence right after pump excitation, and a reduction within ~100 ps [Olo+16]. In order to account for this effect, we corrected this pump-induced space charge energy-shift in the EDCs by shifting E_F of the Fermi-Dirac distribution of the data shown in Fig. 6.5-a. The amount of time-dependent space charge shift (Fig. 6.5-b) is strongly fluence dependent due to the strongly non-linear photoemission from the pump pulse, and the timescale of its reduction matches literature reports [Olo+16] confirming the assignment to pump-induced space charge.

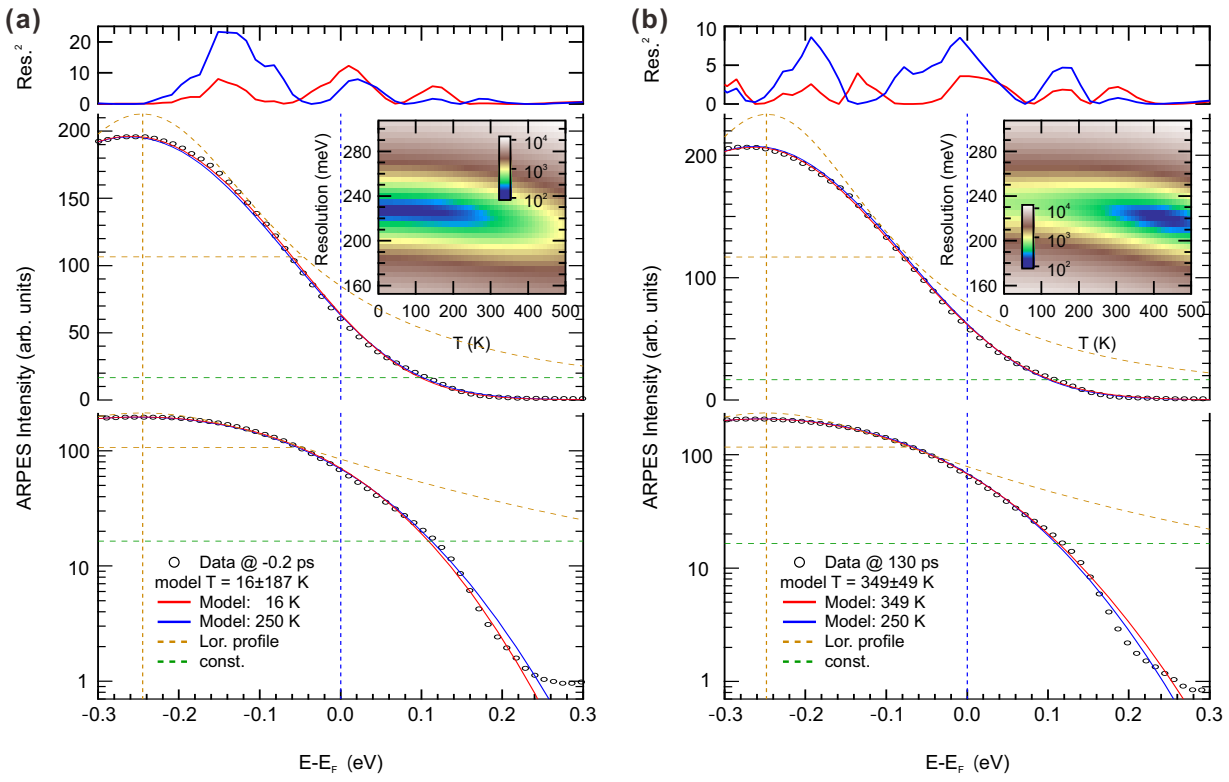

Figure 6.6: Energy distribution curves near the Fermi momentum at (a) -0.2 ps and (b) +130 ps shown on a linear- (middle) and logarithmic intensity scale (bottom). The phenomenological density of states function used to fit the data consisting of a Lorentzian peak (yellow) and a constant offset (green) are shown as dashed lines. Fit functions at the optimized electronic temperature and at 250 K are shown as red and blue solid lines, respectively. Energy-dependent squared residual highlighting the deviations between trARPES intensity and model fits is shown in the top panel. Insets: Color-coded χ^2 maps as a function of energy broadening and electronic temperature.

Accuracy of the electronic temperature determination

As will be discussed in subsection 6.2.1, our assignment of a remagnetization during a transient electron and lattice temperature exceeding the equilibrium Néel temperature requires a reliable determination of the electronic temperatures, in particular at late pump-probe delays. As our limited energy resolution poses a challenge to accurately extract low electronic temperatures (compare EDCs in Fig. 6.4-a), we investigated the accuracy of our analysis carefully. Fig. 6.6 shows the EDCs and fit functions based on the same phenomenological density of states at -0.2 ps and at +130 ps along with the energy-dependent squared residual curves indicating the difference between the model and the data. The employed phenomenological density of states function consists of a Lorentzian profile (yellow dotted lines) and a constant offset (green dotted lines), multiplied by the Fermi-Dirac distribution function, and convolved with a Gaussian resolution function of a full-width at half-maximum of 230 meV. The additional broadening compared to the intrinsic energy resolution given by the spectrometer and the probe pulse bandwidth can be explained by contamination of the surface, leading to a broadening of the surface state and Fermi level during the cause of the experiment. The pump space-charge-induced broadening on the spectra is in the range of the energy shift, and negligible compared to the energy resolution.

To check the sensitivity of our fit analysis, we compare fit functions at the optimized temperatures and at 250 K in Fig. 6.6. For the EDC before the photoexcitation, the higher electronic temperature (blue) yields a significant increase of the squared residual compared to the optimized temperature (16±187 K), yielding an upper limit for the electronic temperature (Fig. 6.6-a). For

γ_0 (J/K^{2}m^3)	247-760	T_D (K)	430
k$_e$ (W/m K)	0.5	G$_{ep}$ (J/K s m^3)	(8.5-13)$\times 10^{17}$
T_N (K)	130-340 (ex. split) 265-600 (001 amp.)	R (1/ps)	0.074 (ex. split) 0.055 (001 amp.)
E$_{ex}$/T_N (eV/K)	0.002	μ_{at} (μ_B)	7.55

Table 6.1: Physical parameters of $GdRh_2Si_2$ for the 2TM and the M3TM.

the EDC at late times, where the magnetic order starts recovering, the situation is opposite, and the fit with optimized temperature (349±49 K) describes the data significantly better than the 250 K case (Fig. 6.6-b), providing a lower limit for the electronic temperature.

To further assess the influence of the resolution function in the model, we calculated χ^2 map as a function of the energy resolution and the electronic temperature parameters shown in the insets of Fig. 6.6-a/b. The χ^2 map before photoexcitation shows an extended minimum at the determined energy resolution of 230 meV extending until ∼200 K, confirming the error assignment based on the nonlinear fit parameters. After e-ph equilibration we find a slight correlation of the electronic temperature and resolution parameter, but can still clearly identify a minimum around the optimized temperature within ±50 K, and with a consistent resolution function. Note also, that a reduced resolution at late times, as could be expected from reduced space charge influence, would lead to a further increase of extracted electronic temperatures, and that any description with $T_e < T_N$ yields a significantly worse χ^2.

6.2 Analysis and Discussion

Our experimental data consist of the ultrafast dynamics of the electronic temperature, the exchange splitting, and the normalized (001) magnetic diffraction amplitude upon 1.55 eV pump excitation. The exchange splitting and the diffraction amplitude dynamics exhibit a very similar two-step demagnetization (<1 ps, ∼10 ps) and subsequent recovery after ∼100 ps, suggestive of a common physical origin. The electronic temperature also exhibit dynamics on similar timescales. In order to consistently describe our experimental results, we modeled the transient electronic temperature and demagnetization dynamics using an M3TM based on the LLB equation (Eqs (2.20), (2.21), (2.22)), modified to account for AF angular momentum exchange introduced in section 2.2 [AHN16; AC11; JA22b; JA22a; Win+22]. Simulated time evolutions of T_e, T_p and m at selected absorbed pump fluences are overlaid on the experimental results (Fig. 6.2-a/e, 6.4-b, and 6.7-a/b, 6.8-a). For determining the model parameters, at a given fluence, first a numerical solution of two-temperature model (Eqs. (2.20) and (2.21)) is fit to the electronic temperature dynamics (Fig. 6.4-b), and subsequently a numerical solution of magnetization (Eq. (2.22)) is fit to the magnetization dynamics of both, the (001) magnetic diffraction amplitude, and the surface state exchange splitting (Fig. 6.2). The physical parameter ranges used for the simulation are listed in Table 6.1. While the model can describe the qualitative evolution of the curves very well, we found that for a quantitative description of the fluence dependent results, we need to vary a number of model parameters significantly. In this section we will discuss the M3TM simulation results, and the fluence dependence of the extracted parameters. First, we will compare the dynamics at a given fluence, and then discuss the fluence dependence of the results.

6.2.1 Comparison of electronic temperature and magnetization dynamics

Fig. 6.7-a/b shows the ultrafast dynamics of the electronic temperature dynamics together with the dynamics of the normalized magnetic order parameter of both itinerant (surface state exchange splitting) and localized (trRXD amplitude) magnetic moments within the first two ps (Fig. 6.7-a), and on a longer timescale (Fig. 6.7-b) for an absorbed fluence of 1 mJ/cm^2. The electronic

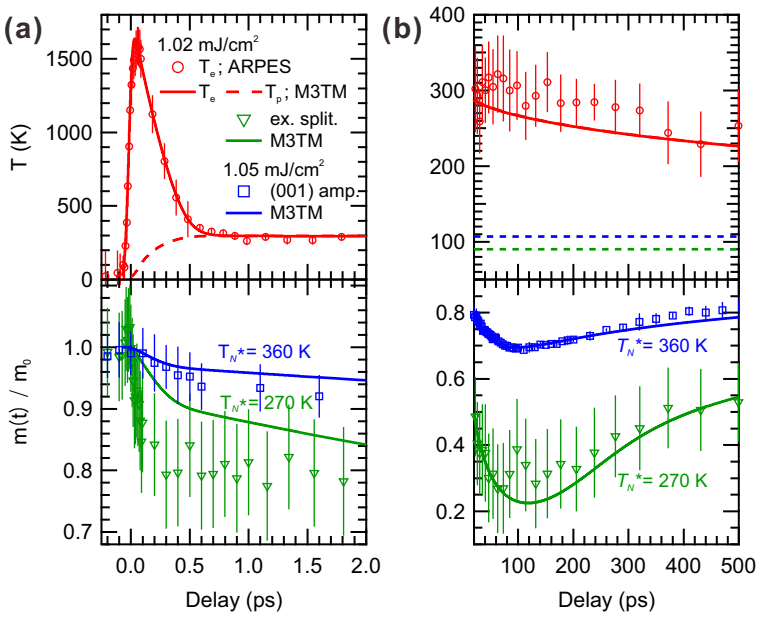

Figure 6.7: (a) Short-term and (b) long-term dynamics of the electronic temperature (red circles), the normalized exchange splitting (green triangles) and the (001) diffraction amplitude (blue squares). Red solid (dashed) lines are electronic (lattice) temperature dynamics simulated by the M3TM. Blue and green solid lines show the simulated magnetization dynamics taking the probe depth of trRXD and trARPES into account, respectively. Dashed lines in (b) indicate the reference sample T_N (blue: bulk AF order [Win+20]; green: exchange splitting [Güt+16]).

temperature is very well described by the M3TM (red curves in Fig. 6.7-a/b), and yields an e-ph coupling constant of G_{ep} = (8.5 – 13)×10^{17} J K^{-1} s^{-1} m^{-3}. The electronic temperature rapidly increases within the pump pulse duration followed by e-ph relaxation within ∼0.5 ps, which equilibrates the electronic and lattice temperatures and leads to a transient increase of the lattice temperature by several 100 K at this fluence (dashed line in Fig. 6.7-a). Subsequently, the electron and lattice temperatures relax via heat diffusion within several 100 ps (Fig. 6.7-b). Remarkably, the electron and lattice temperatures remain significantly above the equilibrium surface (T_N = 90 K [Güt+16] exchange splitting) and bulk (T_N = 107 K [KK15; Win+20] magnetic diffraction amplitude) Néel temperatures for the entire investigated time range (dashed lines in Fig. 6.7-b, top).

Based on this description of the electronic and the lattice temperature, the dynamics of bulk and surface magnetic order are simulated. Similar to other rare-earth magnets, the M3TM features an enhanced demagnetization rate during the first ∼0.5 ps, corresponding to an enhanced spin-flip scattering rate due to the large transient temperature difference between electrons and lattice [AC11]. After temperature equilibration, the demagnetization timescale slows down to ∼10 ps (Fig. 6.7-b). According to Eq. (2.22) of the M3TM, a recovery of magnetization is expected once the transient electron and lattice temperatures drop below the magnetic transition temperature. Remarkably, while the experimental magnetic order starts recovering at ∼100 ps in Fig. 6.7-b, the electron and lattice temperatures stay well above the equilibrium bulk and surface Néel temperatures (dashed lines in Fig. 6.7-b, top). This indicates a transiently enhanced magnetic ordering temperature, which was accounted for in the model by introducing an effective transient T_N^* = 130 – 340 K (surface state exchange splitting) and 265 – 600 K (trRXD amplitude).

While the overall behavior is well described by this model for both observables, in particular for the ∼10 ps timescale, a quantitative description requires a ∼33 % larger value for the material-specific R factor for the surface magnetic order (see Table 6.1). A possible explanation might be an underestimation of the probe penetration depth of trRXD.

Both, the itinerant surface electrons and the localized bulk $4f$ moments exhibit a very similar magnetic order dynamics, described by similar microscopic physical parameters. Such a similarity of the magnetic order dynamics of the localized $4f$ moments and the itinerant conduction electrons has been previously considered for determining the strength of the exchange coupling between the $4f$ moments and conduction electrons in lanthanide-based magnets [Fri+20; Fri+15; Ret+16]. Based on such considerations, our results indicate a strong exchange coupling between the itinerant conduction electrons and the localized Gd $4f$ moments in AF $GdRh_2Si_2$.

The resemblance of the magnetic order dynamics of the itinerant surface electrons and the localized bulk $4f$ moments allows for another interesting interpretation. Unlike the similar collinear antiferromagnet $EuRh_2Si_2$, where the surface state actively enhances the sub-surface in-plane FM ordering, leading to exchange splitting at significantly higher temperatures (41 K) than the bulk T_N of $\sim$ 24.5 K [Gen+17; Güt+19], $GdRh_2Si_2$ exhibits surface ordering at slightly lower temperatures (90 K) than the bulk ($T_N \sim 107$ K). Considering these facts, the resemblance of the two magnetic order dynamics implies that the surface state exchange splitting in $GdRh_2Si_2$ acts as a spectator of the sub-surface FM ordering, supporting our assignment that its dynamics can be regarded as a fingerprint of the itinerant sub-surface magnetic order.

The M3TM considers spin-flip scattering events both from Elliott-Yafet type with phonons, leading to angular momentum transfer to the lattice, as well as direct spin transfer between opposing AF sublattices [JA22b]. The latter channel was demonstrated to contribute as an efficient demagnetization channel in $GdRh_2Si_2$ using trRXD and ab-initio calculations in particular for the slow demagnetization channel in Chapter 4 [Win+22]. Therefore, we conclude that the reduction of both, the surface state exchange splitting and the $4f$ AF ordering, results from a combination of spin-flip scattering induced by direct spin transfer and phonon-mediated processes. This interpretation is also quantitatively supported considering the spin-flip scattering probability a_{sf}, which can be calculated from the material-specific R factor. For AF $GdRh_2Si_2$, a_{sf} is 25 to 43 % depending on the pump fluence. With the equilibrium $T_N = 107$ K, this is two to three times larger than FM Gd (15 %), where only a phonon-mediated process occurs [Koo+10].

While the model describes the experimental results qualitatively well, the model significantly underestimates the amplitude of the fast $\sim$0.5 ps demagnetization channel (Fig. 6.7-a). This is particularly evident in the exchange splitting dynamics, which exhibits a >10% drop within the first 100 fs significantly exceeding the $\sim$5% reduction in the M3TM simulations within this timescale. This could indicate an important influence of a non-thermal electron system during the first $\sim$100 fs (see Fig. 6.4-a), which is neglected in the model. Such a non-thermal electron distribution could lead to more efficient spin-flip scattering due to the occupation of highly excited electronic states.

6.2.2 Fluence dependence of the ultrafast spin dynamics

As discussed in the previous section, for a quantitative description of the ultrafast magnetic order dynamics, we have to consider a transiently enhanced transition temperature T_N^*. Here, we discuss the fluence dependence of this behavior. To emphasize the inability of the M3TM to account for the magnetization dynamics using the equilibrium T_N, Fig. 6.8-a shows the trRXD amplitude at a pump fluence of 1.40 mJ/cm^2. Employing the equilibrium T_N=107 K yields a simulated magnetization dynamics exhibiting a complete demagnetization within $\sim$3 ps, which does not recover even after 1 ns. However, considering a transient T_N^*=380 K correctly reproduces the experimental magnetic order dynamics with $\sim$50% demagnetization and recovery after $\sim$100 ps. Importantly, both model descriptions employ the same electronic and lattice dynamics, consistent with the experimentally measured electronic temperature (see Fig. 6.4-b). Fig. 6.8-b and c show the fluence dependence of the minimal normalized magnetic order parameter of the magnetic diffraction amplitude and the exchange splitting, respectively, compared to the M3TM simulations for various T_N. Similarly, we find that the M3TM using the equilibrium Néel temperatures cannot reproduce the experimental data. Surprisingly, even employing an enhanced critical temperature T_N^* only yields a correct description of the demagnetization dynamics within a narrow fluence range, and we

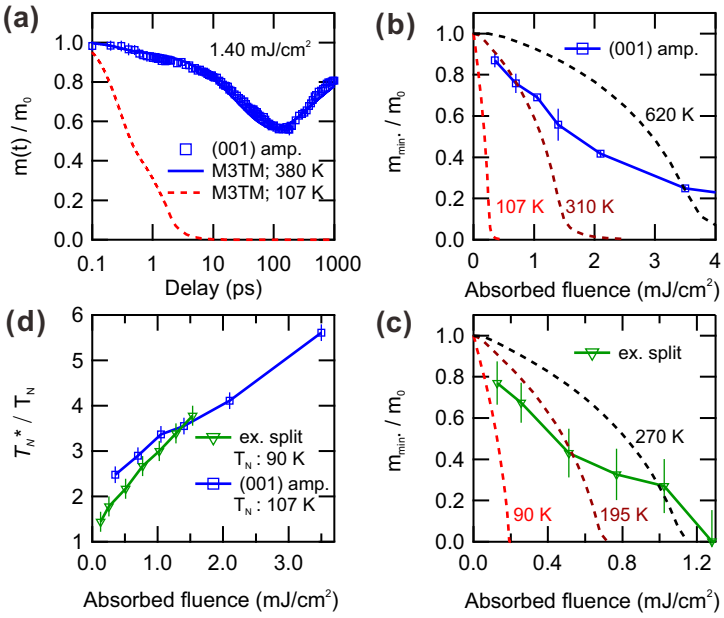

Figure 6.8: (a) Time-dependent magnetic diffraction amplitude dynamics (blue squares) shown together with the magnetization dynamics calculated by the M3TM for two different Néel temperatures (T_N=107 K, red dashed line, T_N^*=380K, blue solid line). Note the time axis is log-scaled. (b, c) Fluence dependence of the minimal magnetic order parameter of the magnetic diffraction amplitude (b) and normalized exchange splitting (c). Dashed lines show the predictions of the M3TM for various Néel temperatures (red lines: equilibrium T_N) (d) Fluence dependence of the transient enhancement of T_N^*/T_N of the diffraction amplitude (blue) and the exchange splitting (green). Note the figures are placed in clockwise order.

find that the transient T_N^* scales with the pump fluence, shown in Fig. 6.8-d. In other words, no single T_N^* reproduces the entire experimental fluence dependence in the M3TM. Importantly, the transient Néel temperature enhancement is consistent between the trRXD data and the exchange splitting, and the electronic and lattice temperatures after e-ph equilibration following the expected fluence dependence (Figure 6.9-a). While we want to emphasize that this transient increase of T_N is introduced as one possible phenomenological description of the experimental results within the scope of the M3TM, it may be rationalized by the observed remagnetization at transient electron/lattice temperatures exceeding the equilibrium Néel temperature. The influence of other model parameters is discussed in subsection 2.2.2, more specifically in Figure 2.5.

Similar robust magnetic order phenomena were previously reported for other lanthanides, however without a systematic analysis. Refs. [And+15] and [ALW21] reported that the exchange splitting of the 5*d* surface state of FM Gd and Tb starts recovering already for an electronic temperature still above the equilibrium Curie temperature. Furthermore, Ref. [Thi+17] although not directly providing a transient temperature dynamics, concluded that photoexcitation strong enough to heat the sample above the transition temperature does not lead to a complete suppression of magnetic order in FM and AF Dy.

The fluence dependence of the minimal magnetization amplitude found in the M3TM exhibits a convex behavior, i.e. it resembles the equilibrium order parameter, with fluence acting as temperature (dashed curves in Fig. 6.8-b/c). This can be understood from basic assumptions of the M3TM, that the magnetic system is not very far from thermal equilibrium. This means that the non-equilibrium magnetization is described by a thermal distribution in a non-equilibrium field, leading to magnetization dynamics governed by the equilibrium properties of the system. In contrast, the experimental data exhibit a more gradual linear to concave behavior. This behavior could indicate the importance of non-thermal spin dynamics or a transient modification of the exchange

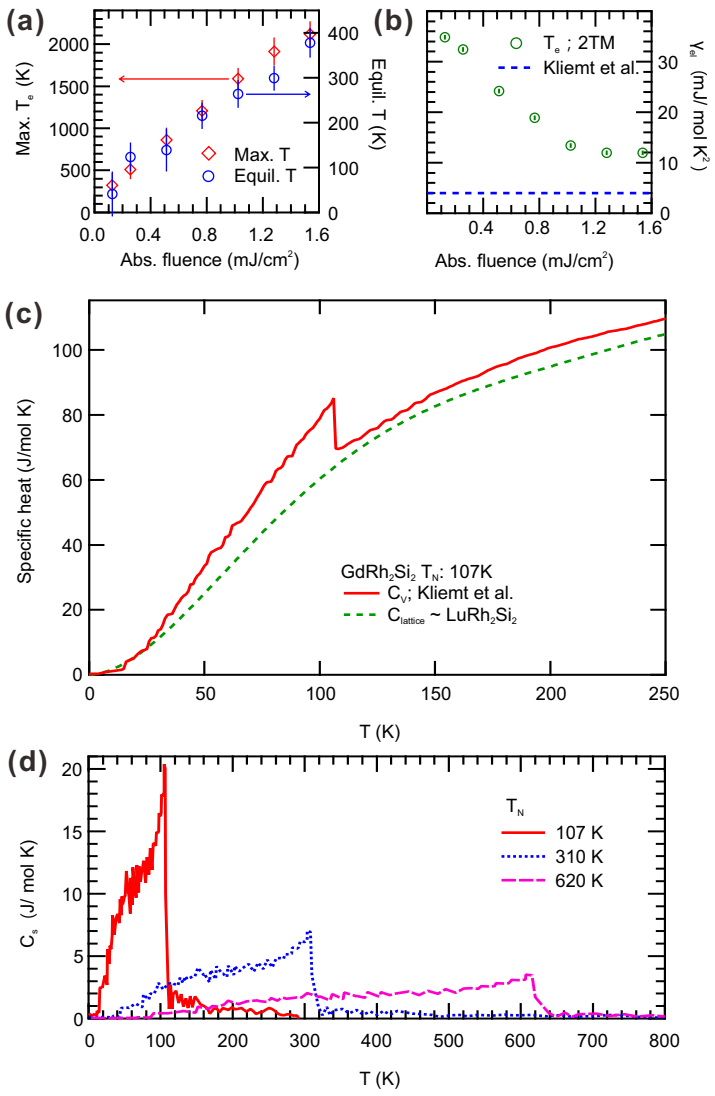

Figure 6.9: Fluence dependence of (a) the maximum electronic temperature, the equilibrated electronic temperature and (b) the Sommerfeld coefficient, $\gamma_0 (= C_e/T_e)$. (c) Temperature dependence of the specific heat of $GdRh_2Si_2$[KK15] and the modeled lattice heat capacity (see text). (d) Spin heat capacities of AF $GdRh_2Si_2$ scaled to various Néel temperatures used for the M3TM simulations described in the main text.

interaction in the excited system, which go beyond the currently available M3TMs. Therefore, even though such models can *qualitatively* well describe experimental ultrafast magnetic order dynamics [Koo+10; Shi+20; Atx+14; Che+19; Fri+20; Sul+12; Rad+11; Fri+15; Atx+10; Nie+14] our results indicate that *quantitative* comparison needs to be met with caution. This is particularly important if not all experimental parameters, such as the electron and/or lattice temperature evolution are accessible under similar conditions as the magnetization dynamics. Our data can serve as a test case for more microscopic descriptions such as atomistic spin models [Zah+21; Zah+22] or time-dependent density functional theory [Kri+15; Gol+21] that go beyond a mean-field description and can potentially include such effects.

Fluence-dependence of the electronic, spin, and lattice heat capacities

In order to describe the experimental results measured at various pump fluences with the M3TM, parameters related to the heat capacity of $GdRh_2Si_2$ had to be adjusted as Table 6.1 implies. This subsection discusses the fluence dependence of the spin and electron heat capacities.

The maximum electronic temperature of the M3TM is largely determined by the Sommerfeld coefficient $\gamma_0 = C_e/T_e$. While the M3TM with a constant γ_0 yields a square-root-like dependence of maximal electronic temperature with fluence, experimentally we find an approximately linear behavior (Fig. 6.9-a). A consistent description of this behavior requires a fluence-dependent Sommerfeld coefficient, as shown in Fig. 6.9-b. Surprisingly, all values for γ_0 that we find significantly exceed the low temperature equilibrium value reported in Ref. [KK15], and also depends on the fluence (Fig. 6.9-b). A similar enhancement of γ_0 necessary for describing the ultrafast electronic temperature dynamics was recently also reported for FM Ni [Ten+18]. A possible reason could be a varying electronic density of states away from the Fermi energy [LJ22]. Additionally, we account for the magnetic specific heat exclusively in the lattice system, and neglect possible contributions of itinerant magnetic specific heat to the electronic specific heat. Such an explanation would also fit to the observed fluence dependence, as the influence of the spin-induced heat capacity becomes exceedingly small compared to the electronic heat capacity as fluence and electronic temperatures increase. Please note that this description still yields a consistent modeling of the electronic and lattice temperatures, and that equilibrated electron/lattice temperatures are well-described with the modeled lattice heat capacity (Fig. 6.9-a), which is a hybridization of a polynomial approximation of $LuRh_2Si_2$ specific heat ($T < 0.67\ T_D$) and the Einstein model of the lattice heat capacity of $T_D = 430$ K ($T > 0.67\ T_D$) (Fig. 6.9-c).

Magnetic specific heat contributions in the M3TM were extracted from the difference of isostructural, paramagnetic $LuRh_2Si_2$ and AF $GdRh_2Si_2$ (Fig. 6.9-c). For consistent M3TM simulations, the spin heat capacity was scaled to the transient Néel temperature (see Fig. 6.9-d) and considered as part of the lattice heat capacity. Please note that M3TM simulations of the electron and lattice temperatures do hardly depend on T_N^* (Figure 2.5-i), and that this correction only marginally influences the exact values of fitting parameters.

6.3 Conclusion

In this study, employing time- and angle-resolved photoelectron spectroscopy and time-resolved resonant elastic soft x-ray diffraction, we explored the femtosecond dynamics of the electronic temperature, the exchange splitting of a Si-derived surface state, and the resonant magnetic diffraction amplitude of the (001) magnetic reflection in antiferromagnetic $GdRh_2Si_2$. Combining experimental techniques sensitive to in-plane surface ferromagnetic order and out-of-plane bulk antiferromagnetic order allows us to gain a multi-faceted view on the ultrafast dynamics of magnetic order of a quasi-2D antiferromagnet. The similar dynamics of the two observables suggests a strong exchange coupling between itinerant conduction electrons, and localized Gd $4f$ moments. We found similar dynamics of the exchange splitting and the diffraction amplitude, which can be *qualitatively* well described by a magnetic three-temperature model (M3TM) based on the Landau-Lifshitz-Bloch equation. Surprisingly, we found a recovery of the transient magnetic order already for electronic and lattice temperatures exceeding the equilibrium transition temperatures. This implies a transiently enhanced T_N^*, which allows us to quantitatively describe the magnetic order dynamics within the M3TM. Comparison with the mean-field behavior predicted by the M3TM suggests that the system transiently strongly deviates from a mean-field behavior. These deviations, which could be due to non-thermal effects in the spin system or a transient modification of the exchange interaction, are found to scale with increasing excitation fluence. Our results thus imply that models beyond a M3TM descriptions are necessary to quantitatively describe the ultrafast magnetic order dynamics.

This page is intentionally left blank.

Chapter 7

Disparate dynamics of exchange coupling and magnetic order in a frustrated $4f$ antiferromagnet

$GdCo_2Si_2$ is very unconventional antiferromagnet compared to other family members of AF $Ln\,T_2Si_2$: As discussed in Chapter 5, $GdCo_2Si_2$ exhibits incommensurate magnetic diffraction [0 0 L] peaks at L=0.965 and 1.035 at 20 K, and the peak position L evolves upon heating (Figures 5.4-b, 5.6). Moreover, while other materials exhibits mean-field-like demagnetization (Figures 2.2), $GdCo_2Si_2$ does not (Figure 5.4-c). However, though $GdCo_2Si_2$ exhibits such interesting antiferromagnetism compared to other AF $Ln\,T_2Si_2$ compounds, it has not drawn much attention so far. For example, even its exact AF spin structure is not yet identified. There was one attempt employing nuclear magnetic resonance spectroscopy of Co ions suggesting an AF structure repeating every two unit cells [Fig+89]. However, it it were true, $GdCo_2Si_2$ must have exhibited [0 0 0.5] magnetic diffraction peaks, not incommensurate peaks. Therefore, to establish basic understanding of AF $GdCo_2Si_2$ and to understand why it exhibits such exotic antiferromagnetism, in this chapter, we will study AF $GdCo_2Si_2$ in detail employing (tr)RXD. First, we will try to identify the spin structure of $GdCo_2Si_2$ by comparing experimental magnetic diffraction intensities with structure factor calculations. Then, we will discuss how these incommensurate spin order evolves upon ultrashort optical excitation.

7.1 Sample characterization

7.1.1 Photon-energy dependence

Since we studied two incommensurate magnetic diffraction peaks of $GdCo_2Si_2$, to check whether the resonance effect of the two peaks are identical, we studied the spectral behavior of the incommensurate diffraction peaks at various incident photon energies around Gd M_4 and M_5 absorption edges. Since the peak position of the two peaks shift significantly, from now on, we will label the peaks at L=0.966 and 1.034 as [0 0 q] and [0 0 $2-q$], respectively. As Figure 7.1-a shows, both peaks exhibit almost identical energy dependence. For quantitative comparison, we phenomenologically modelled the peaks with Doniach-Sujic function (Eq. 5.1) and extracted the resonant behavior (solid triangles) and the penetration depth (open circles) as shown in Figure 7.1-b. Resonant enhancement of the signal is the most prominent at 1188 eV. Simultaneously, the penetration depth is the smallest at 1188 eV ($\sim$4 nm). Therefore, 1188 eV is chosen for the main working incident photon energy. The data presented in this chapter were all measured at 1188 eV, unless specified.

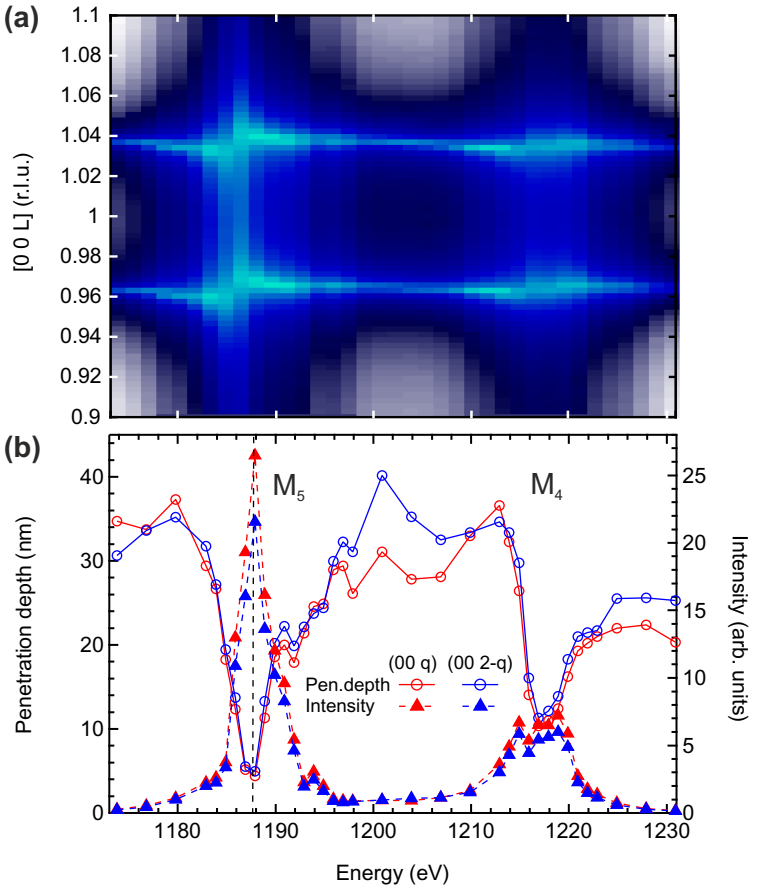

Figure 7.1: (a) $\theta - 2\theta$ scans along [0 0 L] at various incident photon energy of $GdCo_2Si_2$. From bright blue to dark blue, intensity decreases taking white color as background. (b) Photon-energy-dependence of penetration depth (open circles; left axis) and diffraction intensity (solid triangles; right axis) of magnetic [0 0 q] (red markers; $L < 1$) and [0 0 $2-q$] (blue markers; $L > 1$) reflections.

7.1.2 Equilibrium demagnetization

To characterize the magnetic properties of the sample, first, we measured temperature dependent behavior of the magnetic diffraction peak upon equilibrium heating employing resonant magnetic soft x-ray diffraction. The incommensurate magnetic diffraction of [0 0 q] and [0 0 $2-q$] reflections vanish at 45 K, where $q \sim 0.966$ at 10 K. The diffraction peaks evolve in two different aspects upon equilibrium heating (Fig. 7.2-a). First, the diffraction intensity decreases. Note that from now on, intensity indicates integrated area of the diffraction peak unless specified. Both peaks exhibit almost identical temperature dependence of the integrated intensity (Fig. 7.2-b). Comparing with the mean-field-like behavior of equilibrium demagnetization of S=7/2 (∼Gd) case, the intensity quenching behavior significantly deviates from the mean-field-like behavior. In other words, in $GdCo_2Si_2$, thermal excitation overcomes the Weiss molecular field much more efficiently than the mean-field-like expectation. Second, the position of the diffraction peaks shifts. Both the [0 0 q] and the [0 0 $2-q$] peak monotonously shift in the direction of decreasing q with respect to the center of the two peaks, and the amount of the shift is identical, $\Delta q \sim$ -0.008 (Fig. 7.2-c). Since the peak position number is inversely proportional to the period of the long-range AF order, decreasing q indicates increase of period of long-range Gd $4f$ AF order upon heating.

One notable thing is that the center of the two peaks shifts as temperature increases (Inset of Fig. 7.2-c). The presented [0 0 L] value is calculated from the diffraction intensity acquisition program (SPEC) based on the diffraction geometry between the incoming and outgoing x-ray lights

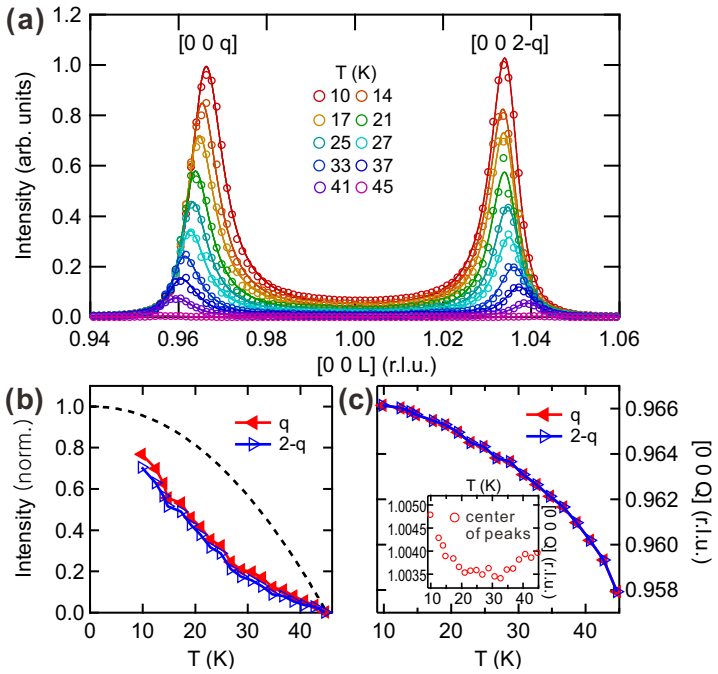

Figure 7.2: (a) The [0 0 q], [0 0 2 − q] magnetic diffraction peaks at various sample temperatures. Solid curves are phenomenological description of the experimental data modeled by Doniach-Sunjic function (see Eq. (5.1)). (b) Temperature dependent evolution of (b) the diffraction intensity and (c) the peak position of the [0 0 q], [0 0 2 − q] reflections. The black dashed line in (b) is the square of the mean-field-like behavior of the magnetization for S = 7/2 (∼Gd).

and the sample based on the assumption that the lattice constant c of $GdCo_2Si_2$ is constant 9.81 Å [Czj+89] at all temperatures. However, the center of the two peaks shifts as temperature increases. We think that the center of the two peaks is an actual position of [001]. The deviation from [001] position may come from two different factors: First, the actual lattice constant c of $GdCo_2Si_2$ is different from 9.81 Å, which can explain that why the center position is at 1.0048, not 1. If $L = 1.0048$ is the correct position of [001], the lattice constant c becomes 9.763 Å, 0.05 Å smaller than the literature value. Second, the lattice constant c evolves from heating. From 10 K to 20 K, the center shifts from 1.0048 to 1.0035. This suggests thermal expansion of c from 9.763 Å to 9.775 Å ($\Delta c = 0.012$ Å). While other family compounds do exhibit thermal expansion of lattice constants [Szy+86], the amount is not significant enough to yield a visible peak shift in RXD measurements. Though, we don't understand exact reason for this, for future studies, we note this observation here.

7.1.3 Identification of the spin structure

Unlike other LnT_2Si_2 compounds, $GdCo_2Si_2$ has incommensurate spin order. Ref. [Win+20] has shown that we can identify unknown spin structure of a similar antiferromagnet $GdRh_2Si_2$ by measuring the magnetic diffraction intensity at various azimuthal orientations with two linearly polarized x-ray lights (σ, π). In order to identify the exact antiferromagnetic spin structure of $GdCo_2Si_2$, we measured the magnetic diffraction peaks at various azimuthal orientations with two linear polarizations of the incident light.

As Figure 7.3-a shows, the ratio of the diffraction intensity between σ and π polarizations is almost constant at around 0.4 at all the in-plane orientations of $GdCo_2Si_2$ within 180°. The next step is to postulate a possible spin structure and to simulate the azimuthal dependence of the I_σ/I_π ratio from structure factor calculation. Since the diffraction peak appears at $q = 0.966$=483/500 at 10 K, one candidate is that the spin structure is a helimagnet repeating 483 rotations every 500

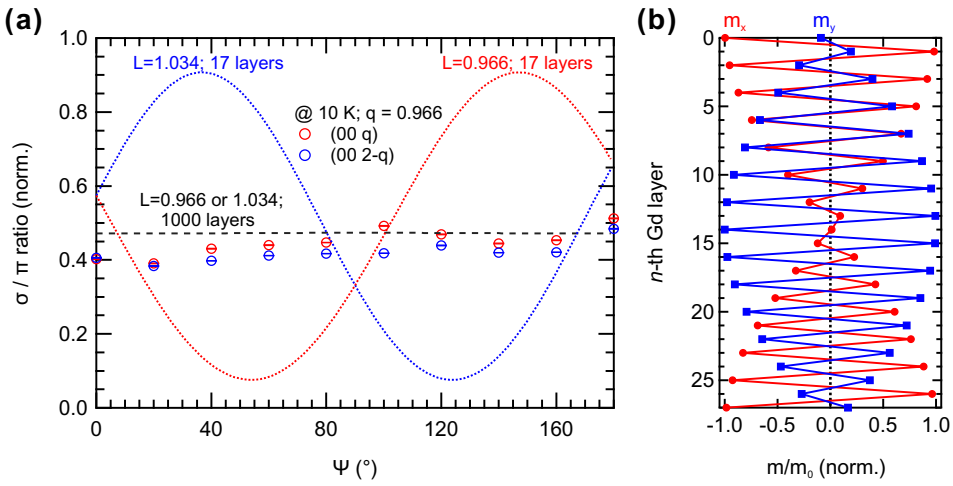

Figure 7.3: (a) The ratio between diffraction intensity at σ and π polarizations measured at various azimuthal orientations of the sample. Structure factor calculations with a helimagnetic spin structure with L=0.966 (red dotted line; summed up for 17 layers) and 1.034 (blue dotted line; summed up for 17 layers) are plotted together (see text). Black dashed line is the prediction summed up for 1000 layers. (b) In-plane components of the magnetic moments forming a helimagnetic structure suggested in Eqs. (7.1),(7.2),(7.3) as one candidate for AF structure of $GdCo_2Si_2$. Since there is no out-of-plane component, $m_z = 0$. Though period of the structure is 500 unit cells, only 27 layers from the surface are presented.

unit cells along the c-axis. The postulated long-range helimagnet has following structure in the Cartesian coordinate:

$$(m_x)_n = m\cos\left(\frac{483}{500}n\pi\right), \tag{7.1}$$

$$(m_y)_n = m\sin\left(\frac{483}{500}n\pi\right), \tag{7.2}$$

$$(m_z)_n = 0, \tag{7.3}$$

where m is Gd $4f$ moment, and the subscript n indicates the n-th Gd layers in $GdCo_2Si_2$ along the c-axis (Figure 7.3-b). Based on this postulate, we calculated the structure factor for the two linearly polarized incident lights, σ, π. Since the diffraction intensity is resonantly amplified, we only calculate the contribution from the dipole-dipole interaction (E1-E1), which has a linear scaling relation with magnetic moment $\vec{m}$: $(\hat{\epsilon}' \times \hat{\epsilon}) \cdot \vec{m}$, where $\hat{\epsilon}$, $\hat{\epsilon}'$ are the polarization of incident and scattered lights. A scattering matrix for linear polarizations looks as following [HM96]:

$$\left(\hat{\epsilon}' \times \hat{\epsilon}\right) \cdot \vec{m}_i = \begin{pmatrix} \hat{\epsilon}'_\sigma \times \hat{\epsilon}_\sigma & \hat{\epsilon}'_\sigma \times \hat{\epsilon}_\pi \\ \hat{\epsilon}'_\pi \times \hat{\epsilon}_\sigma & \hat{\epsilon}'_\pi \times \hat{\epsilon}_\pi \end{pmatrix} \cdot \vec{m}_i = \begin{pmatrix} 0 & (m_z)_i \sin\theta + (m_x)_i \cos\theta \\ (m_z)_i \sin\theta - (m_x)_i \cos\theta & -(m_y)_i \sin 2\theta \end{pmatrix}, \tag{7.4}$$

where $\theta = 31.9°$ is the Bragg angle of the diffraction geometry. Summing up the scattering factor of 1000 contributing magnetic moments in 500 unit cells, we simulate diffraction intensity at σ and π polarizations and the I_σ/I_π intensity ratio. Since the detector does not distinguish the polarization of scattered light, it can be expressed as following:

$$I_\sigma = \left|\sum_i^{1000} \left(\hat{\epsilon}'_\pi \times \hat{\epsilon}_\sigma\right) \cdot \vec{m}_i e^{2\pi i \vec{Q}\cdot\vec{r}_i}\right|^2 \tag{7.5}$$

$$I_\pi = \left|\sum_i^{1000} \left(\hat{\epsilon}'_\sigma \times \hat{\epsilon}_\pi\right) \cdot \vec{m}_i e^{2\pi i \vec{Q}\cdot\vec{r}_i}\right|^2 + \left|\sum_i^{1000} \left(\hat{\epsilon}'_\pi \times \hat{\epsilon}_\pi\right) \cdot \vec{m}_i e^{2\pi i \vec{Q}\cdot\vec{r}_i}\right|^2. \tag{7.6}$$

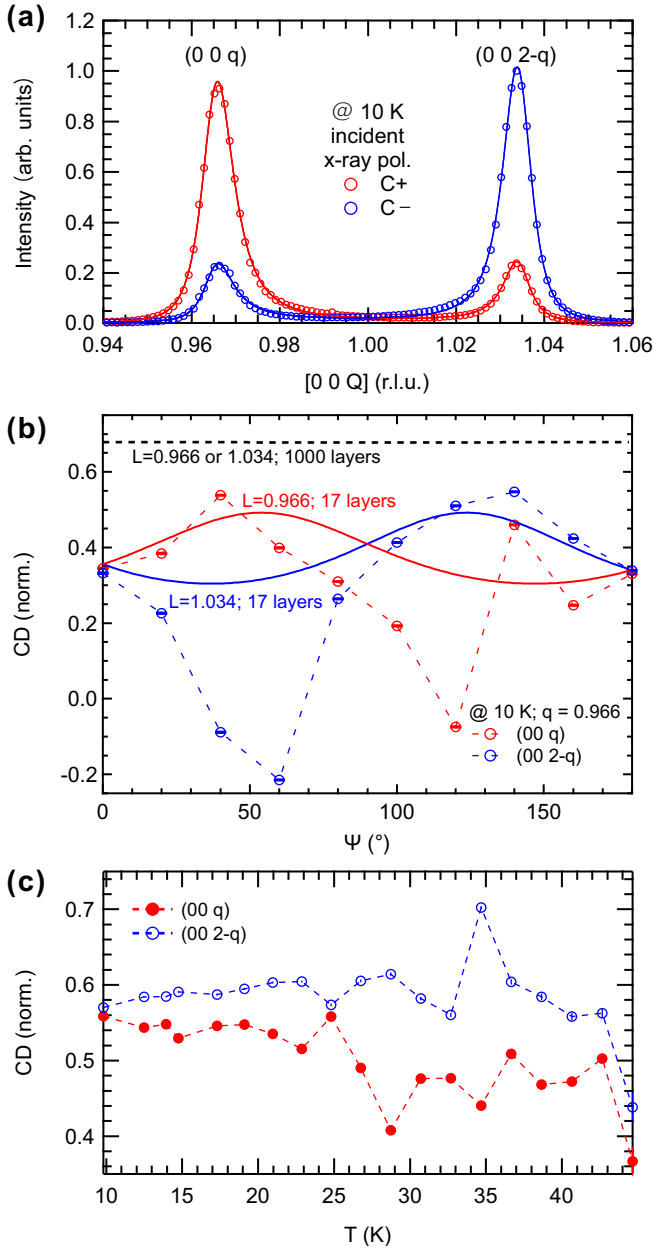

Figure 7.4: (a) Magnetic diffraction intensity of $[0\ 0\ q]$ and $[0\ 0\ 2-q]$ reflections measured with circularly polarized incident soft x-ray light. (b) Circular dichroism measured at various azimuthal orientations of the sample. Model predictions with a helimagnetic spin structure with L=0.966 (red solid line; summed up for 17 layers) and 1.034 (blue solid line; summed up for 17 layers) are plotted together (see text). Black dashed line is the prediction summed up for 1000 layers. (c) Circular dichroism of $GdCo_2Si_2$ at various sample temperatures.

The structure factor calculation of a single domain is presented as a black dashed line in Figure 7.3-a. Similar to experimental result, it expects a constant ratio at all azimuthal orientations. This is natural considering the isotropic nature of the suggested helimagnetic structure. From this excellent agreement, we tentatively assume that the spin structure of AF $GdCo_2Si_2$ is a long-range helimagnet along the c-axis repeating 483 rotations every 500 unit cells since each unit cell has two Gd $4f$ moments.

7.1.4 Circular dichroism

Interestingly enough, the magnetic diffraction peaks of $GdCo_2Si_2$ exhibits circular dichroism (CD), unlike other family compounds (Figure 7.4-a). The circular dichroism in this material has not been reported yet. Since, in general, [0 0 q] peak exhibits larger intensity with right circularly polarized (RCP) light and [0 0 $2-q$] peak with left circularly polarized (LCP) light, for convenient comparison of positive CD value of the two peaks, CD of [0 0 q] and [0 0 $2-q$] peaks are difined as $(I_{RCP} - I_{LCP})/(I_{RCP} + I_{LCP})$, $(I_{LCP} - I_{RCP})/(I_{RCP} + I_{LCP})$, respectively.

In-plane-rotation dependence In order to support identifying exact spin structure of $GdCo_2Si_2$, we studied in-plane-rotation dependence of CD as well (Figure 7.4-b). There are three notable observations of the experimental CD. First, both peaks exhibit CD with $\sim$180° period in azimuthal rotation. Second, depending on the azimuthal orientation of the sample, CD exhibits maximum 80% change in CD (between 60° and 140° for [0 0 $2-q$] peak), which is huge. Lastly, at certain azimuthal orientations (40, 60° for [0 0 $2-q$] and 120° for [0 0 q]), the sign of the circular dichroism is flipped to negative. These observations will be utilized in the subsequent subsection to crosscheck the validity of the suggested helimagnetic structure (Figure 7.3-b).

Temperature dependence In order to determine whether the circular dichroism has a magnetic origin, we studied the temperature dependence of the circular dichroism in $GdCo_2Si_2$ (Fig. 7.4-c). The amount of the CD remains constant between 10 - 25 K. Between 25 - 43 K, CD of the [0 0 q] ([0 0 $2-q$]) peak exhibits decrease (increase) of CD, but we do not find any systematic temperature dependence of CD from our measurement data. If the CD were magnetic circular dichroism, it must have quenched to some degree reflecting disordering of AF structure. However, there was no such clear temperature dependence in $GdCo_2Si_2$. Therefore, we conclude that the circular dichroism in $GdCo_2Si_2$ most likely does not have magnetic origin.

Crosschecking the helimagnetic spin structure

Structure factor calculation is capable of predicting circular dichroism of a given spin structure as well. In this subsection, we use the experimental CD to crosscheck whether the spin structure we postulated in the previous subsection (Eqs (7.1), (7.2), (7.3) and Figure 7.3-b) is correct or not. While Ref. [HM96] provides intuitive way to calculate structure factor, but only for linearly polarized lights $\hat{\epsilon}_\sigma$, $\hat{\epsilon}_\pi$. Since $GdCo_2Si_2$ exhibits CD, we need to calculate the structure factor at circularly polarized lights $\hat{\epsilon}_{RCP}$, $\hat{\epsilon}_{LCP}$ as well. Readers interested in detailed discussion of calculating structure factor of diffraction intensity at circularly polarized lights may refer Refs. [FLB08; Wal+13; Kim+22].

First, we need to construct a scattering matrix for circularly polarized lights. As the detector that we used for this measurement does not resolve the polarization of scattered light, we only need to calculate for the cases when incident light is circularly polarized. Likewise to the previous subsection, we only consider E1-E1 contribution. Then the structure factor of an individual magnetic moment looks as following:

$$\left(\hat{\epsilon}' \times \hat{\epsilon}\right) \cdot \vec{m} = \begin{pmatrix} \hat{\epsilon}'_\sigma \times \hat{\epsilon}_{RCP} & \hat{\epsilon}'_\sigma \times \hat{\epsilon}_{LCP} \\ \hat{\epsilon}'_\pi \times \hat{\epsilon}_{RCP} & \hat{\epsilon}'_\pi \times \hat{\epsilon}_{LCP} \end{pmatrix} \cdot \vec{m}, \tag{7.7}$$

where $\hat{\epsilon}_{RCP} = \left(\hat{\epsilon}_\sigma - i\hat{\epsilon}_\pi\right)/\sqrt{2}$, $\hat{\epsilon}_{LCP} = \left(\hat{\epsilon}_\sigma + i\hat{\epsilon}_\pi\right)/\sqrt{2}$ are clockwise and counter-clockwise polarizations, respectively. Using the results from Ref. [HM96], each matrix element can be rewritten as

following:

$$\hat{\epsilon}'_\sigma \times \hat{\epsilon}_{RCP} = \hat{\epsilon}'_\sigma \times \frac{1}{\sqrt{2}}\left(\hat{\epsilon}_\sigma - i\hat{\epsilon}_\pi\right) = -\frac{i}{\sqrt{2}}\hat{k} \tag{7.8}$$

$$\hat{\epsilon}'_\sigma \times \hat{\epsilon}_{LCP} = \hat{\epsilon}'_\sigma \times \frac{1}{\sqrt{2}}\left(\hat{\epsilon}_\sigma + i\hat{\epsilon}_\pi\right) = \frac{i}{\sqrt{2}}\hat{k} \tag{7.9}$$

$$\hat{\epsilon}'_\pi \times \hat{\epsilon}_{RCP} = \hat{\epsilon}'_\pi \times \frac{1}{\sqrt{2}}\left(\hat{\epsilon}_\sigma - i\hat{\epsilon}_\pi\right) = \frac{1}{\sqrt{2}}\left[-\hat{k}' - i\left(\hat{k}' \times \hat{k}\right)\right] \tag{7.10}$$

$$\hat{\epsilon}'_\pi \times \hat{\epsilon}_{LCP} = \hat{\epsilon}'_\pi \times \frac{1}{\sqrt{2}}\left(\hat{\epsilon}_\sigma + i\hat{\epsilon}_\pi\right) = \frac{1}{\sqrt{2}}\left[-\hat{k}' + i\left(\hat{k}' \times \hat{k}\right)\right] \tag{7.11}$$

where $\hat{k}$, $\hat{k}'$ are the wavevector of incident and scattered lights, respectively. Using above relations and Eq. (7.4), the scattering matrix Eq. 7.7 can be rewritten as follows:

$$\left(\hat{\epsilon}' \times \hat{\epsilon}\right) \cdot \vec{m} = \frac{1}{\sqrt{2}}\begin{pmatrix} -i\left(m_z \sin\theta + m_x \cos\theta\right) & +i\left(m_z \sin\theta + m_x \cos\theta\right) \\ -\left(m_z \sin\theta - m_x \cos\theta\right) + i m_y \sin 2\theta & -\left(m_z \sin\theta - m_x \cos\theta\right) - i m_y \sin 2\theta \end{pmatrix}, \tag{7.12}$$

where θ is the Bragg angle of the diffraction geometry. We can simulate the diffraction intensities at circularly polarized lights by summing up the scattering factor of all the consisting magnetic moments:

$$I_{RCP} = \left|\sum_i^{1000}\left(\hat{\epsilon}'_\sigma \times \hat{\epsilon}_{RCP}\right) \cdot \vec{m}_i e^{2\pi i \vec{Q}\cdot\vec{r}_i}\right|^2 + \left|\sum_i^{1000}\left(\hat{\epsilon}'_\pi \times \hat{\epsilon}_{RCP}\right) \cdot \vec{m}_i e^{2\pi i \vec{Q}\cdot\vec{r}_i}\right|^2 \tag{7.13}$$

$$I_{LCP} = \left|\sum_i^{1000}\left(\hat{\epsilon}'_\sigma \times \hat{\epsilon}_{LCP}\right) \cdot \vec{m}_i e^{2\pi i \vec{Q}\cdot\vec{r}_i}\right|^2 + \left|\sum_i^{1000}\left(\hat{\epsilon}'_\pi \times \hat{\epsilon}_{LCP}\right) \cdot \vec{m}_i e^{2\pi i \vec{Q}\cdot\vec{r}_i}\right|^2 \tag{7.14}$$

Applying the helimagnet structure postulated previously, we calculated the CD. While the experimental CD exhibits a clear dependence in in-plane rotation of the sample, our simulation summed up for 1000 Gd moments does not exhibit such behavior remaining constant at 68% (Black dashed line in Figure 7.4-b).

Since the penetration depth of the soft x-ray light in $GdCo_2Si_2$ sample is 4 nm at Gd M_5 absorption edge (Figure 7.1-b), it is possible that only a part of the layers out of 1000 Gd layers might contribute to the circular dichroism. To account for the penetration depth, we decrease the number of Gd layers to sum up in Eqs (7.13), (7.14) instead of 1000. Empirically, summing up 17 layers of Gd moments describes the experimental circular dichroism the best (red solid line for L=0.966 and blue solid line for L=1.034 in Figure 7.4-b); (i) in-plance rotation yields about 180° of period similar to the experimental CD and (ii) the CD value varies between 20% to 60%, which agrees with a part of the experimental CD. However, the model description does not explain the experimental CD flipping sign to negative value at some azimuthal orientations. Furthermore, the ratio between the linearly polarized light I_σ/I_π summing up only 17 layers of Gd moments presented in Figure 7.3-a (red dotted line for L=0.966 and blue dotted line for L=1.034) exhibits a significant in-plane-rotation dependence, which does not agree with the experimental I_σ/I_π. Then the question remains, within this structure factor simulation, why the experimental CD requires less number of Gd layers to sum up while the experimental I_σ/I_π exhibits isotropic behavior (i.e. stay constant at all azimuthal orientations measured)? We believe that the suggested helimagnetic structure is a good candidate explaining the experimental I_σ/I_π. However, since there is a disagreement in predicting the experimental CD, we tentatively conclude that it requires more sophisticated model than simple helimagnetic structure. Further measurements of magnetic diffraction peaks at various [H K L] diffraction geometries requiring hard x-ray regions may be helpful to elucidate the AF spin structure of $GdCo_2Si_2$. Our current best guess is described with Eqs 7.1, 7.2, 7.3 and in Figure 7.3-b.

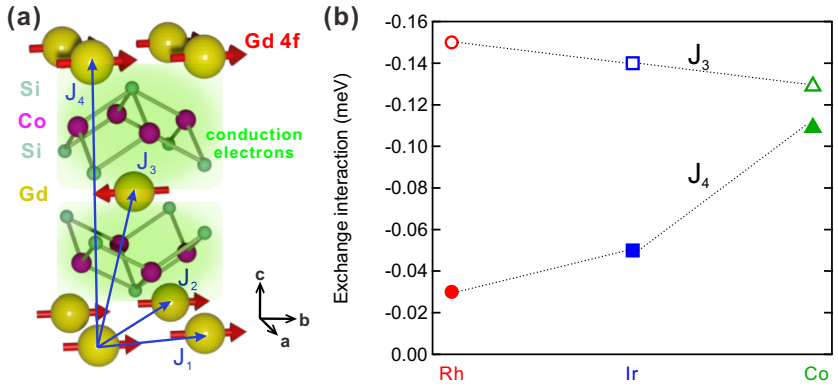

Figure 7.5: (a) Crystal structure of $GdCo_2Si_2$ and relevant indirect exchange couplings within it. (b) DFT calculation of the RKKY coupling in GdT_2Si_2 between the nearest neighboring Gd $4f$ moments ($J_3 = J_{n.n}$) and the next nearest neighboring Gd $4f$ moments ($J_4 = J_{n.n.n.}$) along the [001] axis. Note that the x-axis indicates the transition metal ions T in GdT_2Si_2 compound, which is not scaled.

7.1.5 Frustrated spin structure

As another attempt to identify the spin structure of $GdCo_2Si_2$, we employed a computational approach; density functional theory calculations of exchange couplings and electronic structure of $GdCo_2Si_2$ were conducted by our theory collaborator (Appendix A). As Figure 7.5 shows, the calculated exchange couplings suggest that $GdCo_2Si_2$ has a frustrated spin structure along the c-axis since the nearest and the next nearest exchange couplings along the c-axis both exhibit negative values indicating AF coupling with respect to the $4f$ moments at the origin. Furthermore, unlike the other two sister compounds $GdRh_2Si_2$, $GdIr_2Si_2$, where the exchange coupling between the nearest neighboring Gd $4f$ moments ($J_3 = J_{n.n.}$ in Figure 7.5-a) govern their antiferromagnetism, $GdCo_2Si_2$, has significantly prominent RKKY coupling between the next nearest neighboring Gd $4f$ moments ($J_4 = J_{n.n.n.}$ in Figure 7.5-a) almost as comparable as $J_3 = J_{n.n.}$. We interpret that this is due to the localization of Co $3d$ electrons in $GdCo_2Si_2$. Since the Co $3d$ wave functions are spatially localized compared to Rh $4d$ or Ir $5d$ wave functions, the conduction electrons from Si and Gd ions in $GdCo_2Si_2$ are not well hybridized with the conduction electrons of Co ions. Instead, the conduction electrons of Gd and Si ions hybridize together more strongly and enhance the electron distribution in the Gd-Si-Si-Gd chain along the c-axis. This in the end enhances the exchange coupling between the next nearest Gd $4f$ moments along the c-axis (J_4) making it as comparable as the exchange coupling between the nearest Gd $4f$ moments along the c-axis (J_3) (Figure 7.5-b).

For a crosscheck of the above calculation results, there is an empirical figure to determine the geometrical frustration of an AF spin structure: The ratio between the Néel temperature T_N and the Curie-Weiss temperature Θ_{CW}. The Curie-Weiss temperature indicates the sum of the interactions involved in $GdCo_2Si_2$, and the Néel temperature more or less scales with the strength of the exchange interaction. For unfrustrated system $|\Theta_{CW}|/T_N \sim 1$, and for frustrated magnets $|\Theta_{CW}|/T_N \gg 1$ (usually larger than 10) [Cha+]. $GdCo_2Si_2$ has T_N of 45 K and Θ_{CW} of 55 K [YRI80], therefore the ratio is 1.22. From this, we think that though the spin system might be frustrated according to the DFT calculation, the degree of frustration in $GdCo_2Si_2$ may not be as significant as other geometrically frustrated antiferromagnets.

7.2 Ultrafast dynamics of diffraction intensity and peak position

We found that both the intensity and the peak position of the magnetic diffraction of [0 0 q] and [0 0 2 − q] reflections evolve only in one direction upon equilibrium heating in AF $GdCo_2Si_2$;

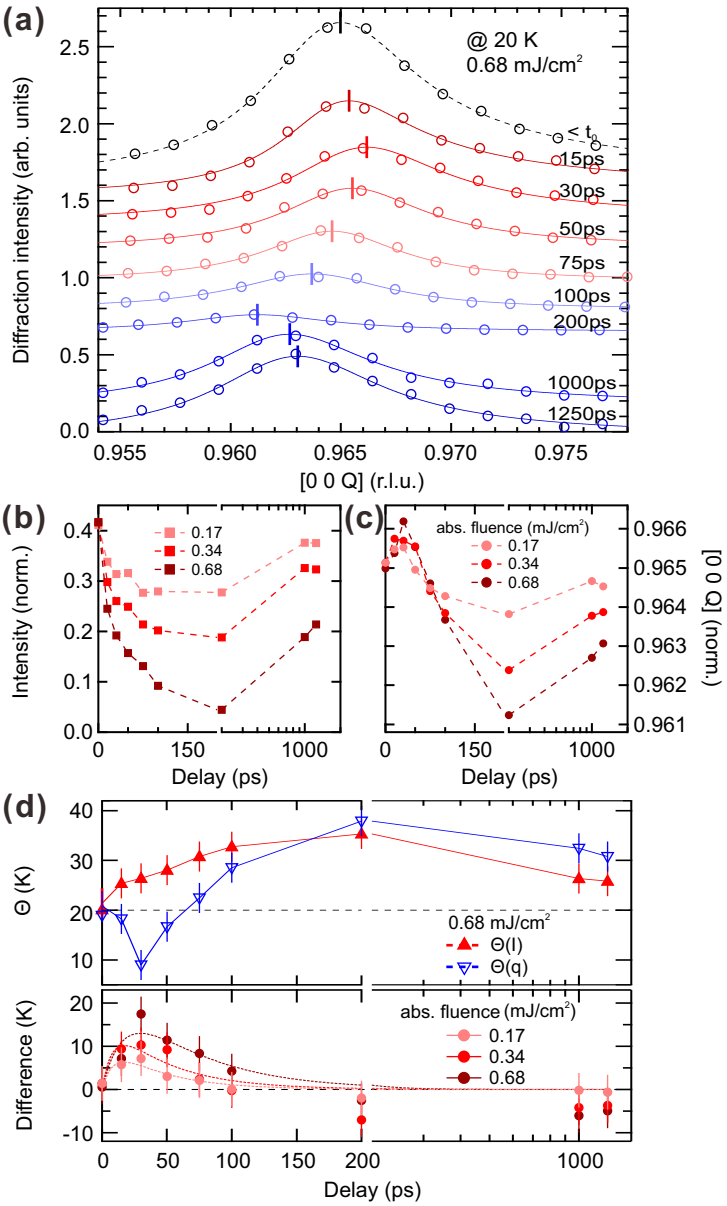

Figure 7.6: (a) Ultrafast dynamics of the [0 0 q] magnetic diffraction peak at a selected fluence. Vertical ticks on top of each curve indicate the peak position. Dashed and solid curves are phenomenological description modeled by Doniach-Sunjic function (see Eq. (5.1)). Temporal evolution of (b) the diffraction intensity and (c) the peak position at various fluences. (d) Temporal evolution of temperature representation of the diffraction intensity $\Theta_I(t)$ and the peak position $\Theta_q(t)$ (top; see text for the conversion) and the difference between the two parameters (bottom). Dotted lines in difference dynamics are guides for the eye.

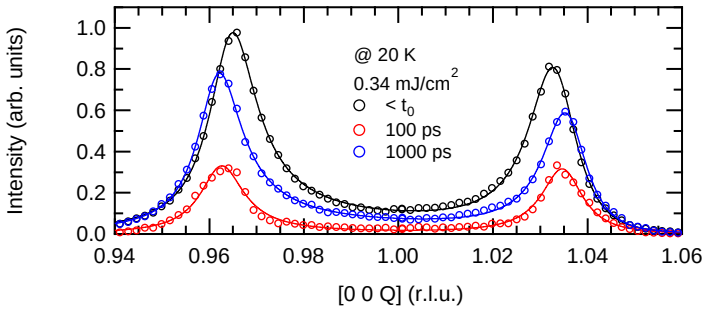

Figure 7.7: Dynamics of $[0\ 0\ q]$ and $[0\ 0\ 2-q]$ reflection of $GdCo_2Si_2$ measured at 50 ps-temporal-resolution mode, which yields larger count rate compared to femtoslicing mode.

intensity decreases and peak position shifts in the direction of decreasing q. However, as we saw in subsection 5.2.1 for reconstructing the actual demagnetization dynamics of $GdCo_2Si_2$, as Figure 5.6-a shows, the peak position shifts in the direction of increasing q for early timescale. In order to investigate the different behavior between the statics and the ultrafast dynamics, we studied ultrafast spin dynamics of $GdCo_2Si_2$ at various fluences employing trRXD.

As the two magnetic diffraction peaks share almost identical temperature-dependent behavior as shown in Fig. 7.2, we measured only the dynamics of the $[0\ 0\ q]$ reflection in detail (Fig. 7.6-a). For crosscheck, we briefly checked the dynamics of the $[0\ 0\ 2-q]$ peaks as well and they exhibit more or less identical dynamics (Fig. 7.7). Upon photoexcitation, like upon equilibrium heating, the diffraction peaks evolve in two different aspects; intensity and peak position. However, the behavior is significantly different from equilibrium demagnetization. While, the intensity exhibits $\sim$10 ps demagnetization dynamics until 200 ps (Fig. 7.6-b), the peak position shifts in the direction of increasing q for the first 30 ps, and subsequently in the direction of decreasing q till 200 ps (Figure 7.6-c). After 200 ps, both the integrated intensity and position return to initial state altogether at a rate of $\sim$100 ps.

7.2.1 Disparate dynamics of the exchange couplings and the antiferromagnetic order parameter

We learned that while, upon equilibrium heating, the peak position shifts monotonously in the direction of decreasing q. In other words, the period of the long-range Gd $4f$ ordering simply increases upon equilibrium heating. However, upon ultrashort optical excitation, the period of the AF structure decreases for the first 30 ps and subsequently increases for 200 ps. What makes it more interesting is that the magnetic order dynamics does not exhibit such behavior in the early timescale. To emphasize the disparate dynamics of the intensity $I(t)$ and the position $q(t)$ of the diffraction peak, we converted $I(t)$ and $q(t)$ into temperature representation, $\Theta_I(t)$ and $\Theta_q(t)$, respectively, using the temperature dependent relation of the intensity $I(T)$ and the position $q(T)$ acquired from the equilibrium heating measurement. Fig. 7.6-d presents $\Theta_I(t)$ and $\Theta_q(t)$ dynamics at a selected pump fluence and the differences between the two temperature representations at various fluences. The difference dynamics increases for the first 30 ps and effectively quenches by 200 ps. As the pump fluence increases, the amount of the difference increases and it takes longer time to quench. The magnetic diffraction intensity is the squared Gd $4f$ AF order parameter, and the period of the long-range AF structure reflects exchange coupling configuration between $4f$ moments in $GdCo_2Si_2$ [JM91]. The 200-ps-long disparate dynamics of the two different physical parameters imply 200-ps-long non-thermal state of Gd $4f$ moments in $GdCo_2Si_2$. We speculate that this peculiarly long non-thermal state is due to the localized nature of the Gd $4f$ moments. This result suggests that $4f$ spin structure in Gd-based magnets may stay non-thermalized for even several hundreds of picoseconds upon photoexcitation, especially when they lack coupling

to surrounding environment e.g. almost nonexistent spin-orbit interaction in elemental Gd. For example, it has been shown that elemental Gd exhibits drastically different dynamics of itinerant conduction electrons and localized $4f$ electrons due to the lack of the spin-orbit interaction, hence the lack of the spin-lattice coupling [Wie+11; And+15; Fri+15]. As shown in Chapter 6, in $GdRh_2Si_2$, the $4f$ spin dynamics exhibits almost identical dynamics with the conduction electrons since Rh $4d$ electrons are *not* localized in $GdRh_2Si_2$ unlike Co $3d$ electrons in $GdCo_2Si_2$. Based on the previous studies on elemental Gd dynamics and the density functional theory calculation results presented in 7.1.5, we speculate that the localization of Co $3d$ electrons in $GdCo_2Si_2$ and inherent small magnetoscrystalline anisotropy of Gd $4f$ moments result slow thermalization of $4f$ spins upon photoexcitation in $GdCo_2Si_2$.

7.3 Conclusion

In this chapter, statics and ultrafast dynamics of magnetic diffraction peak of $[0\ 0\ q]$ and $[0\ 0\ 2-q]$ reflections in antiferromagnetic $GdCo_2Si_2$ were explored employing resonant elastic magnetic soft x-ray diffraction. From statics study and calculations, we showed that $GdCo_2Si_2$ exhibit various exotic magnetic properties unlike other family compounds such as incommensurate spin order, deviation from mean-field-like demagnetization, circular dichroism, and frustrated spin structure. Though we do not identify the exact spin structure of AF $GdCo_2Si_2$ in this study, we presents various methods for spin structure identification such as structure factor calculation of linearly and circularly polarized incident lights, density functional theory calculation. Our current best candidate of the spin structure is a helimagnet repeating 483 rotations every 500 unit cells along the c-axis (at 10 K). Further measurements at various magnetic diffraction peaks are required to precisely identify its spin structure.

Both the diffraction intensity and the peak position evolve upon equilibrium heating; the intensity decrease implies quenching of antiferromagnetic (AF) order and the peak position shift in the direction of decreasing q indicates a gradual increase of long-range AF order period along the c-axis. Interestingly enough, upon ultrashort photoexcitation, while the intensity dynamics exhibits curves resembling demagnetization dynamics of other lanthanides, the period dynamics decreases for early 30 ps, which does not appear in equilibrium heating experiment. Since the period of AF order reflects the exchange coupling configuration in $GdCo_2Si_2$, we argue that the long-range $4f$ AF order and exchange couplings between $4f$ moments in $GdCo_2Si_2$ exhibit disparate dynamics. This disparate dynamics lasts for 200 ps. The disparate dynamics implies non-thermal state of Gd $4f$ moments for several hundreds of picoseconds upon photoexcitation. We speculate that this peculiarly long non-thermal state is due to the localization of Co $3d$ electrons in $GdCo_2Si_2$ and small magnetocrystalline anisotropy of Gd $4f$ moments.

This page is intentionally left blank.

Chapter 8

Summary and outlook

This thesis investigated the role of the indirect Ruderman-Kittel-Kasuya-Yosida (RKKY) exchange interaction in ultrafast spin dynamics of $4f$ antiferromagnets $Ln\,T_2Si_2$. The indirect RKKY exchange interaction is a vital physical parameter governing the characteristic magnetism of lanthanides coming from spatial localization of exceptionally large $4f$ magnetic moments, which take the surrounding conduction electrons as mediator of the magnetic interaction. The proximity of oppositely aligned magnetic sublattices in AF $Ln\,T_2Si_2$ opens a new demagnetization channel, direct spin transfer channel. Since this direct spin transfer channel between the oppositely aligned magnetic sublattices in $Ln\,T_2Si_2$ involves both inter-atomic couplings of $4f$ moments from different lanthanide atoms and intra-atomic coupling between itinerant conduction and localized $4f$ electrons, employing femtosecond time-resolved experimental techniques, we studied these inter- and intra-atomic couplings from ultrafast spin dynamics of $4f$ antiferromagnets.

In Chapters 4 and 5, by comparing ultrafast spin dynamics of a family of $4f$ antiferromagnets $Ln\,T_2Si_2$ which share almost identical lattice parameters and antiferromagnetic structure, we unambiguously showed that the direct spin transfer channel between antiferromagnetically coupled $4f$ moments can enhance the angular momentum transfer upon photoexcitation. The transfer rate scales with the antiferromagnetic indirect exchange interaction with constant offset contribution from phonon-mediated Elliott-Yafet-like spin-flip scattering. As introduced in Chapter 2, the strength of the RKKY interaction between $4f$ moments at different lanthanide atoms can be described as following: $J \propto |I|^2\chi$, where I is the overlap integral between the wave functions of localized $4f$ electrons and of itinerant conduction electrons and χ is the non-local susceptibility of the conduction electrons around the Fermi level. In Chapter 4, by swapping Ln ions in $Ln Rh_2Si_2$, we single out the role of the localized $4f$ electrons. Systematic change in size of the $4f$ magnetic moments yields various de Gennes factors. We showed that both the angular momentum transfer rate and the strength of the antiferromagnetic indirect exchange interaction scale with the de Gennes factor. This scaling relation reflects the dominant role of the direct spin transfer between antiparallel $4f$ spins. In Chapter 5, by swapping T ions in $Gd\,T_2Si_2$, we single out the role of the itinerant conduction electrons. Modifying conduction electrons changes the spin polarization of Gd $5d$ electrons around the Fermi energy. This significantly modifies the non-local susceptibility of conduction electrons χ and, in consequence, the strength of the antiferromagnetic indirect exchange interaction. Therefore, from systematic studies of inter-atomic indirect exchange coupling, we provide two different ways (modifying $4f$ and conduction electrons) to finely tune the strength of the antiferromagnetic indirect exchange coupling and the angular momentum transfer rate upon photoexcitation, which will be helpful for designing spintronic devices in future.

The fact that we can single out the role of each component of the indirect exchange interaction from simple comparative analysis of the ultrafast spin dynamics is one of the strong points of $Ln\,T_2Si_2$ compounds. We could not achieve this from comparative analysis of large number of elemental lanthanides since they do not share comparably uniform lattice and magnetic structures. Future studies can employ $Ln\,T_2Si_2$ as a test-bed for studying the relation between the indirect

exchange coupling and the ultrafast spin dynamics. Since thermal excitation has been extensively studied in this thesis, one can study how external magnetic field changes ultrafast spin dynamics of $Ln\,T_2Si_2$ to extend our understanding on how damping and precession of $4f$ spins affects the direct spin transfer.

Another strong point of $Ln\,T_2Si_2$ compounds is that the samples have stayed robust against atmospheric air or low-vacuum desiccator environment for the last 5 years. This means that even though the samples have been stored in rather forgiving storage conditions the bare single crystal samples have consistently exhibited antiferromagnetism for multiple times of RXD measurements (i.e. beamtimes at synchrotrons), and even for ARPES measurements if the sample is well exfoliated in in-situ environment. Though it might sound dull in the scientific perspective, in the practical perspective, this robustness of the samples is indeed a strong point in actual implementation of spintronic devices which, in principle, should have at least a few years of lifetime.

In Chapter 6, we explored ultrafast dynamics of transient electronic temperature, exchange splitting of a surface state, and long-range $4f$ antiferromagnetic ordering of AF $GdRh_2Si_2$ at various fluences. The resemblance of the demagnetization timescales of the surface conduction electrons and localized Gd $4f$ moments suggests that there is a strong intra-atomic on-site exchange coupling between the conduction and $4f$ electrons, unlike ferromagnetic elemental Gd [And+15; Wie+11]. To understand the intricate energy and angular momentum exchange within AF $GdRh_2Si_2$ upon photoexcitation, we applied a microscopic three temperature model for antiferromagnets based on a Landau-Lifshitz-Bloch equation. Derivation of the exchange-enhancement due to direct spin transfer channel and extensive details about the role of each physical parameter (fitting parameter) in the model have been presented for future studies in section 2.2. The model qualitatively well describes the experimental results. However, to explain robust magnetic order remaining even when the equilibrated temperature is above the Néel temperature T_N, a transient increase of the Néel temperature T_N^* is introduced within the M3TM as a phenomenological description. This transient increase of T_N^* scales with the fluence of the optical excitation. We believe this indicates a transient increase of exchange interaction within $GdRh_2Si_2$. Regarding fluence-dependence, while the model predicts equilibrium-like demagnetization behavior with increasing fluence, the experimental results for both the surface and bulk magnetic order do not agree with the model prediction. From these two disagreements, transient increase of T_N^* and equilibrium-like fluence dependence, we conclude that the predictive power of the M3TM in quantitative analysis is rather limited. Because of the above-mentioned limitations, we strongly argue that it is very important to achieve corresponding experimental transient electron/lattice temperature dynamics to describe experimental magnetic order dynamics with a M3TM.

Employing two complementary time-resolved experimental techniques, time- and angle-resolved photoemission spectroscopy and time-resolved resonant elastic magnetic soft x-ray diffraction, ultrafast dynamics of surface ferromagnetic order and long-range antiferromagnetic order of a layered antiferromagnetic structure were measured, respectively. Combining these two complementary experimental techniques sensitive to both surface in-plane and bulk out-of-plane spin order can be applied to study emerging field of van der Waals 2D antiferromagnets as well [Wan+21; Rah+21; VR19].

In Chapter 7, we showed unconventional antiferromagnetism of $GdCo_2Si_2$: $GdCo_2Si_2$ exhibits incommensurate spin order, circular dichroism, and has frustrated spin structure. Furthermore, upon equilibrium heating, $GdCo_2Si_2$ exhibits quenching of AF order which does not follow mean-field-like behavior and period increase of long-range AF structure. None of the above unconventional antiferromagnetism were observed in other AF $Ln\,T_2Si_2$ compounds. Upon optical excitation, the period dynamics exhibits decrease for early 30 ps and subsequent increase dynamics while the AF order dynamics exhibits simple demagnetization dynamics. This disparate dynamics of the period and AF order lasts for 200 ps. Since the period of long-range AF structure is determined by indirect RKKY coupling configuration between $4f$ moments, the disparate dynamics of the exchange couplings and AF $4f$ order imply non-thermal state of Gd $4f$ moments for several hun-

dreds of picoseconds upon photoexcitation. Measuring ultrafast dynamics of exchange couplings in lanthanide-based magnets with incommensurate spin order such as LnT_2 or LnC_2 compounds [Ato68a; Ato68b; Ato68c; Ato69b; Ato69a; Ato04] is recommended to elucidate the origin of the disparate dynamics of exchange coupling and AF order in $GdCo_2Si_2$. Our current best guess is due to the small magnetocrystalline anisotropy of Gd $4f$ moments and localization of Co $3d$ electrons in $GdCo_2Si_2$.

Since the exact antiferromagnetic spin structure of $GdCo_2Si_2$ has not been reported yet, we present two different ways to speculate its spin structure. First, first-principles calculations within a density functional theory explain that the spin structure is frustrated since the indirect exchange coupling between the next nearest neighbor $4f$ moments along the c-axis is enhanced as strong as the coupling between the nearest neighboring $4f$ moments due to localization of $3d$ electrons of Co ions in $GdCo_2Si_2$. Second, structure factor calculations with linearly polarized incident x-ray lights suggest helical antiferromagnet propagating along the c-axis with a period of 500 unit cells. However, experimental circular dichroism does not agree with structure factor calculations with circularly polarized incident x-ray lights based on the suggested helical antiferromagnet. Further studies of various magnetic diffraction peaks are required to determine the exact spin structure of $GdCo_2Si_2$.

Various aspects of indirect RKKY exchange interaction in antiferromagnetism of $4f$ antiferromagnets have been studied in this thesis; incommensurate and commensurate spin order; itinerant conduction and localized $4f$ electrons; intra- and inter-atomic couplings; surface ferromagnetic and bulk antiferromagnetic orders. Though I invested all my efforts to achieve answers for the studies that I have embarked on and from that I learned a lot, as I discussed about various topics for future studies in this chapter, I feel more confused now because it brings even more questions than answers; what if I apply magnetic fields during the dynamics?; can I apply these experimental methods to 2D antiferromagnets as well?; why haven't others extensively discussed about the limitation of the M3TM in quantitative predictive power even though it has been applied so many times? what other models will be good for the quantitative analysis?; why does an antiferromagnet with an incommensurate spin order exhibits disparate dynamics of exchange couplings and magnetic order? Is it reproducible in other $4f$ magnets? Even so, everything deserves an end, and so does this thesis. Therefore, instead of keep questioning, I pause here and hope this thesis be a good starting point for someone who newly endeavours this field of $4f$ antiferromagnetism in future.

This page is intentionally left blank.

Appendix A

Calculation details of density functional theory

A part of this chapter was published in "Exchange scaling of ultrafast angular momentum transfer in 4f antiferromagnets" *Nature Materials* **21**, 514–517 (2022)

Our collaborator Prof. Dr. Arthur Ernst conducted the first-principles calculations within a density functional theory (DFT) presented in this thesis. Here we present the details for the DFT calculation. The exchange couplings and the electronic density of states presented in Chapters 4, 5 and 7 were calculated using a self-consistent Green's function method within density functional theory (DFT) [Gei+15; Hof+20] in a generalized gradient approximation (GGA) [PBE96], which is considered precise, but computationally costly. Readers interested in this calculation methods may refer [Hug07; Ern07].

Strongly localized $4f$ electrons were treated within the GGA + U approach. The corresponding effective Hubbard parameter $U^* = U - J$ was chosen in such a way as to guarantee a good agreement of calculated and experimental Néel temperature [AZA91]. Although the Néel temperature is a macroscopic quantity, it can be evaluated using microscopic quantum mechanical calculations through the Heisenberg model. The exchange parameters in the Heisenberg model represent the overlap between various orbitals and can be obtained from first-principles calculations. The parameters presented in this thesis were estimated using the magnetic force theorem implemented within the multiple scattering theory [Lie+87].

The electronic and magnetic properties of the LnT_2Si_2 materials are distinguishable by the effect of the lanthanide elements within them, which harbor strongly localized $4f$ states. These $4f$ states form magnetic moments which interact primarily via free electrons, which in turn are characterized by the density of states at the Fermi level. The strong localization of the $4f$ electrons renders hybridization with valence states of other elements insignificant, so other types of magnetic interaction can be excluded. Thus, long range magnetic order in these compounds is driven primarily by the RKKY interaction.

Appendix B

Optical characterization of $4f$ antiferromagnets

chapter was published in "Exchange scaling of ultrafast angular momentum transfer in 4f antiferromagnets" *Nature Materials* **21**, 514–517 (2022)

LnT_2Si_2	n_0	k	Pump depth (nm)	Pump spot (μm × μm)	R
$PrRh_2Si_2$	3.3±0.1	3.1±0.1	20	310±6×346±6	0.67
$NdRh_2Si_2$	3.4±0.1	3.5±0.1	17	394±6×433±6	0.71
$SmRh_2Si_2$	3.7±0.1	3.4±0.2	18	411±5×545±6	0.72
$GdCo_2Si_2$	4.6±0.5	3.8±0.7	16	411±5×546±5	0.61
$GdRh_2Si_2$	3.3±0.1	3.2±0.2	19	166±26×321±60	0.72
$GdIr_2Si_2$	3.0±0.2	2.5±0.2	24	244±36×241±30	0.73
$TbRh_2Si_2$	3.7±0.1	3.3±0.1	18	411±5×546±5	0.74
$DyRh_2Si_2$	3.4±0.1	3.1±0.1	20	244±36×241±30	0.74
$HoRh_2Si_2$	3.2±0.1	3.2±0.1	19	244±36×241±30	0.76

Table B.1: Effective values of optical constants and relevant properties for the pump beam. The pump depth is the penetration depth of 800 nm light in the samples (see text for the calculation). The reflectivity of the pump R is calculated for the corresponding Bragg angle. Reproduced with permission from Springer Nature [Win+22].

Optical constants are essential for calculating penetration depth and absorbed fluence. However, the optical constants of the LnT_2Si_2 materials are not available in literature. To assess the validity of comparing the experiments on these materials, Dr. Yoav William Windsor measured the optical constants of all materials for λ= 800 nm light by measuring angle-dependent reflectivity. Using the Fresnel equations, we extracted the values as $n = n_0 + ik$ (Table. B.1).

Another aspect to consider for calculating the pump penetration depth is the incident angle of the pump light. In the magnetic x-ray diffraction geometry, the pump light is nearly-collinear to the x-ray probe lights ($\sim$1° offset). The x-ray angle is defined by Bragg's law, and therefore varies between the resonances of the different materials (see Fig. 3.2, vertical axes in the left column). Using Snell's law, we estimate the refracted angles of the pump beam to the surface normal inside the material ϕ, and find that they are nearly identical in the range 15° - 18°. Finally, the pump penetration depth is estimated as $\lambda(4\pi k)^{-1}\cos\phi$.

The pump spot size was estimated as the full-width at half maximum of the spot profile (see Table B.1). The x-ray probe spot was in the vertical direction cut to 40 μm (except for $GdRh_2Si_2$, in which it was 170±66 μm). In the horizontal direction the probe spot was kept to half the size of the pump spot.

List of publications

Publications discussed in this thesis

Y. W. Windsor, S.-E. Lee, D. Zahn, V. Borisov, D. Thonig, K. Kliemt, A. Ernst, C. Schüßler-Langeheine, N. Pontius, U. Staub, C. Krellner, D. V. Vyalikh, O. Eriksson, and L. Rettig, *Exchange scaling of ultrafast angular momentum transfer in 4*f *antiferromagnets*, Nature Materials **21**, 514-417 (2022).

S.-E. Lee, Y. W. Windsor, A. Fedorov, K. Kliemt, C. Krellner, C. Schüßler-Langeheine, N. Pontius, M. Wolf, U. Atxitia, D. V. Vyalikh, and L. Rettig, *Robust magnetic order upon ultrafast excitation of an antiferromagnet*, arxiv:2207.00789 [cond-mat.str-el] (Submitted to Advanced Materials Interfaces)

Additional publications

B. Andres, S.-E. Lee, and M. Weinelt, *The role of spin-lattice coupling for ultrafast changes of the magnetic order in rare earth metals*, Applied Physics Letters **119**, 182404 (2021).

Published datasets

B. Andres, S.-E. Lee, and M. Weinelt, *The role of spin-lattice coupling for ultrafast changes of the magnetic order in rare earth metals*, Zenodo

Statement of contributions

Chapter 2 All the samples studied in this thesis were grown by Prof. Dr. Cornelius Krellner and Dr. Kristin Kliemt. The microscopic three temperature model based on the Landau-Lifshitz-Bloch equation was developed by Florian Jakobs and Dr. Unai Atxitia [JA22a].

Chapter 3 The equilibrium resonant x-ray diffraction measurements were conducted at ReSoXS endstation of SIM beamline of Swiss Light Source in Switzerland with beamline support from Prof. Dr. Urs Staub and at PM3 beamline of BESSY II in Germany with beamline support from Dr. Christian Schüßler-Langeheine and Dr. Torsten Kachel. The time-resolved resonant x-ray diffraction measurements were conducted at FemtoSpeX beamline of BESSY II in Germany with beamline support from Dr. Christian Schüßler-Langeheine and Dr. Niko Pontius. The time- and angle-resolved photoemission spectroscopy setup was designed and built by Michele Puppin et al. [Pup+15].

Chapter 4 Dr. Laurenz Rettig and Dr. Yoav William Windsor had the idea for the project. The resonant x-ray diffraction measurements were conducted by Dr. Laurenz Rettig, Dr. Yoav William Windsor, Dr. Daniela Zahn, and myself with the above-mentioned beamline support. Dr. Laurenz Rettig, Dr. Yoav William Windsor and I did the data analysis and interpretation. First-principles calculations within a density functional theory presented was conducted by Prof. Dr. Arthur Ernst.

Chapter 5 Dr. Laurenz Rettig and Dr. Yoav William Windsor had the idea for the project. The resonant x-ray diffraction measurements were conducted by Dr. Laurenz Rettig, Dr. Yoav William Windsor, Dr. Daniela Zahn, and myself with the above-mentioned beamline support. I did the data analysis and interpretation consulting with Dr. Laurenz Rettig, Dr. Yoav William Windsor, and Prof. Dr. Arthur Ernst. First-principles calculations within a density functional theory presented was conducted by Prof. Dr. Arthur Ernst.

Chapter 6 Dr. Laurenz Rettig had the idea for the project. The time- and angle-resolved photoemission spectroscopy measurements were conducted by Dr. Alexader Fedorov, Prof. Dr. Denis V. Vyalikh, Dr. Yoav William Windsor and Dr. Laurenz Rettig. The subsequent data analyses were conducted by myself consulting with Dr. Laurenz Rettig. The time-resolved resonant x-ray diffraction measurements are from Chapter 4. The FORTRAN-based simulation code is provided by Dr. Unai Atxitia. I conducted the simulations and corresponding interpretation consulting with Dr. Laurenz Rettig and Dr. Unai Atxitia.

Chapter 7 I had the idea for the project. Dr. Laurenz Rettig found the incommensurate spin order of $GdCo_2Si_2$. The resonant x-ray diffraction measurements were conducted by Dr. Laurenz Rettig, Dr. Yoav William Windsor, Dr. Daniela Zahn, and myself with the above-mentioned beamline support. I did the data analysis and interpretation consulting with Dr. Laurenz Rettig, Dr. Yoav William Windsor, and Prof. Dr. Arthur Ernst. First-principles calculations within a density functional theory presented was conducted by Prof. Dr. Arthur Ernst.

Acknowledgement

I thank Dr. Laurenz Rettig for his guidance during my PhD program. His open ears to honest words, challenging scientific comments and encouragements have driven me to the end of this PhD program which I never thought I could reach. Also, I thank him for securing my contract throughout the last five years. Thankfully, he proofread most of the chapters in this thesis for me. I thank Dr. Yoav William Windsor for teaching me time-resolved resonant elastic magnetic x-ray diffraction, and subsequent data analysis methodology. His flexible and insightful viewpoints always enlightened me about how to formulate a good scientific story from our measurement data. He also proofread one chapter of this thesis for me. I thank Dr. Maciej Dendzik and Dr. Tommaso Pincelli for teaching me time- and angle-resolved photoemission spectroscopy, and subsequent data analysis methods for it. Especially, Dr. Pincelli proofread one chapter of this thesis and provided invaluable comments on the purpose of writing a PhD thesis. Dr. Daniela Zahn thankfully participated all the beamtimes we had at BESSY II and SLS. Her dedication and willingness to do night shifts all the time for the team made it possible to achieve such beautiful results presented in this thesis. Group members of AG Rettig and AG Ernstorfer made the working environment very vibrant, which I appreciate. I want to thank Sven Kubala very much for his technical supports. He always helped me to solve technical troubles, taught me the right way to manipulate experimental devices in general. His brutal sense of humor supported me to get through difficult times during my PhD program. For the same reason (technical supports), I thank technician staffs of mechanical workshop, electric workshop and Physical Chemistry in Fritz-Haber-Institut. Thanks to Prof. Dr. Martin Wolf, I could safely continue research even at home-office during the Covid-19 crisis period. I really appreciate his dedication to our department.

I appreciate Prof. Dr. Martin Weinelt for guiding me as a second supervisor of my PhD program. Thanks to his dedicated service for TRR 227 collaborative research center, I could participate all the helpful programs and courses provided by iRTG. The lessons he provided during my master thesis time also helped me a lot. I want to thank Dr. Britta Anstötz and Dr. Christian Frischkorn as well for the administration of the iRTG program and other TRR 227-related events.

Prof. Dr. Arthur Ernst provided me such beautiful and intuitive explanations how the indirect RKKY exchange coupling governs the antiferromagnetism in $Ln\,T_2\mathrm{Si}_2$ with ab-initio density functional theory calculations. Dr. Unai Atxitia taught me how to simulate ultrafast demagnetization dynamics within the microscopic three temperature model (M3TM). Thankfully, he developed an M3TM code based on the Landau-Lifshitz-Bloch equation for antiferromagnets and explained to me how his FORTRAN-based code operates.

I thank Prof. Dr. Cornelius Krellner and Dr. Kristin Kliemt for providing wonderful samples of $Ln\,T_2\mathrm{Si}_2$ compounds. That exceptional quality of the samples they provided made the measurement process much more straightforward.

Prof. Dr. Urs Staub supported us during the beamtimes at Swiss Light Source. His advice helped us to make good measurement plans and subsequent post-measurement data analyses. Dr. Christian Schüßler-Langeheine and Dr. Niko Pontius supported us during all the beamtimes at BESSY II. Their dedicated support and post-beamtime explanation of their sophisticated setup made it possible to achieve beautiful results presented in this thesis.

I thank Google Translation for translating the abstract of this thesis in German.

While I got many supports from various people, if any error or typo are contained in this work,

I am the only person who is responsible for all of them.

All the happy moments with my friends, Jan Böhnke, Xinwei Zheng, Filippo Tedoli, Soléne Besson, and Chika Okura (now Chika Kojio) have made me motivated during my study. Dudes on "Physics Channel" on Arcalive and academics on "Reviewer2 Must Be Stopped!" on Facebook deserve my gratitude for reminding me that I am not the only miserable PhD student in this world when I was having a hard time. Finally, last but not least, I would like to thank my mother for her invaluable support and encouragement. Without her, I could not finish this PhD program.

Declaration of authorship

I, Sang-Eun Lee, hereby declare to the Freie Universität Berlin that I have completed the submitted dissertation independently and without the use of sources and aids other than those indicated. The present thesis is free from plagiarism. I have marked as such all statements are taken literally or in content from other writings. This dissertation has not been submitted in the same or similar form in any previous doctoral procedure.

I agree to have my thesis examined by a plagiarism examination software.

Berlin, on December 20, 2022

Sang-Eun Lee

Bibliography

[Her87] H. Hertz. "Ueber einen Einfluss des ultravioletten Lichtes auf die electrische Entladung". In: *Annalen der Physik* 267.8 (1887), pp. 983–1000. DOI: https://doi.org/10.1002/andp.18872670827. eprint: https://onlinelibrary.wiley.com/doi/pdf/10.1002/andp.18872670827. URL: https://onlinelibrary.wiley.com/doi/abs/10.1002/andp.18872670827.

[Ein05] A. Einstein. "Über einen die Erzeugung und Verwandlung des Lichtes betreffenden heuristischen Gesichtspunkt". In: *Annalen der Physik* 322.6 (1905), pp. 132–148. DOI: https://doi.org/10.1002/andp.19053220607. eprint: https://onlinelibrary.wiley.com/doi/pdf/10.1002/andp.19053220607. URL: https://onlinelibrary.wiley.com/doi/abs/10.1002/andp.19053220607.

[RK54] M. A. Ruderman and C. Kittel. "Indirect Exchange Coupling of Nuclear Magnetic Moments by Conduction Electrons". In: *Phys. Rev.* 96 (1 Oct. 1954), pp. 99–102. DOI: 10.1103/PhysRev.96.99. URL: https://link.aps.org/doi/10.1103/PhysRev.96.99.

[HPT55] C. L. Hammer, R. W. Pidd, and K. M. Terwilliger. "Betatron Oscillations in the Synchrotron". In: *Review of Scientific Instruments* 26.6 (1955), pp. 555–556. DOI: 10.1063/1.1715241. eprint: https://doi.org/10.1063/1.1715241. URL: https://doi.org/10.1063/1.1715241.

[Kas56] Tadao Kasuya. "A Theory of Metallic Ferro- and Antiferromagnetism on Zener's Model". In: *Progress of Theoretical Physics* 16.1 (July 1956), pp. 45–57. ISSN: 0033-068X. DOI: 10.1143/PTP.16.45. eprint: https://academic.oup.com/ptp/article-pdf/16/1/45/5266722/16-1-45.pdf. URL: https://doi.org/10.1143/PTP.16.45.

[Yos57] Kei Yosida. "Magnetic Properties of Cu-Mn Alloys". In: *Phys. Rev.* 106 (5 June 1957), pp. 893–898. DOI: 10.1103/PhysRev.106.893. URL: https://link.aps.org/doi/10.1103/PhysRev.106.893.

[DS63] P. G. De Gennes and D. Saint-James. "Helical structures of the heavy rare earth metals". In: *Solid State Communications* 1.3 (Aug. 1963), pp. 62–66. ISSN: 0038-1098. DOI: 10.1016/0038-1098(63)90359-4.

[BS64] C. N. Berglund and W. E. Spicer. "Photoemission Studies of Copper and Silver: Theory". In: *Phys. Rev.* 136 (4A Nov. 1964), A1030–A1044. DOI: 10.1103/PhysRev.136.A1030. URL: https://link.aps.org/doi/10.1103/PhysRev.136.A1030.

[Koe65] W. C. Koehler. "Magnetic Properties of Rare-Earth Metals and Alloys". In: *Journal of Applied Physics* 36.3 (Mar. 1965). Publisher: American Institute of Physics, pp. 1078–1087. ISSN: 0021-8979. DOI: 10.1063/1.1714108.

[Ato68a] Masao Atoji. "Magnetic Structure of DyC_2". In: *The Journal of Chemical Physics* 48.8 (Apr. 1968), pp. 3384–3388. ISSN: 0021-9606, 1089-7690. DOI: 10.1063/1.1669630. URL: http://aip.scitation.org/doi/10.1063/1.1669630 (visited on 04/27/2022).

[Ato68b] Masao Atoji. "Magnetic Structure of TbAg $_2$". In: *The Journal of Chemical Physics* 48.8 (Apr. 1968), pp. 3380–3383. ISSN: 0021-9606, 1089-7690. DOI: 10.1063/1.1669629. URL: http://aip.scitation.org/doi/10.1063/1.1669629 (visited on 04/27/2022).

[Ato68c] Masao Atoji. "Magnetic Structures of TbAu2". In: *The Journal of Chemical Physics* 48.2 (Jan. 1968). Publisher: American Institute of Physics, pp. 560–564. ISSN: 0021-9606. DOI: 10.1063/1.1668683. URL: https://aip.scitation.org/doi/abs/10.1063/1.1668683 (visited on 05/03/2022).

[Ato69a] Masao Atoji. "Magnetic Structure of HoAg $_2$". In: *The Journal of Chemical Physics* 51.9 (Nov. 1969), pp. 3882–3885. ISSN: 0021-9606, 1089-7690. DOI: 10.1063/1.1672606. URL: http://aip.scitation.org/doi/10.1063/1.1672606 (visited on 04/27/2022).

[Ato69b] Masao Atoji. "Magnetic Structures of DyAu $_2$ and DyAg $_2$". In: *The Journal of Chemical Physics* 51.9 (Nov. 1969), pp. 3877–3882. ISSN: 0021-9606, 1089-7690. DOI: 10.1063/1.1672605. URL: http://aip.scitation.org/doi/10.1063/1.1672605 (visited on 04/27/2022).

[Mah70] G. D. Mahan. "Theory of Photoemission in Simple Metals". In: *Phys. Rev. B* 2 (11 Dec. 1970), pp. 4334–4350. DOI: 10.1103/PhysRevB.2.4334. URL: https://link.aps.org/doi/10.1103/PhysRevB.2.4334.

[Née70] Louis Eugène Félix Néel. *The Nobel Prize in Physics 1970*. 1970. URL: https://www.nobelprize.org/prizes/physics/1970/neel/lecture/ (visited on 08/15/2022).

[Ell+72] R. J. Elliott et al. *Magnetic Properties of Rare Earth Metals*. Ed. by R. J. Elliott. 1st ed. Springer New York, NY, 1972. ISBN: 978-1-4757-5693-7. DOI: 10.1007/978-1-4757-5691-3.

[YRI80] J. K. Yakinthos, Ch. Routsi, and P. F. Ikonomou. "Magnetic properties of ternary TCo2Si2 compounds (T = Gd, Tb, Dy, Ho, Er, Y)". In: *Journal of the Less Common Metals* 72.2 (Aug. 1980), pp. 205–208. ISSN: 0022-5088. DOI: 10.1016/0022-5088(80)90138-1. URL: https://www.sciencedirect.com/science/article/pii/0022508880901381 (visited on 08/25/2022).

[FN83] Israel Felner and Israel Nowik. "Local and itinerant magnetism and superconductivity in R Rh2si2 (R = rare earth)". In: *Solid State Communications* 47.10 (Sept. 1983), pp. 831–834. ISSN: 0038-1098. DOI: 10.1016/0038-1098(83)90076-5.

[ŚLS83] M. Ślaski, J. Leciejewicz, and A. SzytuŁa. "Magnetic ordering in HoRu2Si2, HoRh2Si2, TbRh2Si2 and TbIr2Si2 by neutron diffraction". In: *Journal of Magnetism and Magnetic Materials* 39.3 (Dec. 1983), pp. 268–274. ISSN: 0304-8853. DOI: 10.1016/0304-8853(83)90085-9.

[FN84] Israel Felner and Israel Nowik. "Itinerant and local magnetism, superconductivity and mixed valency phenomena in RM2Si2, (R = rare earth, M = Rh, Ru)°". In: *Journal of Physics and Chemistry of Solids* 45.4 (Jan. 1984), pp. 419–426. ISSN: 0022-3697. DOI: 10.1016/0022-3697(84)90149-5.

[Szy+84] A. Szytuła et al. "Magnetic ordering in NdRh2Si2 and ErRH2Si2". In: *Solid State Communications* 52.4 (Oct. 1984), pp. 395–398. ISSN: 0038-1098. DOI: 10.1016/0038-1098(84)90021-8.

[Blu85] M. Blume. "Magnetic scattering of x rays (invited)". In: *Journal of Applied Physics* 57.8 (Apr. 1985). Publisher: American Institute of Physics, pp. 3615–3618. ISSN: 0021-8979. DOI: 10.1063/1.335023.

[Szy+86] A. Szytuła et al. "X-ray study of crystal structure and pressure dependence of the Néel temperature of the GdRh2Si2 and TbRh2Si2 compounds". In: *Solid State Communications* 57.10 (Mar. 1986), pp. 813–815. ISSN: 0038-1098. DOI: 10.1016/0038-1098(86)90182-1.

[Lec87] Janusz Leciejewicz. *Magnetic ordering in ternary intermetallic MT2X2 systems / Janusz Leciejewicz ; Andrzej Szytuła.* eng. Prace fizyczne 26 = 831 [d. Gesamtw.] Kraków: Nakładem Uniw. Jagiellońskiego, 1987. ISBN: 978-83-01-08082-2.

[Lie+87] A. I. Liechtenstein et al. "Local spin density functional approach to the theory of exchange interactions in ferromagnetic metals and alloys". In: *Journal of Magnetism and Magnetic Materials* 67.1 (May 1987), pp. 65–74. ISSN: 0304-8853. DOI: 10.1016/0304-8853(87)90721-9.

[Han+88] J. P. Hannon et al. "X-Ray Resonance Exchange Scattering". In: *Physical Review Letters* 61.10 (Sept. 1988). Publisher: American Physical Society, pp. 1245–1248. DOI: 10.1103/PhysRevLett.61.1245.

[Czj+89] G. Czjzek et al. "A study of compounds GdT2Si2 by Mössbauer spectroscopy and by bulk magnetization measurements". In: *Journal of Magnetism and Magnetic Materials* 79.1 (Apr. 1989), pp. 42–56. ISSN: 0304-8853. DOI: 10.1016/0304-8853(89)90290-4.

[Fig+89] H. Figiel et al. "59Co nuclear magnetic resonance study in GdCo2Si2 compound". In: *Hyperfine Interactions* 51.1 (June 1989), pp. 967–971. ISSN: 1572-9540. DOI: 10.1007/BF02407811.

[AZA91] Vladimir I. Anisimov, Jan Zaanen, and Ole K. Andersen. "Band theory and Mott insulators: Hubbard U instead of Stoner I". In: *Physical Review B* 44.3 (July 1991). Publisher: American Physical Society, pp. 943–954. DOI: 10.1103/PhysRevB.44.943.

[JM91] Jens Jensen and Allan R. Mackintosh. *Rare Earth Magnetism: Structures and Excitations*. The International Series of Monographs on Physics. Oxford: Clarendon Press, 1991. ISBN: 978-0-198-52027-6. URL: https://www.fys.ku.dk/~jjensen/REM.htm (visited on 04/17/2022).

[Kim+92] Bongsoo Kim et al. "Temperature-dependent conduction-band exchange splitting in ferromagnetic hcp gadolinium: Theoretical predictions and photoemission experiments". In: *Phys. Rev. Lett.* 68 (12 Mar. 1992), pp. 1931–1934. DOI: 10.1103/PhysRevLett.68.1931. URL: https://link.aps.org/doi/10.1103/PhysRevLett.68.1931.

[Bea+96] E. Beaurepaire et al. "Ultrafast Spin Dynamics in Ferromagnetic Nickel". In: *Physical Review Letters* 76.22 (1996), pp. 4250–4253. DOI: 10.1103/PhysRevLett.76.4250.

[HM96] J. P. Hill and D. F. McMorrow. "Resonant Exchange Scattering: Polarization Dependence and Correlation Function". In: *Acta Crystallographica Section A: Foundations of Crystallography* 52.2 (Mar. 1996). Number: 2 Publisher: International Union of Crystallography, pp. 236–244. ISSN: 0108-7673. DOI: 10.1107/S0108767395012670.

[PBE96] John P. Perdew, Kieron Burke, and Matthias Ernzerhof. "Generalized Gradient Approximation Made Simple". In: *Physical Review Letters* 77.18 (Oct. 1996). Publisher: American Physical Society, pp. 3865–3868. DOI: 10.1103/PhysRevLett.77.3865.

[ZZ96] A. A. Zholents and M. S. Zolotorev. "Femtosecond X-Ray Pulses of Synchrotron Radiation". In: *Phys. Rev. Lett.* 76 (6 Feb. 1996), pp. 912–915. DOI: 10.1103/PhysRevLett.76.912. URL: https://link.aps.org/doi/10.1103/PhysRevLett.76.912.

[Bod+99] M. Bode et al. "Temperature-Dependent Exchange Splitting of a Surface State on a Local-Moment Magnet: Tb(0001)". In: *Phys. Rev. Lett.* 83 (15 Oct. 1999), pp. 3017–3020. DOI: 10.1103/PhysRevLett.83.3017. URL: https://link.aps.org/doi/10.1103/PhysRevLett.83.3017.

[Mai+02] K. Maiti et al. "Finite Temperature Magnetism in Gd: Evidence against a Stoner Behavior". In: *Phys. Rev. Lett.* 88 (16 Apr. 2002), p. 167205. DOI: 10.1103/PhysRevLett.88.167205. URL: https://link.aps.org/doi/10.1103/PhysRevLett.88.167205.

[DHS03] Andrea Damascelli, Zahid Hussain, and Zhi-Xun Shen. "Angle-resolved photoemission studies of the cuprate superconductors". In: *Rev. Mod. Phys.* 75 (2 Apr. 2003), pp. 473–541. DOI: 10.1103/RevModPhys.75.473. URL: https://link.aps.org/doi/10.1103/RevModPhys.75.473.

[Kam03] van Kampen M. "Ultrafast spin dynamics in ferromagnetic metals". ISBN: 9789038617053. Phd Thesis 1 (Research TU/e / Graduation TU/e). Eindhoven: Technische Universiteit Eindhoven, 2003. DOI: 10.6100/IR566741.

[Ato04] Masao Atoji. "Neutron Diffraction Studies of CaC2, YC2, LaC2, CeC2, TbC2, YbC2, LuC2, and UC2". In: *The Journal of Chemical Physics* 35.6 (Aug. 2004). Publisher: American Institute of PhysicsAIP, p. 1950. ISSN: 0021-9606. DOI: 10.1063/1.1732192. URL: https://aip.scitation.org/doi/abs/10.1063/1.1732192 (visited on 05/03/2022).

[Lis+04] M. Lisowski et al. "Ultra-fast dynamics of electron thermalization, cooling and transport effects in Ru(001)". In: *Applied Physics A* 78.2 (Jan. 2004), pp. 165–176. ISSN: 1432-0630. DOI: 10.1007/s00339-003-2301-7.

[Hol+06] K. Holldack et al. "Femtosecond Terahertz Radiation from Femtoslicing at BESSY". In: *Phys. Rev. Lett.* 96 (5 Feb. 2006), p. 054801. DOI: 10.1103/PhysRevLett.96.054801. URL: https://link.aps.org/doi/10.1103/PhysRevLett.96.054801.

[Ott+06] H. Ott et al. "Magnetic x-ray scattering at the ${M}_{5}$ absorption edge of Ho". In: *Physical Review B* 74.9 (Sept. 2006). Publisher: American Physical Society, p. 094412. DOI: 10.1103/PhysRevB.74.094412.

[CFV07] Claude Chappert, Albert Fert, and Frédéric Nguyen Van Dau. "The emergence of spin electronics in data storage". In: *Nature Materials* 6.11 (Nov. 2007). Number: 11 Publisher: Nature Publishing Group, pp. 813–823. ISSN: 1476-4660. DOI: 10.1038/nmat2024. URL: https://www.nature.com/articles/nmat2024 (visited on 08/16/2022).

[CS07] Łukasz Cywiński and L. J. Sham. "Ultrafast demagnetization in the sp-d model: A theoretical study". In: *Physical Review B* 76.4 (July 2007). Publisher: American Physical Society, p. 045205. DOI: 10.1103/PhysRevB.76.045205.

[Döb+07] K. M. Döbrich et al. "Electronic band structure and Fermi surface of ferromagnetic Tb: Experiment and theory". In: *Phys. Rev. B* 76 (3 July 2007), p. 035123. DOI: 10.1103/PhysRevB.76.035123. URL: https://link.aps.org/doi/10.1103/PhysRevB.76.035123.

[Ern07] Arthur Ernst. "Multiple-scattering theory New developments and applications". Available from INIS: http://inis.iaea.org/search/search.aspx?orig_q=RN:40073562 INIS Reference Number: 40073562. PhD thesis. Dec. 2007.

[Hug+07] I. D. Hughes et al. "Lanthanide contraction and magnetism in the heavy rare earth elements". In: *Nature* 446.7136 (Apr. 2007), pp. 650–653. ISSN: 0028-0836. URL: http://dx.doi.org/10.1038/nature05668.

[Hug07] Ian Hughes. "A first-principles approach to modelling magnetism in strongly-correlated electron systems". phd. University of Warwick, Oct. 2007. URL: http://webcat.warwick.ac.uk/record=b2242299~S1 (visited on 08/04/2022).

[FLB08] J. Fernández-Rodriguez, S. W. Lovesey, and J. A. Blanco. "Polarization analysis in resonant x-ray Bragg diffraction by K2CrO4 at the Cr K-edge". In: *Phys. Rev. B* 77 (9 Mar. 2008), p. 094441. DOI: 10.1103/PhysRevB.77.094441. URL: https://link.aps.org/doi/10.1103/PhysRevB.77.094441.

[Sta+08] U. Staub et al. “Polarization analysis in soft X-ray diffraction to study magnetic and orbital ordering”. In: *Journal of Synchrotron Radiation* 15.5 (Sept. 2008). Number: 5 Publisher: International Union of Crystallography, pp. 469–476. ISSN: 0909-0495. DOI: 10.1107/S0909049508019614.

[Wan+08] J. Wang et al. “Femtosecond demagnetization and hot-hole relaxation in ferromagnetic Ga 1-x Mn x As”. In: *Physical Review B* 77.23 (June 2008). Publisher: American Physical Society, p. 235308. DOI: 10.1103/PhysRevB.77.235308.

[Hos+09] Z. Hossain et al. “Magnetic properties of PrRh2Si2: A neutron diffraction study”. In: *Journal of Magnetism and Magnetic Materials* 321.3 (Feb. 2009), pp. 213–215. ISSN: 0304-8853. DOI: 10.1016/j.jmmm.2008.08.107.

[Atx+10] U. Atxitia et al. “Evidence for thermal mechanisms in laser-induced femtosecond spin dynamics”. In: *Physical Review B* 81.17 (2010), p. 174401. DOI: 10.1103/PhysRevB.81.174401.

[Boe+10] C. Boeglin et al. “Distinguishing the ultrafast dynamics of spin and orbital moments in solids”. In: *Nature* 465.7297 (May 2010). Number: 7297 Publisher: Nature Publishing Group, pp. 458–461. ISSN: 1476-4687. DOI: 10.1038/nature09070.

[Fle+10] U. Flechsig et al. “Performance measurements at the SLS SIM beamline”. In: *AIP Conference Proceedings* 1234.1 (June 2010). Publisher: American Institute of Physics, pp. 319–322. ISSN: 0094-243X. DOI: 10.1063/1.3463200.

[Koo+10] B. Koopmans et al. “Explaining the paradoxical diversity of ultrafast laser-induced demagnetization”. In: *Nature Materials* 9.3 (Mar. 2010), pp. 259–265. ISSN: 1476-4660. DOI: 10.1038/nmat2593.

[Shi+10] T. Shigeoka et al. “High Field Metamagnetism of PrRh2Si2 Single Crystal Compound Having Anomalously High Néel Temperature”. In: *Journal of Low Temperature Physics* 159.1 (Apr. 2010), pp. 42–45. ISSN: 1573-7357. DOI: 10.1007/s10909-009-0077-7. URL: https://doi.org/10.1007/s10909-009-0077-7 (visited on 06/15/2022).

[AC11] U. Atxitia and O. Chubykalo-Fesenko. “Ultrafast magnetization dynamics rates within the Landau-Lifshitz-Bloch model”. In: *Physical Review B* 84.14 (2011), p. 144414. DOI: 10.1103/PhysRevB.84.144414.

[Ost+11] Thomas A. Ostler et al. “Crystallographically amorphous ferrimagnetic alloys: Comparing a localized atomistic spin model with experiments”. In: *Physical Review B* 84.2 (July 2011). Publisher: American Physical Society, p. 024407. DOI: 10.1103/PhysRevB.84.024407.

[Rad+11] I. Radu et al. “Transient ferromagnetic-like state mediating ultrafast reversal of antiferromagnetically coupled spins”. In: *Nature* 472.7342 (Apr. 2011), pp. 205–208. ISSN: 1476-4687. DOI: 10.1038/nature09901.

[Wie+11] Marko Wietstruk et al. “Hot-Electron-Driven Enhancement of Spin-Lattice Coupling in Gd and Tb 4f Ferromagnets Observed by Femtosecond X-Ray Magnetic Circular Dichroism”. In: *Physical Review Letters* 106.12 (Mar. 2011). Publisher: American Physical Society, p. 127401. DOI: 10.1103/PhysRevLett.106.127401.

[Hey+12] C. M. Heyl et al. “High-order harmonic generation with μJ laser pulses at high repetition rates”. In: *Journal of Physics B: Atomic, Molecular and Optical Physics* 45.7 (Mar. 2012). Publisher: IOP Publishing, p. 074020. ISSN: 0953-4075. DOI: 10.1088/0953-4075/45/7/074020. URL: https://doi.org/10.1088/0953-4075/45/7/074020 (visited on 08/28/2022).

[Men+12] J. H. Mentink et al. “Ultrafast Spin Dynamics in Multisublattice Magnets”. In: *Physical Review Letters* 108.5 (Jan. 2012). Publisher: American Physical Society, p. 057202. DOI: 10.1103/PhysRevLett.108.057202.

[Ost+12] T. A. Ostler et al. “Ultrafast heating as a sufficient stimulus for magnetization reversal in a ferrimagnet”. In: *Nature Communications* 3.1 (Feb. 2012). Number: 1 Publisher: Nature Publishing Group, p. 666. ISSN: 2041-1723. DOI: 10.1038/ncomms1666.

[Rot+12] T. Roth et al. “Temperature Dependence of Laser-Induced Demagnetization in Ni: A Key for Identifying the Underlying Mechanism”. In: *Physical Review X* 2.2 (May 2012). Publisher: American Physical Society, p. 021006. DOI: 10.1103/PhysRevX.2.021006.

[Sch+12] F. Schlickeiser et al. “Temperature dependence of the frequencies and effective damping parameters of ferrimagnetic resonance”. In: *Phys. Rev. B* 86 (21 Dec. 2012), p. 214416. DOI: 10.1103/PhysRevB.86.214416. URL: https://link.aps.org/doi/10.1103/PhysRevB.86.214416.

[Sul+12] Muhammad Sultan et al. “Electron- and phonon-mediated ultrafast magnetization dynamics of Gd(0001)”. In: *Physical Review B* 85.18 (2012), p. 184407. DOI: 10.1103/PhysRevB.85.184407.

[Brz+13] Maria Brzhezinskaya et al. “A novel monochromator for experiments with ultrashort X-ray pulses”. In: *Journal of Synchrotron Radiation* 20.4 (July 2013), pp. 522–530. DOI: 10.1107/S0909049513008613. URL: https://doi.org/10.1107/S0909049513008613.

[Esc+13] A. Eschenlohr et al. “Ultrafast spin transport as key to femtosecond demagnetization”. In: *Nature Materials* 12.4 (Apr. 2013). Number: 4 Publisher: Nature Publishing Group, pp. 332–336. ISSN: 1476-4660. DOI: 10.1038/nmat3546.

[Fin+13] J. Fink et al. “Resonant elastic soft x-ray scattering”. In: *Reports on Progress in Physics* 76.5 (Apr. 2013), p. 056502. ISSN: 0034-4885. DOI: 10.1088/0034-4885/76/5/056502.

[Wal+13] H. C. Walker et al. “Circularly polarized x-ray scattering investigation of spin-lattice coupling in TbMnO3 in crossed electric and magnetic fields”. In: *Phys. Rev. B* 88 (21 Dec. 2013), p. 214415. DOI: 10.1103/PhysRevB.88.214415. URL: https://link.aps.org/doi/10.1103/PhysRevB.88.214415.

[Atx+14] U. Atxitia et al. “Controlling the polarity of the transient ferromagneticlike state in ferrimagnets”. In: *Physical Review B* 89.22 (2014), p. 224421. DOI: 10.1103/PhysRevB.89.224421.

[Ber+14] N. Bergeard et al. “Ultrafast angular momentum transfer in multisublattice ferrimagnets”. In: *Nature Communications* 5.1 (Mar. 2014). Number: 1 Publisher: Nature Publishing Group, p. 3466. ISSN: 2041-1723. DOI: 10.1038/ncomms4466.

[Esc+14] A. Eschenlohr et al. “Role of spin-lattice coupling in the ultrafast demagnetization of Gd 1-x Tb x alloys”. In: *Physical Review B* 89.21 (June 2014). Publisher: American Physical Society, p. 214423. DOI: 10.1103/PhysRevB.89.214423.

[Hol+14] K. Holldack et al. “FemtoSpeX: a versatile optical pump–soft X-ray probe facility with 100 fs X-ray pulses of variable polarization”. In: *Journal of Synchrotron Radiation* 21.5 (Sept. 2014), pp. 1090–1104. ISSN: 1600-5775. DOI: 10.1107/S1600577514012247.

[Men+14] J. Mendil et al. “Resolving the role of femtosecond heated electrons in ultrafast spin dynamics”. In: *Scientific Reports* 4.1 (Feb. 2014), p. 3980. ISSN: 2045-2322. DOI: 10.1038/srep03980.

[Nie+14] P. Nieves et al. “Quantum Landau-Lifshitz-Bloch equation and its comparison with the classical case”. In: *Physical Review B* 90.10 (2014), p. 104428. DOI: 10.1103/PhysRevB.90.104428.

[Rot+14] Jan Rothhardt et al. “Absorption-limited and phase-matched high harmonic generation in the tight focusing regime”. In: *New Journal of Physics* 16.3 (Mar. 2014). Publisher: IOP Publishing, p. 033022. ISSN: 1367-2630. DOI: 10.1088/1367-2630/16/3/033022. URL: https://doi.org/10.1088/1367-2630/16/3/033022 (visited on 08/28/2022).

[And+15] Beatrice Andres et al. “Separating Exchange Splitting from Spin Mixing in Gadolinium by Femtosecond Laser Excitation”. In: *Physical Review Letters* 115.20 (2015), p. 207404. DOI: 10.1103/PhysRevLett.115.207404.

[Fri+15] B. Frietsch et al. “Disparate ultrafast dynamics of itinerant and localized magnetic moments in gadolinium metal”. In: *Nature Communications* 6.1 (Sept. 2015), p. 8262. ISSN: 2041-1723. DOI: 10.1038/ncomms9262.

[Gei+15] Matthias Geilhufe et al. “Numerical solution of the relativistic single-site scattering problem for the Coulomb and the Mathieu potential”. In: *Journal of Physics: Condensed Matter* 27.43 (Oct. 2015). Publisher: IOP Publishing, p. 435202. ISSN: 0953-8984. DOI: 10.1088/0953-8984/27/43/435202.

[KEF15] T. Kachel, F. Eggenstein, and R. Follath. “A soft X-ray plane-grating monochromator optimized for elliptical dipole radiation from modern sources”. In: *Journal of Synchrotron Radiation* 22.5 (Sept. 2015). Number: 5 Publisher: International Union of Crystallography, pp. 1301–1305. ISSN: 1600-5775. DOI: 10.1107/S1600577515010826.

[KK15] K. Kliemt and C. Krellner. “Single crystal growth and characterization of GdRh2Si2”. In: *Journal of Crystal Growth* 419 (2015), pp. 37–41. ISSN: 0022-0248. DOI: 10.1016/j.jcrysgro.2015.02.079.

[Kri+15] K. Krieger et al. “Laser-Induced Demagnetization at Ultrashort Time Scales: Predictions of TDDFT”. In: *Journal of Chemical Theory and Computation* 11.10 (Oct. 2015), pp. 4870–4874. ISSN: 1549-9618. DOI: 10.1021/acs.jctc.5b00621.

[Pup+15] Michele Puppin et al. “500 kHz OPCPA delivering tunable sub-20 fs pulses with 15 W average power based on an all-ytterbium laser”. In: *Optics Express* 23.2 (Jan. 2015), pp. 1491–1497. ISSN: 1094-4087. DOI: 10.1364/OE.23.001491.

[AHN16] U. Atxitia, D. Hinzke, and U. Nowak. “Fundamentals and applications of the Landau–Lifshitz–Bloch equation”. In: *Journal of Physics D: Applied Physics* 50.3 (Dec. 2016), p. 033003. ISSN: 0022-3727. DOI: 10.1088/1361-6463/50/3/033003.

[Güt+16] M. Güttler et al. “Robust and tunable itinerant ferromagnetism at the silicon surface of the antiferromagnet GdRh2Si2”. In: *Scientific Reports* 6.1 (Apr. 2016), p. 24254. ISSN: 2045-2322. DOI: 10.1038/srep24254.

[Jun+16] T. Jungwirth et al. “Antiferromagnetic spintronics”. In: *Nature Nanotechnology* 11.3 (Mar. 2016), pp. 231–241. ISSN: 1748-3395. DOI: 10.1038/nnano.2016.18.

[Olo+16] L.-P. Oloff et al. “Pump laser-induced space-charge effects in HHG-driven time- and angle-resolved photoelectron spectroscopy”. In: *Journal of Applied Physics* 119.22 (June 2016), p. 225106. ISSN: 0021-8979. DOI: 10.1063/1.4953643.

[Ret+16] L. Rettig et al. “Itinerant and Localized Magnetization Dynamics in Antiferromagnetic Ho”. In: *Physical Review Letters* 116.25 (2016), p. 257202. DOI: 10.1103/PhysRevLett.116.257202.

[Sch+16] Daniel Schick et al. “Analysis of the halo background in femtosecond slicing experiments”. In: *Journal of Synchrotron Radiation* 23.3 (May 2016), pp. 700–711. DOI: 10.1107/S160057751600401X. URL: https://doi.org/10.1107/S160057751600401X.

[Wad+16] P. Wadley et al. “Electrical switching of an antiferromagnet”. In: *Science* 351.6273 (2016), pp. 587–590. DOI: 10.1126/science.aab1031. eprint: https://www.science.org/doi/pdf/10.1126/science.aab1031. URL: https://www.science.org/doi/abs/10.1126/science.aab1031.

[Eri+17] Olle Eriksson et al. *Atomistic Spin Dynamics: Foundations and Applications*. Oxford: Oxford University Press, 2017. ISBN: 978-0-19-878866-9. DOI: 10.1093/oso/9780198788669.001.0001.

[Fer+17] T. Ferté et al. “Element-resolved ultrafast demagnetization rates in ferrimagnetic CoDy”. In: *Physical Review B* 96.13 (Oct. 2017). Publisher: American Physical Society, p. 134303. DOI: 10.1103/PhysRevB.96.134303.

[Gen+17] Alexander Generalov et al. “Spin Orientation of Two-Dimensional Electrons Driven by Temperature-Tunable Competition of Spin–Orbit and Exchange–Magnetic Interactions”. In: *Nano Letters* 17.2 (Feb. 2017), pp. 811–820. ISSN: 1530-6984. DOI: 10.1021/acs.nanolett.6b04036.

[Kli+17] K. Kliemt et al. “GdRh2Si2: An exemplary tetragonal system for antiferromagnetic order with weak in-plane anisotropy”. In: *Physical Review B* 95.13 (2017), p. 134403. DOI: 10.1103/PhysRevB.95.134403.

[Thi+17] Nele Thielemann-Kühn et al. “Ultrafast and Energy-Efficient Quenching of Spin Order: Antiferromagnetism Beats Ferromagnetism”. In: *Physical Review Letters* 119.19 (2017), p. 197202. DOI: 10.1103/PhysRevLett.119.197202.

[KBK18] K. Kliemt, M. Bolte, and C. Krellner. “Crystal growth and magnetic characterization of HoIr2Si2 (I4/mmm)”. In: *Journal of Physics: Condensed Matter* 30.38 (Aug. 2018). Publisher: IOP Publishing, p. 385801. ISSN: 0953-8984. DOI: 10.1088/1361-648X/aada97.

[Ole+18] Kamil Olejník et al. “Terahertz electrical writing speed in an antiferromagnetic memory”. In: *Science Advances* 4.3 (Mar. 2018). Publisher: American Association for the Advancement of Science, eaar3566. DOI: 10.1126/sciadv.aar3566. URL: https://www.science.org/doi/10.1126/sciadv.aar3566 (visited on 08/15/2022).

[Sic+18] J. Sichelschmidt et al. “Weak magnetic anisotropy in GdRh2Si2 studied by magnetic resonance”. In: *Physical Review B* 97.21 (2018), p. 214424. DOI: 10.1103/PhysRevB.97.214424.

[Ten+18] Phoebe Tengdin et al. “Critical behavior within 20 fs drives the out-of-equilibrium laser-induced magnetic phase transition in nickel”. In: *Science Advances* 4.3 (2018), eaap9744. DOI: 10.1126/sciadv.aap9744.

[Che+19] Zhifeng Chen et al. “Ultrafast dynamics of 4f electron spins in TbFeCo film driven by inter-atomic 3d–5d–4f exchange coupling”. In: *New Journal of Physics* 21.12 (Dec. 2019), p. 123007. ISSN: 1367-2630. DOI: 10.1088/1367-2630/ab5aa4.

[Dor+19] C. Dornes et al. “The ultrafast Einstein–de Haas effect”. In: *Nature* 565.7738 (Jan. 2019). Number: 7738 Publisher: Nature Publishing Group, pp. 209–212. ISSN: 1476-4687. DOI: 10.1038/s41586-018-0822-7.

[Güt+19] M. Güttler et al. “Divalent EuRh2Si2 as a reference for the Luttinger theorem and antiferromagnetism in trivalent heavy-fermion YbRh2Si2”. In: *Nature Communications* 10.1 (Feb. 2019), p. 796. ISSN: 2041-1723. DOI: 10.1038/s41467-019-08688-y.

[Hen+19] Martin Hennecke et al. “Angular Momentum Flow During Ultrafast Demagnetization of a Ferrimagnet”. In: *Physical Review Letters* 122.15 (Apr. 2019). Publisher: American Physical Society, p. 157202. DOI: 10.1103/PhysRevLett.122.157202.

[VR19] Sergio O. Valenzuela and Stephan Roche. “The phase diagram of 2D antiferromagnets”. In: *Nature Nanotechnology* 14.12 (Dec. 2019). Number: 12 Publisher: Nature Publishing Group, pp. 1088–1089. ISSN: 1748-3395. DOI: 10.1038/s41565-019-0592-x. URL: https://www.nature.com/articles/s41565-019-0592-x (visited on 08/24/2022).

[Fri+20] B. Frietsch et al. “The role of ultrafast magnon generation in the magnetization dynamics of rare-earth metals”. In: *Science Advances* 6.39 (2020), eabb1601. DOI: 10.1126/sciadv.abb1601.

[Hof+20] Martin Hoffmann et al. “Magnetic and Electronic Properties of Complex Oxides from First-Principles”. In: *physica status solidi (b)* 257.7 (2020), p. 1900671. ISSN: 1521-3951. DOI: 10.1002/pssb.201900671.

[Kli+20] Kristin Kliemt et al. “Crystal Growth of Materials with the ThCr2Si2 Structure Type”. In: *Crystal Research and Technology* 55.2 (2020), p. 1900116. ISSN: 1521-4079. DOI: 10.1002/crat.201900116.

[Mak+20] J. Maklar et al. “A quantitative comparison of time-of-flight momentum microscopes and hemispherical analyzers for time- and angle-resolved photoemission spectroscopy experiments”. In: *Review of Scientific Instruments* 91.12 (2020), p. 123112. DOI: 10.1063/5.0024493. eprint: https://doi.org/10.1063/5.0024493. URL: https://doi.org/10.1063/5.0024493.

[Shi+20] Je-Ho Shim et al. “Role of non-thermal electrons in ultrafast spin dynamics of ferromagnetic multilayer”. In: *Scientific Reports* 10.1 (Apr. 2020), p. 6355. ISSN: 2045-2322. DOI: 10.1038/s41598-020-63452-3.

[Win+20] Y. W. Windsor et al. “Deterministic control of an antiferromagnetic spin arrangement using ultrafast optical excitation”. In: *Communications Physics* 3.1 (Aug. 2020), pp. 1–8. ISSN: 2399-3650. DOI: 10.1038/s42005-020-00407-0.

[ALW21] Beatrice Andres, Sang Eun Lee, and Martin Weinelt. “The role of spin-lattice coupling for ultrafast changes of the magnetic order in rare earth metals”. In: *Applied Physics Letters* 119.18 (Nov. 2021), p. 182404. ISSN: 0003-6951. DOI: 10.1063/5.0067397.

[Gim+21] Radel R. Gimaev et al. “Magnetic and Electronic Properties of Heavy Lanthanides (Gd, Tb, Dy, Er, Ho, Tm)”. In: *Crystals* 11.2 (2021). ISSN: 2073-4352. DOI: 10.3390/cryst11020082. URL: https://www.mdpi.com/2073-4352/11/2/82.

[Gol+21] E. Golias et al. “Ultrafast Optically Induced Ferromagnetic State in an Elemental Antiferromagnet”. In: *Physical Review Letters* 126.10 (2021), p. 107202. DOI: 10.1103/PhysRevLett.126.107202.

[Rah+21] Sharidya Rahman et al. “Recent Developments in van der Waals Antiferromagnetic 2D Materials: Synthesis, Characterization, and Device Implementation”. In: *ACS Nano* 15.11 (Nov. 2021). Publisher: American Chemical Society, pp. 17175–17213. ISSN: 1936-0851. DOI: 10.1021/acsnano.1c06864. URL: https://doi.org/10.1021/acsnano.1c06864 (visited on 08/24/2022).

[SHS21] Jonathan A. Sobota, Yu He, and Zhi-Xun Shen. “Angle-resolved photoemission studies of quantum materials”. In: *Rev. Mod. Phys.* 93 (2 May 2021), p. 025006. DOI: 10.1103/RevModPhys.93.025006. URL: https://link.aps.org/doi/10.1103/RevModPhys.93.025006.

[Wan+21] Shiyao Wang et al. “Discovery of intrinsic two-dimensional antiferromagnets from transition-metal borides”. In: *Nanoscale* 13.17 (May 2021). Publisher: The Royal Society of Chemistry, pp. 8254–8263. ISSN: 2040-3372. DOI: 10.1039/D1NR01103K. URL: https://pubs.rsc.org/en/content/articlelanding/2021/nr/d1nr01103k (visited on 08/24/2022).

[Zah+21] Daniela Zahn et al. “Lattice dynamics and ultrafast energy flow between electrons, spins, and phonons in a 3d ferromagnet”. In: *Physical Review Research* 3.2 (2021), p. 023032. DOI: 10.1103/PhysRevResearch.3.023032.

[JA22a] Florian Jakobs and Unai Atxitia. *Exchange-enhancement of the ultrafast magnetic order dynamics in antiferromagnets*. Number: arXiv:2206.05783 arXiv:2206.05783 [cond-mat]. June 2022. DOI: 10.48550/arXiv.2206.05783. URL: http://arxiv.org/abs/2206.05783 (visited on 06/14/2022).

[JA22b] Florian Jakobs and Unai Atxitia. *Universal criteria for single femtosecond pulse ultrafast magnetization switching in ferrimagnets*. Number: arXiv:2201.09067 arXiv:2201.09067 [cond-mat] version: 1. Jan. 2022. DOI: 10.48550/arXiv.2201.09067. URL: http://arxiv.org/abs/2201.09067 (visited on 06/14/2022).

[Kim+22] Kook Tae Kim et al. "Origin of circular dichroism in resonant elastic x-ray scattering from magnetic and polar chiral structures". In: *Phys. Rev. B* 106 (3 July 2022), p. 035116. DOI: 10.1103/PhysRevB.106.035116. URL: https://link.aps.org/doi/10.1103/PhysRevB.106.035116.

[LJ22] Yongnan Li and Pengfei Ji. "Ab initio calculation of electron temperature dependent electron heat capacity and electron-phonon coupling factor of noble metals". In: *Computational Materials Science* 202 (2022), p. 110959. ISSN: 0927-0256. DOI: 10.1016/j.commatsci.2021.110959.

[Moe+22] Behnam Moeini et al. "Definition of a new (Doniach-Sunjic-Shirley) peak shape for fitting asymmetric signals applied to reduced graphene oxide/graphene oxide XPS spectra". In: *Surface and Interface Analysis* 54.1 (2022), pp. 67–77. DOI: https://doi.org/10.1002/sia.7021. eprint: https://analyticalsciencejournals.onlinelibrary.wiley.com/doi/pdf/10.1002/sia.7021. URL: https://analyticalsciencejournals.onlinelibrary.wiley.com/doi/abs/10.1002/sia.7021.

[Win+22] Y. W. Windsor et al. "Exchange scaling of ultrafast angular momentum transfer in 4f antiferromagnets". In: *Nature Materials* (Feb. 2022), pp. 1–4. ISSN: 1476-4660. DOI: 10.1038/s41563-022-01206-4.

[Zah+22] Daniela Zahn et al. "Intrinsic energy flow in laser-excited 3d ferromagnets". In: *Physical Review Research* 4.1 (2022), p. 013104. DOI: 10.1103/PhysRevResearch.4.013104.

[Cha+] John. T Chalker et al. *Introduction to Frustrated Magnetism*. Ed. by Claudine Lacroix, Philippe Mendels, and Frédéric Mila. 1st ed. Vol. 164. Springer Series in Solid-State Sciences. Springer Berlin Heidelberg. ISBN: 978-3-642-10589-0. URL: https://link.springer.com/book/10.1007/978-3-642-10589-0 (visited on 08/25/2022).